United Aircraft Research Laboratories

UNITED AIRCRAFT CORPORATION

EAST HARTFORD, CONNECTICUT

D-910093-19

Analytical Study
of Hydrogen Turbopump Cycles
for Advanced Nuclear Rockets

NASA Contract No. NASw-847

REPORTED BY G. H. McLafferty

G. H. McLafferty

H. H. Michels

H. H. Michels

T. S. Latham

T. S. Latham

R. Roback

R. Roback

DATE September 1965

NO. OF PAGES 88

COPY NO. 80

FOREWORD

An exploratory experimental and theoretical investigation of gaseous nuclear rocket technology is being conducted by the United Aircraft Corporation Research Laboratories under Contract NASw-847 with the joint AEC-NASA Space Nuclear Propulsion Office. The Technical Supervisor of the Contract for NASA is Captain W. A. Yingling (USAF). Results of the investigation conducted during the period between September 15, 1964 and September 15, 1965 are described in the following eleven reports (including the present report) which comprise the required third Interim Summary Technical Report under the Contract:

1. McFarlin, D. J.: Experimental Investigation of the Effect of Peripheral Wall Injection Technique on Turbulence in an Air Vortex Tube. UAC Research Laboratories Report D-910091-5, September 1965. (Unclassified)

2. Johnson, B. V.: Analytical Study of Propellant Flow Requirements for Reducing Heat Transfer to the End Walls of Vortex-Stabilized Gaseous Nuclear Rocket Engines (U). UAC Research Laboratories Report D-910091-6, September 1965. (report classified Confidential)

3. Travers, A.: Experimental Investigation of Peripheral Wall Injection Techniques in a Water Vortex Tube. UAC Research Laboratories Report D-910091-7, September 1965. (Unclassified)

4. Johnson, B. V., and A. Travers: Analytical and Experimental Investigation of Flow Control in a Vortex Tube by End-Wall Suction and Injection (U). UAC Research Laboratories Report D-910091-8, September 1965. (report classified Confidential)

5. Mensing, A. E., and J. S. Kendall: Experimental Investigation of the Effect of Heavy-to-Light-Gas Density Ratio on Two-Component Vortex Tube Containment Characteristics (U). UAC Research Laboratories Report D-910091-9, September 1965. (report classified Confidential)

6. Krascella, N. L.: Theoretical Investigation of the Opacity of Heavy-Atom Gases. UAC Research Laboratories Report D-910092-4, September 1965. (Unclassified)

7. Kesten, A. S., and R. B. Kinney: Theoretical Effect of Changes in Constituent Opacities on Radiant Heat Transfer in a Vortex-Stabilized Gaseous Nuclear Rocket (U). UAC Research Laboratories Report D-910092-5, September 1965. (report classified Confidential)

8. Marteney, P. J., N. L. Krascella, and W. G. Burwell: Experimental Refractive Indices and Theoretical Small-Particle Spectral Properties of Selected Metals. UAC Research Laboratories Report D-910092-6, September 1965. (Unclassified)

9. Williamson, H. A., H. H. Michels, and S. B. Schneiderman: Theoretical Investigation of the Lowest Five Ionization Potentials of Uranium. UAC Research Laboratories Report D-910099-2, September 1965. (Unclassified)

10. McLafferty, G. H., H. H. Michels, T. S. Latham, and R. Roback: Analytical Study of Hydrogen Turbopump Cycles for Advanced Nuclear Rockets. UAC Research Laboratories Report D-910093-19, September 1965. (Unclassified)(present report)

11. McLafferty, G. H.: Analytical Study of the Performance Characteristics of Vortex-Stabilized Gaseous Nuclear Rocket Engines (U). UAC Research Laboratories Report D-910093-20, September 1965. (report classified Confidential)

Report D-910093-19

Analytical Study of Hydrogen Turbopump Cycles for Advanced Nuclear Rockets

TABLE OF CONTENTS

Report D-910093-19

Analytical Study of Hydrogen Turbopump Cycles for Advanced Nuclear Rockets

N66 14286

SUMMARY

An analytical study was conducted to determine the characteristics of three different turbopump cycles which might be employed to obtain the high engine inlet pressures which are expected to exist in advanced nuclear rockets. The three cycles considered were: a topping cycle, in which the power required to drive the pump is obtained by passing all of the pump-exit flow through a turbine before this flow enters the engine; a bleed cycle, in which all of the pump power is obtained by discharging a fraction of the pump-exit flow through a bleed turbine with an expansion pressure ratio of 0.01; and a mixed cycle, in which half of the power to drive the pump is obtained from a primary turbine and half from a bleed turbine. The studies were conducted for a range of turbine inlet temperatures between 1400 and 3800 R, for a range of turbine inlet pressures between 200 and 5000 atm, for pressure drops between the pump exit and the turbine inlet of zero and 50 atm, and for three different combinations of pump and turbine efficiency. The results of the study indicate the effect of engine inlet pressure on the turbine pressure drop and/or the bleed flow fraction for each cycle.

Three studies not connected with hydrogen turbopumps are described in the Appendixes. These are: an analysis of the approximate temperature distribution in the fuel-containment region of a coaxial-flow gaseous nuclear rocket (APPENDIX I); a change in form of heavy-gas containment data obtained from NASA Lewis coaxial-flow tests (APPENDIX II); and an analysis of the heat generation rate in fuel passing through a fuel injection duct located in the moderator of a gaseous nuclear rocket engine (APPENDIX III).

Author

RESULTS

Results of Turbopump Analysis

Unless otherwise noted, each of the following results was obtained for a turbine inlet temperature of 2200 R, a pump efficiency of 70 percent, a turbine efficiency of 80 percent, and a pressure drop between the pump exit and turbine inlet of 50 atm. It should be noted that a final choice between the different cycles considered will require detailed structural analyses as well as cycle studies.

1. Attainment of an engine inlet pressure of 1000 atm will require: for a topping cycle, a primary turbine pressure drop of 1000 atm; for a bleed cycle, a bleed fraction of 15.5 percent; and for a mixed cycle, a primary turbine pressure drop of 260 atm and a bleed fraction of 10.0 percent.

2. A reduction in the engine inlet pressure from 1000 to 500 atm will result in the following: for the topping cycle, a reduction in the primary turbine pressure drop from 1000 to 170 atm; for the bleed cycle, a reduction of bleed fraction from 15.5 percent to 8.8 percent; and for the mixed cycle, a reduction in the primary turbine pressure drop from 260 to 66 atm and a reduction in bleed fraction from 10.0 percent to 5.1 percent.

3. An increase in the engine inlet pressure from 1000 to 2000 atm will result in the following: for the bleed cycle, an increase in bleed flow from 15.5 percent to 26.5 percent; and for the mixed cycle, an increase in primary turbine pressure drop from 260 to 1100 atm and an increase in the bleed fraction from 10.0 percent to 21.4 percent. The topping cycle will not provide an engine inlet pressure of 2000 atm for any pressure drop across the turbine for a turbine inlet temperature of 2200 R.

4. An increase in turbine inlet temperature from 2200 to 3800 R will result in the following for an engine inlet pressure of 1000 atm: for the topping cycle, a decrease in primary turbine pressure drop from 1000 to 360 atm; for the bleed cycle, a decrease in bleed flow from 15.5 percent to 9.0 percent; and for the mixed cycle, a decrease in primary turbine pressure drop from 260 to 138 atm and a decrease in bleed flow from 10.0 percent to 5.3 percent.

5. An increase of pump efficiency from 70 percent to 80 percent combined with an increase in turbine efficiency from 80 to 90 percent will result in the following for an engine inlet pressure of 1000 atm: for the topping cycle, a decrease in the primary turbine pressure drop from 1000 to 530 atm; for the bleed cycle, a decrease in bleed flow from 15.5 percent to 12.1 percent; and for the mixed cycle, a decrease in primary turbine pressure drop from 260 to 188 atm and a decrease in bleed flow from 10.0 percent to 7.2 percent.

6. A decrease in the pressure drop between the pump exit and the turbine inlet from 50 to zero will result in the following for an engine inlet pressure of 1000 atm: for the topping cycle, a decrease in the primary turbine pressure drop from 1000 to 940 atm; for the bleed cycle, a decrease in bleed flow from 15.5 percent to 14.9 percent; and for the mixed cycle, a decrease in primary turbine pressure drop from 260 to 240 atm and a decrease in bleed flow from 10.0 percent to 9.5 percent.

Results of Analyses described in Appendixes

7. The temperatures near the centerline of a coaxial-flow gaseous nuclear rocket will be on the order of 100,000 to 200,000 R for cavity pressures of 100 to 1000 atm and for a heat flux at the outside edge of the fuel-containment region equal to that for black body thermal radiation at a temperature of 30,000 R.

8. For gaseous nuclear rockets in which the fuel and propellant are injected separately into the cavity, a high fuel velocity is required when the fuel passes through the moderator in order to prevent excessive self-heating of the fuel. For the example discussed in an Appendix, a fuel velocity of 67,000 ft/sec would be required to keep the temperature of the fuel below 3600 R at the exit of the fuel-injection duct with no neutron-absorbing material surrounding the fuel-injection duct.

9. The required velocity of the fuel in the fuel-injection duct passing through the moderator can be reduced by surrounding this duct with a sleeve made from a neutron-absorbing material such as hafnium. For the example described in an Appendix, a sleeve having a thickness of 0.5 in. surrounding a duct having a radius of 0.04 in. would result in decreasing the required fuel velocity from 67,000 ft/sec to 200 ft/sec.

10. Surrounding a fuel-injection duct with a neutron-absorbing material may result in a significant increase in the critical fuel mass required in the cavity unless care is taken with the design of the fuel-injection duct. For the example discussed in Result No. 9, this increase in fuel mass was approximately 5 percent.

INTRODUCTION

The Research Laboratories of United Aircraft Corporation under Contract NASw-847 with the joint AEC-NASA Space Nuclear Propulsion Office are investigating various technologies which influence the characteristics of gaseous nuclear rockets. Studies conducted under this contract and at the NASA Lewis Research Center indicate that it will be desirable to operate such rockets at high pressures in order to reduce the engine size necessary to obtain attractive performance capabilities. One of the engine components which may limit the maximum operating pressure is the turbopump. Available studies of turbopumps for nuclear rockets (see, for example, Refs. 1 and 2) are usually limited to consideration of engine pressures of 100 atm of less, whereas pressures of 100 to 2000 atm may be desirable for gaseous nuclear rockets. The object of the study described in the main body of this report is to determine the characteristics of the turbopump cycle for engine pressures of interest for gaseous nuclear rockets.

The investigation of gaseous nuclear rocket technology under Contract NASw-847 has also been concerned with studies of a number of other problem areas, and results from three of these studies are described in the Appendixes. These studies include analyses of the temperature distribution and fuel-containment characteristics of coaxial-flow nuclear rockets and studies of the heat generation rate in fuel passing through a fuel-injection duct located in the moderator of a gaseous nuclear rocket engine.

HYDROGEN PROPERTIES

Cycle studies for hydrogen turbopumps for advanced nuclear rocket engines require information on the properties of hydrogen under the conditions which will exist in both the pump and turbine. The methods employed to obtain these properties are described in the following subsections.

Hydrogen Properties used in Turbine Analysis

Thermodynamic properties of normal hydrogen (3:1 ortho-para mixture) were calculated for temperatures between 600 and 6000 R and pressures between 1.0 and 5,000 atm. The computation procedure employed was essentially that described in Ref. 3 with modifications to allow a better fit of compressibility data at the higher temperatures. A general description of this procedure, which will be referred to hereafter as the Woolley procedure, appears in the first following subsection, and a discussion of the modifications which were made to this procedure appears in the second following subsection.

Woolley Procedure

Thermodynamic properties of hydrogen are first obtained for the idealized gas state from the partition functions for the translational, rotational, vibrational, and electronic contributions. The partition function for vibration was taken as the quantum-mechanical sum-over-state function,

$$\sum_j g_j \, e^{-\epsilon_j / kT} \tag{1}$$

where the values of ϵ_j used in the summation were derived from an analysis of the molecular spectra of hydrogen. The translational contributions were calculated in the usual manner for an ideal gas. The rotational contributions were evaluated in a high-temperature approximation using the series

$$Q_r = \frac{1}{2\sigma}\left(1 + \frac{\sigma}{3} + \frac{\sigma^2}{15} + \cdots\right) \tag{2}$$

with

$$\sigma = \hbar^2 / 2 I_e k T \tag{3}$$

In order to calculate the thermodynamic properties of gaseous hydrogen at high densities, it is necessary to correct the ideal gas properties to take into account changes due to deviations from the law of ideal gases as the density is increased. A very careful and critical analysis of available compressibility data (see, for example, Refs. 4 and 5) has been performed for temperatures between 273 K and 600 K in Ref. 3 and the final form chosen to represent the compressibility of hydrogen can be written as

$$Z = \frac{PV}{RT} = e^{B(T)\rho + C(T)\rho^2} \tag{4}$$

where ρ is the density, $B(T)$ is the second virial coefficient for hydrogen, and $C(T)$ is essentially a temperature-dependent empirical parameter and is not identical with the third virial coefficient. The functional forms for $B(T)$ and $C(T)$ were taken in Ref. 3 as

$$B(T) = b_1/T^{1/4} + b_2/T^{3/4} + b_3/T^{5/4} \tag{5}$$

$$C(T) = c_1/T^{3/2} + c_2/T^2 \tag{6}$$

where the coefficients b_i and c_i were adjusted to fit the experimental data.

Corrections for real gas properties are calculated in the Woolley procedure from the following thermodynamic relations.

$$\frac{S - S^0_{IDEAL}}{R} = -\int_0^\rho (Z-1)\frac{d\rho}{\rho} - \int_0^\rho T\left(\frac{\partial Z}{\partial T}\right)_\rho \frac{d\rho}{\rho} \tag{7}$$

$$\frac{H - H^0_{IDEAL}}{RT} = \int_0^\rho T\left(\frac{\partial Z}{\partial T}\right)_\rho \frac{d\rho}{\rho} + Z - 1 \tag{8}$$

$$\frac{C_P - C^{O}_{P_{IDEAL}}}{R} = 2\int_0^{\rho} T\left(\frac{\partial Z}{\partial \rho}\right)_T \frac{d\rho}{\rho} - \int_0^{\rho} T^2\left(\frac{\partial^2 Z}{\partial \rho^2}\right)_T \frac{d\rho}{\rho} + \left[Z + T\left(\frac{\partial Z}{\partial T}\right)_\rho\right]^2 \Big/ \left[Z + \rho\left(\frac{\partial Z}{\partial \rho}\right)_T\right] \tag{9}$$

These corrections become most important in the region of high compressibility, i.e., low temperature and/or high pressure.

Modifications to Woolley Procedure

Since no significant quantity of experimental compressibility data for hydrogen gas exist for temperatures much above 600 K, a theoretical approach was employed to estimate compressibility. The exponential in Eq. (4) can be expanded to give

$$Z = 1 + B(T)\rho + \left[C(T) + B^2(T)\right]\rho^2 + O(\rho^3) + \cdots \tag{10}$$

where $B(T)$ is the second virial coefficient and $\left[C(T) + B^2(T)\right]$ can now be identified as the third virial coefficient. Higher order terms in density are of lesser importance at high temperatures and were not examined explicitly. The second virial coefficient was obtained from the statistical mechanical expression

$$\tilde{B}(T) = -2\pi N\int_0^{\infty}(e^{-\epsilon(r)/kT} - 1)\, r^2 dr \tag{11}$$

where the Lennard-Jones (6-12) potential was used for $\epsilon(r)$.

Similarly, the third virial coefficient was obtained from the theoretical expression

$$\tilde{C}(T) = -8\pi^2 N^2 \iiint \left[e^{-\epsilon(r)/kT} - 1\right]^3 r^3 dr \tag{12}$$

Convenient numerical solutions for $\tilde{B}(T)$ and $\tilde{C}(T)$ are available in Ref. 6, and the coefficients b_i and c_i of Eqs. (5) and (6) were adjusted to agree with these exact numerical solutions. The fundamental constants required for the Lennard-Jones potential were taken from Ref. 6 as $\epsilon/k = 29$ and $r(\epsilon = 0)/r_e = 2.9$. Values of b_i and c_i used in Ref. 3 and calculated using Eqs. (11) and (12) are compared in Table I. The use of this new set of coefficients resulted in only small changes from the original Woolley program in the calculated thermodynamic properties. For example, the calculated enthalpy function was increased by 1 to 2 percent for temperatures about 2000 K at pressures above 2000 atm. A Mollier diagram for hydrogen calculated from the modified Woolley program is given in Fig. 1.

Hydrogen Properties Used in Pump Analysis

All pump calculations were based on hydrogen pump inlet conditions of one atm pressure and 36 R temperature. The calculations of pump work require information on the characteristics of hydrogen for an isentropic compression process beginning at these pump inlet conditions. However, the maximum pressure for such an isentropic process for which data are available (see Ref. 7) is 300 atm, while it is desirable to analyze pumps with exit pressures up to 5000 atm. Therefore, some method of extrapolation of available data had to be adopted in order to perform the calculations. It was decided to extrapolate data on the density of hydrogen and to use this data in the following equation to calculate enthalpy for an isentropic compression process.

$$dH = V\,dP \qquad (13)$$

The variation of hydrogen density for an isentropic compression process beginning at a pressure of one atm and a temperature of 36 R is shown by the solid line in Fig. 2. These data were obtained from Ref. 7. Three different variations of density with pressure are shown in Fig. 2; two of these represent different extrapolations of the data from Ref. 7, and the third represents constant density at all pressures. Also shown on this figure is the density calculated from the modified Woolley program at a pressure of 5000 atm and a temperature of 600 R. Although no data are available to support the validity of this calculated density, the use of the Woolley program probably provides the best estimate of the density under such conditions. It would be expected that the true density at low temperatures would be greater than that at 600 R; therefore Curve B in Fig. 2 might be more realistic than Curve A. However, unless otherwise specified all calculations described in the report were made using Curve A leading to more conservative results. As noted in a following section, some calculations were made to determine the change which would result from using Curves B or C rather than Curve A.

The variation of hydrogen enthalpy with pressure calculated using Eq. (13) is shown in Fig. 3. It can be seen that Curves A and B differ from each other by only a small amount, and then only at high pressures. At a pump exit pressure of 5000 atm the isentropic pump enthalpy rise calculated using Curve C is approximately 50 percent greater than that using Curves A or B.

TURBOPUMP CHARACTERISTICS

Method of Analysis

Sketches illustrating the three different turbopump cycles which have been employed in the analytical studies are shown in Fig. 4. In the topping cycle, all of the power necessary to drive the pump is obtained by expanding all of the gases discharging from the heat exchanger through the primary turbine. In the bleed cycle, the primary turbine is omitted and the power to drive the pump is obtained by bleeding a fraction of the flow, W_B/W_O, through a bleed turbine. In the mixed cycle, half of the power required to drive the pump is obtained from the primary turbine, while the remainder of the power is obtained from the bleed turbine which obtains its inlet gases from the exit of the primary turbine. The bleed turbine pressure ratio, P_5/P_4, is assumed to be 0.01 for both the bleed and mixed cycles.

The energy required to raise the temperature of the hydrogen from that at the pump exit to that at the turbine inlet is obtained by cooling the moderator of the gaseous nuclear rocket engine. As noted in Ref. 8, this temperature rise may be obtained by piping the pump exit flow directly through the moderator, or may be obtained indirectly from an intermediate coolant loop which transfers the energy deposited in the moderator to an external heat exchanger through which the pump exit flow would pass. In the direct cycle, the relatively weak structural moderator material must withstand the forces generated by the difference between the turbine inlet pressure and the turbine exit pressure. In the indirect cycle, the pressure of the fluid used to cool the moderator is made approximately equal to the pressure in the engine, so that the pressure difference across the walls of the external heat exchanger is approximately equal to the pressure drop across the turbine. Since the external heat exchanger can be made from materials which are chosen without regard for their neutron absorbing characteristics, the stresses due to the pressure differences across the tube walls in the external heat exchanger are much easier to handle than are the stresses due to pressure differences within the moderator with the direct cycle. Therefore, it is assumed in the present report that the indirect cycle is employed to obtain the energy necessary to heat the hydrogen from pump exit pressure to turbine inlet pressure. However, it is still desirable to minimize the pressure drop across the turbine in order to minimize the stresses in the external heat exchanger used in the indirect cycle.

Calculations have been performed for a range of efficiencies in both the pump and turbine. The pump efficiency is defined as the ideal enthalpy rise associated with isentropic compression between the pump inlet pressure and the pump exit pressure (Fig. 3) divided by the actual enthalpy rise between these two pressures. The turbine efficiency is defined as the actual enthalpy drop through the turbine divided by the enthalpy drop which would be obtained by isentropic expansion between the turbine inlet pressure and turbine exit pressure. In calculations of the characteristics of the mixed cycle, the efficiency of the primary turbine and the secondary turbine have been assumed to be equal.

Results of Analysis

Topping Cycle

The results of the analysis of the topping cycle are given in Figs. 5 through 8 for turbine inlet temperatures of 1,400, 2,200, 3,000, and 3,800 R, respectively. For each temperature the pressure drop across the primary turbine is plotted as a function of engine inlet pressure. The pressure drop across the primary turbine is of interest because this pressure difference must be withstood by the tube walls in the heat exchanger used to transfer heat from the moderator in the gaseous nuclear rocket (see preceding section and Ref. 8). Also shown on each figure are lines of constant turbine inlet pressure. This pressure is of interest because it represents the pressure which must be withstood by the case surrounding the heat exchanger. The engine inlet pressure increases with an increase in turbine inlet pressure only up to a certain value of turbine inlet pressure. Above this value, an increase in turbine inlet pressure results in a decrease in engine inlet pressure. No information is shown on Figs. 5 through 8 for the region in which an increase in turbine pressure results in a decrease in engine inlet pressure.

Since it is desirable to minimize the pressure drop through the turbine, it is of interest to determine turbopump characteristics for specified values of the maximum allowable pressure drop across the turbine. Plots showing the variation of engine inlet pressure with turbine inlet temperature for assumed values of turbine pressure drop of 100, 300, and 1,000 atm are given in Fig. 9. Since the variation of maximum engine inlet pressure with turbine inlet temperature is small, it probably will not be desirable to employ extremely high values of turbine inlet temperatures. It is probable that any turbine developed in the near future for use with gaseous nuclear rockets will have turbine inlet temperatures limited to values which are now current for turbojet engines (2,000 to 2,500 R). Pump and turbine efficiencies of 80 and 90 percent, respectively, are also common for turbojet engines. For these pump efficiencies and a turbine inlet temperature of 2,200 R, it can be seen from Fig. 6 that turbine pressure drops of approximately 500 atm are required to obtain an engine inlet pressure of 1,000 atm.

The calculations shown in Fig. 6 for a turbine inlet temperature of 2,200 R and zero pressure drop in the heat exchanger have also been carried out using pump enthalpy Curves B and C in Fig. 3. The results of the calculations are shown in Fig. 10. It can be seen from this figure that the uncertainty in the hydrogen characteristics employed in the pump portion of the cycle has almost no effect on the turbopump performance at low values of engine inlet pressure, and a large effect on turbopump characteristics at high values of engine inlet pressure only by changing from either Curve A or B to Curve C.

Bleed Cycle

The results of calculations of the characteristics of the bleed cycle are shown in Figs. 11 through 14 for bleed turbine inlet temperatures of 1,400, 2,200, 3,000, and 3,800 R, respectively. In each figure, the fraction of bleed flow required is shown as a function of engine inlet pressure. This fraction of bleed flow is of interest because it governs the loss in specific impulse which would result from the use of a bleed cycle. If this bleed flow were exhausted overboard at zero temperature (i.e., with zero velocity), the fractional loss in specific impulse would be equal to the fraction of bleed flow. If zero-temperature bleed exhaust flow were mixed uniformly with the primary engine exhaust flow, the fractional loss in specific impulse would be approximately half of the bleed flow fraction. Since there is a finite temperature to the bleed exhaust flow (approximately 30 percent of bleed turbine inlet temperature), the actual loss in specific impulse would be less than that with zero bleed exhaust temperature. Thus, 10 percent bleed flow would result in something less than 5 to 10 percent loss in specific impulse.

A summary of the maximum engine inlet pressures obtainable using the bleed cycle is shown in Fig. 15 as a function of turbine inlet temperature for bleed flow fractions of 10 and 25 percent. The increase in engine inlet pressure with an increase in turbine inlet temperature for the bleed cycle shown in Fig. 15 is greater than that shown for the topping cycle in Fig. 9. Therefore, greater gains will be obtained by an increase in turbine inlet temperature using the bleed cycle than using the topping cycle. For conditions representative of those obtainable in turbojet engines (turbine inlet temperature of 2,200 R, pump efficiency of 80 percent, and turbine efficiency of 90 percent), it can be seen from Fig. 12 that approximately 7 percent bleed flow is required to obtain an engine inlet pressure of 500 atm and approximately 12 percent bleed flow is required to obtain an engine inlet pressure of 1000 atm.

Calculations to determine the effect of using Curves B or C instead of Curve A in Fig. 3 were also performed for the bleed cycle, and the results of these calculations are shown in Fig. 16. The influence of assumed pump enthalpy characteristics was somewhat less on the results for the bleed cycle than on the results for the topping cycle (see Fig. 10) because the turbine inlet pressures were lower for the bleed cycle than for the topping cycle.

Mixed Cycle

The results of calculations of the characteristics of the mixed cycle are shown in Figs. 17 through 24 for primary turbine inlet temperatures of 1400, 2200, 3000, and 3800 R. All calculations were carried out for a cycle in which half of the work required to drive the pump was obtained from the primary turbine and the remaining half of the work was obtained from the bleed turbine. Both the pressure drop across the primary turbine (Figs. 17, 19, 21 and 23) and the fraction of bleed flow required (Figs. 18, 20, 22 and 24) are shown as a function of engine inlet pressure. Comparison of the information on Figs. 17 through 24 with that shown on Figs. 5 through 8 and Figs. 11 through 14 indicates that, for the mixed cycle, the turbine pressure drops are less than in the topping cycle, and that the bleed flow fractions are less than for the bleed cycle.

The effect of turbine inlet temperature on the maximum value of engine inlet pressure is shown in Fig. 25 for fixed values of pressure drop across the primary turbine. Bleed flow fractions from Figs. 18, 20, 22 and 24 for each of these primary turbine pressure drops are shown in Fig. 26. It can be seen from Fig. 25 that the maximum values of engine inlet pressure are 50 to 100 percent higher than are shown in Fig. 9 for the topping cycle, at an expense of a penalty in bleed flow.

REFERENCES

1. Rohlik, Harold E., and James E. Crouse: Analytical Investigation of the Effect of Turbopump Design on Gross Weight Characteristics of a Hydrogen-Propelled Nuclear Rocket. NASA Memo 5-12-59E, June 1959.

2. Whitney, Warren J.: Analysis of Turbopump Feed Systems for Hydrogen-Nuclear Rockets. NASA TN D-2712, March 1965.

3. Woolley, H. W., R. B. Scott, and F. G. Brickwedde: Compilation of the Thermal Properties of Hydrogen in Its Various Isotopic and Ortho-Para Modifications. Journal of Research NBS, Vol. 41, 1948, p. 379, RP 1932.

4. Michels, A., and M. Goudeket: Compressibilities of Hydrogen Between 0°C and 150°C Up to 3000 Atmospheres. Physica VIII, No. 3, 1941, p. 347.

5. Michels, A., W. DeGraaff, and G. J. Wolkers: Thermodynamic Properties of Hydrogen and Deuterium at Temperatures Between -175°C and 150°C and at Pressures Up to 2500 Atmospheres. Applied Science Research, Section A, Vol. 12, p. 9.

6. Hirschfelder, J. O., C. F. Curtiss, and R. B. Bird: Molecular Theory of Gases and Liquids. John Wiley & Sons, Inc., New York, 1954.

7. Roder, H. M., and R. D. Goodwin: Provisional Thermodynamic Functions for Parahydrogen. National Bureau of Standards TN 130 (PB161631), December 1961.

8. McLafferty, G. H.: Analytical Study of Moderator Wall Cooling of Gaseous Nuclear Rocket Engines. UAC Research Laboratories Report C-910093-9 prepared under Contract NASw-847, September 1964.

9. Weinstein, H., and R. Ragsdale: A Coaxial Flow Reactor--A Gaseous Nuclear-Rocket Concept. ARS Preprint 1518-60, presented at the ARS 15th Annual Meeting, Washington, D. C., December 1960.

10. Krascella, N. L.: Theoretical Investigation of the Opacity of Heavy-Atom Gases. UAC Research Laboratories Report D-910092-4 prepared under Contract NASw-847, September 1965.

11. Ragsdale, Robert G., Herbert Weinstein, and Chester D. Lanzo: Correlation of a Turbulent Air-Bromine Coaxial-Flow Experiment. NASA Tech. Note D-2121, February 1964.

12. Latham, T. S., and L. O. Herwig: Effect of Hot Hydrogen Propellant on the Critical Mass of Gaseous Nuclear Rocket Cavity Reactors. UAC Research Laboratories Report UAR-D70 prepared for presentation at the AIAA Nuclear Propulsion Specialists Conference on June 14-18, 1965.

13. Hughes, D. J., and R. B. Schwartz: Neutron Cross Sections, BNL-325, Brookhaven National Laboratory, July 1958.

14. Reactor Physics Constants, ANL-5800, Argonne National Laboratory, July 1963.

LIST OF SYMBOLS

(Excludes Symbols Employed in Appendixes)

b_1, b_2, b_3	Empirical constants (see Table I for values and units)
$B(T)$	Second virial coefficient, $cm^3/g.mole$
$\tilde{B}(T)$	Statistical mechanical second virial coefficient (see Eq. (11)), $cm^3/g.mole$
C_1, C_2	Empirical constants (see Table I for values and units)
C_P	Specific heat at constant pressure, cal/g.mole-deg K
$C^o_{P_{IDEAL}}$	Specific heat at constant pressure for ideal gas, cal/g.mole-deg K
$C(T)$	Parameter related to the third virial coefficient (see Eq. (6))
$\tilde{C}(T)$	Statistical mechanical third virial coefficient (see Eq. (12)), $(cm^3/g.mole)^2$
F	Fraction of pump work obtained by expansion of flow through primary turbine
g	Electronic degeneracy
$\hbar$	Planck's constant = 1.054×10^{-27} erg sec
H	Enthalpy, cal/g, Btu/lb, or ft-lb/lb
H^o_{IDEAL}	Enthalpy for ideal gas, cal/g, Btu/lb, or ft-lb/lb
$(\Delta H_P)_i$	Isentropic enthalpy rise in pump, Btu/lb or ft-lb/lb
I_e	Moment of inertia, $g\text{-}cm^2$
k	Boltzmann's constant = 1.3804×10^{-16} erg/deg K
N	Avogadro's number, 6.0248×10^{23} molecules/g.mole
P	Pressure, atm or lb/ft^2

$P_{4_{MAX}}$	Maximum value of engine inlet pressure for specified turbine pressure drop or bleed flow fraction, atm
ΔP_P	Pressure rise across pump, $P_2 - P_1$, atm
ΔP_{HE}	Heat exchanger pressure drop between pump exit and turbine inlet, $P_2 - P_3$, atm
ΔP_T	Pressure drop across primary turbine, $P_3 - P_4$, atm
Q_r	Rotational partition function
r	Intermolecular separation, cm
r_e	Value of r at equilibrium separation, cm
R	Universal gas constant = 82.06 cc-atm/g.mole-deg K
S	Entropy, cal/g-deg K or Btu/lb-deg R
S^O_{IDEAL}	Entropy for ideal gas, cal/g-deg K or Btu/lb-deg R
T	Temperature, deg K or deg R
V	Specific volume, cm^3/g or ft^3/lb
W_B	Flow rate through bleed turbine, lb/sec
W_E	Flow rate to engine, lb/sec
W_O	Flow rate through pump, $W_B + W_E$, lb/sec
Z	Compressibility factor
ϵ_j	Energy of the $j^{\underline{TH}}$ quantum state, erg
$\epsilon(r)$	Interatomic potential energy, erg
η_B	Efficiency of bleed turbine (assumed equal to η_P in all calculations)
η_P	Pump efficiency
η_T	Turbine efficiency

ρ Density, g.moles/cm^3, Amagat, or lb/ft^3 (for hydrogen, 1 Amagat = 0.0056115 lb/ft^3)

σ Dimensionless parameter, see Eq. (3)

Subscripts

j Quantum state j

1 Pump inlet

2 Pump exit

3 Inlet of primary turbine

4 Engine Inlet

5 Exit of secondary turbine

APPENDIX I

APPROXIMATE TEMPERATURE DISTRIBUTION IN FUEL-CONTAINMENT REGION OF A COAXIAL-FLOW GASEOUS NUCLEAR ROCKET ENGINE

Symbols Employed in Appendix I

a_R	Rosseland mean opacity, ft^{-1} or cm^{-1}
C_1	Heat creation rate per unit volume in fuel region, $Btu/sec\text{-}ft^3$
K	Radiation thermal conductivity, Btu/sec-ft-deg R
q	Heat flux per unit length of fuel-containment region, Btu/sec-ft
Q	Radial heat flux, $Btu/sec\text{-}ft^2$
Q_e	Value of Q at outside edge of fuel-containment region, $Btu/sec\text{-}ft^2$
R	Local radius, ft
R_e	Radius at outside edge of cylindrical fuel-containment region, ft
T	Temperature, deg R
$T_{℄}$	Centerline temperature, deg R
T_e	Temperature at outside edge of fuel-containment region, deg R
T^*	Black-body radiating temperature which will produce heat flux equal to Q_e, deg R
σ	Stefan-Boltzmann constant, 0.48×10^{-12} $Btu/sec\text{-}ft^2\text{-}(deg\ R)^4$

A simplified procedure has been developed for calculating the temperature distribution in the fuel-containment region of a coaxial-flow gaseous nuclear rocket engine (see Ref. 9). The radiant heat transfer per unit length passing a given radius in the fuel-containment region of such an engine is given by the following equation.

$$q = 2\pi R Q \tag{I-1}$$

If it is assumed that the energy creation rate per unit volume within the fuel-containment region is constant and that convection and molecular conduction effects are negligible, then the radiant heat transfer per unit length at a given radius is proportional to the volume inside of that radius.

$$q = C_1 \pi R^2 \tag{I-2}$$

Combining Eqs. (I-1) and (I-2) yields

$$Q = \frac{C_1}{2} R \tag{I-3}$$

As a boundary condition, assume that the heat flux at the outside edge of the fuel region, $R = R_e$, is equal to the black-body heat flux at a fictitious temperature, T^*. That is,

$$Q_e = \sigma T^{*4} \tag{I-4}$$

Therefore,

$$Q = \frac{R}{R_e} \sigma T^{*4} \tag{I-5}$$

According to diffusion analysis, the radiant heat flux is given by the following expression:

$$Q = -K \frac{dT}{dR} \tag{I-6}$$

where

$$K = \frac{16}{3} \frac{\sigma T^3}{a_R} \tag{I-7}$$

Combining Eqs. (I-5), (I-6), and (I-7) yields

$$\left(\frac{-16}{3 a_R} \right) T^3 \frac{dT}{dR} = \frac{T^{*4}}{R_e} R \tag{I-8}$$

The solution to this equation for a_R = constant and with the temperature at the outside edge of the fuel region set at a value equal to T_e is

$$\frac{T}{T^*} = \sqrt[4]{\left(\frac{T_e}{T^*}\right)^4 + \frac{3}{8}\, a_R\, R_e \left[1 - \left(\frac{R}{R_e}\right)^2\right]} \qquad \text{(I-9)}$$

An example which is of interest to personnel at the NASA Lewis Research Center is one in which the radius, R_e, equals 2 ft and the Rosseland mean opacity, a_R, equals 100 ft^{-1}. Calculated variations of T/T^* with R/R_e are given in Fig. 27 for two different values of T_e/T^*.

The effect of the dimensionless fuel opacity, $a_R R_e$, on the ratio of $T_{\mathbb{C}}/T^*$ is given in Fig. 28 for two different values of T_e/T^*. It can be seen that the temperature ratio is relatively insensitive to $a_R R_e$.

The radiant heat fluxes of interest in a coaxial-flow gaseous nuclear rocket correspond to values of black-body radiating temperature, T^*, on the order of 30,000 R. Therefore, on the basis of the results shown on Figs. 27 and 28, the temperatures near the centerline of such an engine would be considerably higher than 30,000 R. Information on the Rosseland mean opacity of gaseous nuclear fuel is presented in Ref. 10. According to Ref. 10, the Rosseland mean opacity at a temperature of 30,000 R is between approximately 100 and 1000 cm^{-1} at pressures of 100 to 1000 atm, and is between 2 and 20 cm^{-1} at a temperature of 150,000 R and a pressure between 100 and 1000 atm. If the "average" opacity is assumed to be between 10 and 100 cm^{-1}, and the radius, R_e, is assumed to be 2 ft (61 cm), resulting values of $a_R R_e$ of interest are between 600 and 6000. According to Fig. 28, this would lead to centerline temperatures between 4 and 7 times the effective radiating temperatures, or between 120,000 R and 210,000 R for the example being considered. Therefore, it appears that the temperature at the centerline of a coaxial-flow gaseous nuclear rocket will be between approximately 100,000 and 200,000 R.

APPENDIX II

CHANGE OF FORM OF NASA LEWIS HEAVY-GAS CONTAINMENT DATA FROM COAXIAL-FLOW TESTS

Symbols Employed in Appendix II

C^*	Ratio of average concentration at arbitrary value of Z divided by concentration at Z = 0 as determined from Ref. 11 by measuring the attenuation in single light beam passing through center of bromine flow
$\overline{C^*}$	Average value of C^* between Z = 0 and Z = Z
d_O	Equivalent diameter of duct employed in Ref. 11, 4.56 in. or 0.380 ft
K	Constant - see Eq. (II-5)
L	Length of cavity in gaseous nuclear rocket engine (see Fig. 29), ft
r_1	Radius of cavity in gaseous nuclear rocket engine and length of region in model tests used to evaluate C^* (see Fig. 29), ft
r_6	Radius of bromine injection duct in model tests or fuel injection duct in gaseous nuclear rocket engine, ft
Re_A	Air Reynolds number, $\rho_A V_A d_O/\mu_A$
Re_B	Bromine Reynolds number, $2\rho_B V_B r_6/\mu_B$
Re_Z	Axial-flow Reynolds number, $\rho_A V_A r_1/\mu_A$
t_B	Bromine time constant, w_B/W_B
V_A	Air velocity at Z = 0, ft/sec
V_B	Bromine velocity at Z = 0, ft/sec
W_A	Air flow, lb/sec
W_B	Bromine flow, lb/sec
w_B	Weight of bromine between Z = 0 and Z = Z, lb

Z	Distance from end of bromine injection duct, ft or in.
ϵ	Eddy viscosity, ft^2/sec
μ	Molecular viscosity of mixture, lb/sec-ft
μ_A	Air viscosity, 1.2×10^{-5} lb/sec-ft
μ_B	Bromine viscosity, 0.988×10^{-5} lb/sec-ft
ρ	Mixture density, lb/ft^3
ρ_A	Air density at $Z = 0$, lb/ft^3
ρ_B	Local bromine density, lb/ft^3
ρ_{B_O}	Bromine density at $Z = 0$, lb/ft^3
$\bar{\rho}_B$	Average bromine density, $\mathcal{M}_B / \pi r_1^2 L$
τ_B	Dimensionless bromine time constant, $t_B / (\rho_A r_1^2 / \mu_A)$

The results of tests conducted at the NASA Lewis Research Center to determine the characteristics of a coaxial-flow gaseous nuclear reactor (see Ref. 11) are in a form which is not easily used in a gaseous nuclear reactor performance analysis method which is being employed at the UAC Research Laboratories. This analysis method employs three dimensionless parameters: an axial-flow Reynolds number, Re_Z; a dimensionless time constant, τ_B; and a dimensionless density ratio, $\bar{\rho}_B / \rho_A$. The relation between each of these parameters and the data from Ref. 11 is developed in the following paragraphs. All dimensions employed are illustrated in Fig. 29, and the data from Ref. 11 are summarized in Table II.

The first parameter is Re_Z, which is defined as follows:

$$Re_Z = \frac{\rho_A V_A r_1}{\mu_A} \tag{II-1}$$

On the basis of the definition of Re_A employed in Ref. 11, Re_Z can be determined as follows:

$$Re_Z = \frac{r_1}{d_O} \left(\frac{\rho_A V_A d_O}{\mu_A} \right) = \frac{r_1}{d_O} Re_A \tag{II-2}$$

The values of Re_Z given in Table II have been determined for $d_0 = 4.56$ in. and $r_1 = 0.287$ in. (i.e., $r_6/r_1 = 0.75$), which yields a value of $r_1/d_0 = 0.0630$. The value of d_0 of 4.56 in. was determined from values of Re_A, V_A, μ_A, and W_A from Ref. 11. All evaluations of parameters from the results of Ref. 11 are valid only for values of r_6/r_1 which are sufficiently small that the mixing of gases near the axis has no influence on the velocity and concentration at radius r_1, and only if the change in the position of the outer wall to radius r_1 has no influence on the flow pattern inside radius r_1. Insufficient information is presented in Ref. 11 to determine whether this criterion is satisfied for r_6/r_1 of 0.75 (the value assumed in determining some of the information in Table II).

It is convenient to employ a fuel or bromine time constant which is a measure of the average length of time which the heavy gas remains in the cavity of a gaseous nuclear rocket engine. This time constant is defined as follows:

$$t_B = \frac{\mathcal{W}_B}{W_B} = \frac{\bar{\rho}_B \pi r_1^2 L}{\rho_{B_0} \pi r_6^2 V_B} = \left(\frac{\bar{\rho}_B}{\rho_{B_0}}\right)\left(\frac{r_1}{r_6}\right)^2\left(\frac{L}{r_1}\right)\left(\frac{V_A}{V_B}\right)\left(\frac{r_1}{V_A}\right) \qquad \text{(II-3)}$$

or

$$t_B = K \frac{r_1}{V_A} \qquad \text{(II-4)}$$

where

$$K = \left(\frac{\bar{\rho}_B}{\rho_{B_0}}\right)\left(\frac{r_1}{r_6}\right)^2\left(\frac{L}{r_1}\right)\left(\frac{V_A}{V_B}\right) \qquad \text{(II-5)}$$

The time constant determined in model tests can be scaled to determine the time constant in a full-scale engine if the configurations are dynamically similar; that is, if all pertinent dimensionless parameters in the two configurations are equal. These parameters include geometric length ratios, Reynolds numbers, Froude number, molecular weight ratio, laminar and turbulent Schmidt numbers, and dimensionless temperature distribution. If two configurations are dynamically similar, it can be shown that the ratio of any velocity to any other velocity and the ratio of any density to any other density are fixed. Therefore, for dynamically similar configurations, it can be seen that the parameter K in Eq. (II-5) is fixed and, hence, that the time constant for dynamically similar configurations is proportional to r_1/V_A according to Eq. (II-4).

The absolute velocity in Eq. (II-4) can be eliminated by substitution from the definition of Reynolds number in Eq. (II-1) as follows:

$$t_B = K r_1 \left(\frac{\rho_A r_1}{\mu_A Re_Z} \right) = \frac{\rho_A r_1^2}{\mu_A} \frac{K}{Re_Z} \qquad \text{(II-6)}$$

Since dynamic similarity also requires that Reynolds number be fixed, it is convenient to define a dimensionless time constant, τ_B , as follows:

$$\tau_B = \frac{t_B}{\left(\frac{\rho_A r_1^2}{\mu_A} \right)} = \frac{K}{Re_Z} \qquad \text{(II-7)}$$

This dimensionless time constant should be fixed for dynamically similar configurations.

From Eqs. (II-3) and (II-7),

$$\tau_B = \frac{t_B}{\left(\frac{\rho_A r_1^2}{\mu_A} \right)} = \frac{\mathscr{W}_B}{W_B \left(\frac{\rho_A r_1^2}{\mu_A} \right)} \qquad \text{(II-8)}$$

The dimensionless time constant, τ_B , in Eqs. (II-7) and (II-8) must be determined from experiments.

The third parameter in the engine performance analysis method is the density ratio, $\bar{\rho}_B / \rho_A$, which is defined as follows:

$$\frac{\bar{\rho}_B}{\rho_A} = \frac{1}{\rho_A} \frac{\mathscr{W}_B}{\pi r_1^2 L} \qquad \text{(II-9)}$$

Evaluation of Eqs. (II-3), (II-8), and (II-9) requires knowledge of the amount of bromine stored within the simulated cavity region of a gaseous nuclear rocket engine. Although insufficient measurements were obtained in the tests reported in Ref. 11 to determine this quantity exactly, a technique has been adopted which results in approximate values of $\mathscr{W}_B$. In this technique, an average value of C^* is employed, where

$$\overline{C^*} = \frac{1}{L} \int_0^L C^* dZ \qquad \text{(II-10)}$$

It has been assumed that

$$\mathscr{W}_B = \bar{C}^* \rho_{B_0} \pi r_6^2 L \tag{II-11}$$

Equation (II-11) is only approximate because the measurement of local average concentration, C*, in Ref. 11 was made using a light beam which passed only through the centerline of the bromine flow. This difficulty in determining true average concentration has been avoided in the reduction of data at the NASA Lewis Research Center by comparing the variation of measured C* with distance to calculated variations of C* with distance determined from an analysis of the rate of diffusion of the gases for fixed values of eddy viscosity. The true average concentration is then determined from an integration of the variation of theoretical concentration with radius for the eddy viscosity which provides the best match with the measured variation of C* with axial distance. A check on the validity of Eq. (II-11) has been made on the basis of data from nine such theoretical runs which have been furnished by Mr. Robert Ragsdale of the NASA Lewis Research Center. The true amount of flow stored was within 10 percent of that indicated by Eq. (II-11) for Runs 6, 9, 10, and 11 from Ref. 11. However, the true value was less than that indicated by Eq. (II-11) by between 25 and 35 percent for Runs 13, 15, 16, and 18, and by approximately 50 percent for Run 20. Therefore, Eq. (II-11) overestimates the weight of heavy gas stored within a given length.

Integrations have been made of experimental data reported in Ref. 11 to determine values of $\bar{C}^*$ for three different values of L/r_6. The results of these integrations are given in Table II along with values of $\bar{\rho}_B/\rho_A$ and τ_B evaluated from $\bar{C}^*$ and Eqs. (II-8), (II-9), and (II-11). Also shown on this table are values of Re_Z determined from Eq. (II-2). All values of $\bar{\rho}_B/\rho_A$, τ_B, and Re_Z in Table II were determined for $r_6/r_1 = 0.75$. Examination of Eqs. (II-2), (II-8), and (II-9) indicates that changes in the assumed value of r_6/r_1 would result in the following:

$$\tau_B \sim \left(\frac{r_6}{r_1}\right)^2 \tag{II-12}$$

$$\frac{\bar{\rho}_B}{\rho_A} \sim \left(\frac{r_6}{r_1}\right)^2 \tag{II-13}$$

$$Re_Z \sim \frac{1}{(r_6/r_1)} \tag{II-14}$$

All values of τ_B and $\bar{\rho}_B/\rho_A$ from Table II have been plotted as a function of Reynolds number in Figs. 30 and 31 for a value of $L/r_6 = 8$. Values of τ_B and $\bar{\rho}_B/\rho_A$ for selected runs are plotted in Figs. 32 and 33 as a function of L/r_1. All dimensionless time constants are plotted in Fig. 34 as a function of $\bar{\rho}_B/\rho_A$ for a value of $L/r_6 = 8$. Separate symbols have been employed in Fig. 34 for each range of Reynolds number.

The correlation of the data in Ref. 11 indicates that the total viscosity (sum of eddy and molecular viscosities) is related to Reynolds number as follows:

$$\frac{\rho\epsilon+\mu}{\mu} = 1+0.0172\left(\frac{V_A}{V_B}-1\right)^{1/2}\left(Re_B - 250\right) \tag{II-15}$$

For large values of Re_B and Re_A, Eq. (II-15) reduces to

$$\frac{\rho\epsilon+\mu}{\mu} \approx 0.0172\left(\frac{V_A}{V_B}-1\right)^{1/2} Re_B \tag{II-16}$$

For conditions for which Eq. (II-16) is valid, it can be shown that the ratio of any velocity to any other velocity is independent of all Reynolds numbers for fixed values of V_A/V_B, and for fixed values of other dynamic similarity parameters. Under these conditions, the parameter K in Eq. (II-7) is independent of Reynolds number and

$$\tau_B \sim \frac{1}{Re_Z} \tag{II-17}$$

Equation (II-17) is valid only for fixed values of V_A/V_B. Calculations based on Table II indicate that V_A/V_B is approximately equal to 3.0 for Runs 6, 10, and 11, and is approximately equal to 9.0 for Runs 13, 16, and 18. It can be seen from Fig. 30 that the variation of τ_B with Re_Z for each of these two sets of data is approximately as indicated by Eq. (II-17).

APPENDIX III

HEAT GENERATION RATE IN FUEL PASSING THROUGH FUEL-INJECTION DUCT LOCATED IN MODERATOR OF GASEOUS NUCLEAR ROCKET ENGINE

Symbols Employed in Appendix III

A	Cross sectional area of fuel-injection duct, ft^2
B	$\bar{Q}/Q_c$ (see Fig. 39)
ΔH_f	Enthalpy rise of fuel in passing through fuel-injection duct, Btu/lb
ℓ_m	Moderator thickness, ft or cm
Q	Rate of heat generation in fuel within fuel-injection duct, Btu/lb-sec
$\bar{Q}$	Average rate of heat generation in fuel within fuel injection duct, Btu/lb-sec
Q_c	Rate of heat generation in fuel within cavity, Btu/lb-sec
r_i	Inside radius of fuel-injection duct, cm or in.
r_o	Outside radius of sleeve surrounding fuel-injection duct, cm or in.
Δr	Slant thickness of fuel-injection sleeve, $\Delta r_n/\cos\phi$, cm or in.
Δr_n	Thickness of fuel-injection sleeve normal to axis plane, cm or in. (see Fig. 35)
$\overline{\Delta r_n}$	Average thickness of fuel-injection sleeve normal to axis plane, cm or in.
t	Time, sec
t_{fs}	Dwell time of fuel in fuel-injection duct for constant fuel velocity along fuel-injection duct, sec
V_f	Velocity of fuel passing through fuel injection duct, ft/sec
W_f	Weight flow of U-233 fuel, lb/sec

x Distance from outside edge of moderator, cm or ft

y Distance from inside edge of moderator, cm or ft

y_e Effective fuel-exposure length of fuel-injection duct for heating due to uncollided neutrons from cavity, cm or ft

θ_1 Angle shown on Fig. 35, deg

θ_2 Angle shown on Fig. 35, deg

ρ_f Fuel density in carrier gas, lb/ft^3

Σ_a Macroscopic absorption cross section of sleeve wall material, cm^{-1}

Σ_f Macroscopic fission cross section of nuclear fuel, cm^{-1}

Φ_B Neutron flux at cavity-moderator boundary, neutrons/cm^2-sec

Φ_i Neutron flux inside hafnium fuel injection duct, neutrons/cm^2-sec

Φ_o Neutron flux outside hafnium fuel injection duct, neutrons/cm^2-sec

ϕ Angle shown on Fig. 35, deg

Many gaseous nuclear rocket concepts, such as the concept described in Ref. 9, require that fuel be injected separately from the propellant through a fuel-injection duct located in the moderator of the engine into the engine cavity. The configuration employed in the following analysis of the heat generation in the fuel while in the fuel-injection duct is given in Fig. 35. It is assumed that the fuel-injection duct is surrounded by a sleeve made of a material such as hafnium which will absorb a large fraction of the neutrons passing into the fuel-injection sleeve. The analysis in the following subsections first considers the neutron flux which passes through the sleeve, and then considers the uncollided neutron flux which passes from the cavity into the open end of the duct exposed to the cavity. These two sources of heat generation are then added to obtain the overall heat generation rate in the fuel within the fuel-injection duct. Finally, the effect on critical mass of the presence of the neutron poison in the fuel-injection duct sleeve is estimated.

Heat Generation Rate Due to Neutron Flux Passing Through Sleeve

It is assumed that the scattering of neutrons by the sleeve surrounding the fuel-injection duct is negligible, that the length of the sleeve is effectively infinite, and that the neutron flux approaching the sleeve is isotropic. It is also assumed that the thickness of the sleeve is small compared to the neutron mean-free path outside the sleeve such that the flux depression in the moderator caused by the sleeve is negligible. This latter assumption results in a slight overestimation of the flux within the sleeve.

The ratio of the neutron flux within the sleeve to the flux outside the sleeve is derived using Fig. 35.

$$\ell = r_i \sin\theta_2 = r_0 \sin\theta_1 \tag{III-1}$$

$$\Delta r = \frac{r_0\cos\theta_1 - r_i\cos\theta_2}{\cos\phi} \tag{III-2}$$

where ϕ is the angle between the plane normal to the axis of the cylindrical absorber and any oblique plane through the sleeve shown in Fig. 35. Thus,

$$\Delta r = \frac{1}{\cos\phi}\left[r_0(1-\sin^2\theta_1)^{1/2} - (r_i^2 - r_0^2\sin^2\theta_1)^{1/2}\right] = \frac{1}{\cos\phi}\left[(r_0^2-\ell^2)^{1/2} - (r_i^2-\ell^2)^{1/2}\right] \tag{III-3}$$

Consider a band of unit area on the outer surface of the cylindrical absorber of width, $2r_i$. The ratio of flux inside the cylindrical absorber to flux outside the absorber is given by

$$\frac{\Phi_i}{\Phi_0} = \frac{\int_{\phi=0}^{\pi/2}\int_{\ell=0}^{r_i} e^{-\Sigma_a \Delta r}\cos\phi\, d\ell\, d\phi}{\int_{\phi=0}^{\pi/2}\int_{\ell=0}^{r_i} \cos\phi\, d\ell\, d\phi} \tag{III-4}$$

For simplicity, assume that

$$e^{-\Sigma_a \Delta r} = e^{-\Sigma_a(\overline{\Delta r}_n/\cos\phi)} \tag{III-5}$$

where $\overline{\Delta r_n}$ is a constant for a selected geometry given by the following equations.

$$\overline{\Delta r_n} = \frac{\int_{\ell=0}^{r_i} \Delta r_n \, d\ell}{\int_{\ell=0}^{r_i} d\ell} = \frac{\int_{\ell=0}^{r_i} \left[(r_o^2 - \ell^2)^{1/2} - (r_i^2 - \ell^2)^{1/2} \right] d\ell}{r_i} \tag{III-6}$$

$$\overline{\Delta r_n} = \frac{(r_o^2 - r_i^2)}{2} + \frac{r_o^2}{2 r_i} \sin^{-1} \frac{r_i}{r_o} - \frac{\pi}{4} r_i \tag{III-7}$$

Δr_n and $\overline{\Delta r_n}$ are distinguished from Δr in that $\phi = 0$ (plane normal to sleeve axis shown in Fig. 35) for Δr_n and $\overline{\Delta r_n}$. This approximation is accurate as long as $\overline{\Delta r_n}$ does not differ greatly from $(r_o - r_i)$. For the cases of interest in this work, r_i / r_o varies between 0.0 and 0.5 and, over this range, the ratio of $\frac{\overline{\Delta r_n}}{r_o - r_i}$ varies from 1.0 to 1.13. The results of the calculations of the ratios of flux inside the absorber to flux outside, Φ_i/Φ_o, are shown in Fig. 36 for r_i/r_o = 0.0, 0.25 and 0.50.

Calculations of the neutron flux at different positions along the length of the fuel-injection duct have been made on the basis of a typical neutron flux distribution for the configuration shown on Fig. 35 using techniques described in Ref. 12. These calculations were made for a total of 19 radial stations in the moderator. Average values of neutron flux in each energy group and for each of the three major portions of the moderator are given in Table III. The calculations of flux within the fuel-injection duct have been made on the basis of the use of hafnium as a sleeve wall material. It is assumed that the hafnium is cooled by coolant ducts occupying ten percent of the hafnium volume. Average macroscopic hafnium absorption across sections obtained using Ref. 13 for each energy group are shown in Table IV. Also shown in Table IV are the macroscopic fission cross sections for U-233 fuel. The effect of self-shielding of neutrons by the nuclear fuel on the heat generation within the nuclear fuel was neglected.

The results of calculations of the local heat generation rate in the fuel within the fuel-injection duct relative to that for fuel in the cavity are shown in Fig. 37 for r_i = 0.04 in. with sleeve wall thicknesses of 0.0, 1.0, and 2.0 in. as a function of the distance from the outside edge of the moderator. The results shown on this figure were determined by summing the products of $(\Phi_i/\Phi_o)\,\Sigma_f\,\Phi_o$ for all 18 neutron energy groups at each of 19 different radial stations in the reflector moderator. The values of (Φ_i/Φ_o) were taken from Fig. 36 for each neutron energy group as a function of $\Sigma_a(r_o - r_i)$ for the particular energy group and hafnium sleeve thickness. Also shown in the table on Fig. 37 are average values of the heat generation rate within the fuel-injection duct relative to the heat generation rate in the fuel within the cavity. In calculating the heat generation rate within the fuel-injection duct, it was assumed that no neutron, gamma, or beta particle energy would be deposited in the fuel during injection due to the small dimensions of the inside of the injection tube and small residence time for the fuel within the tube. On the other hand, the heat generation rate for fuel within the cavity includes contributions from all energy sources, namely fission fragments, neutrons, gamma rays, and beta particles. On this basis, the ratio of heat generation rate within the fuel-injection duct to that in the cavity for identical neutron fluxes would be 0.88.

Heat Generation Due to Uncollided Flux from Cavity

A certain fraction of the flux near the cavity boundary will enter the end of the fuel-injection duct. Assuming an isotropic flux approaching the duct, the exposure of the fuel in the tube to uncollided flux from the cavity should be proportional to the solid angle subtended along the tube axis. The fission rate at any point y will be

$$\Sigma_f \phi_B \frac{\Omega}{4\pi} = \frac{\Sigma_f \Phi_B}{2} \left[1 - \frac{y}{(r_i{}^2 - y^2)^{1/2}} \right] \qquad \text{(III-8)}$$

where Φ_B is the neutron flux at the cavity-moderator boundary.

A plot showing the variation of local heat generation rate in the fuel-injection duct due to the uncollided flux from the cavity relative to that for fuel in the cavity is given in Fig. 38. In calculating Fig. 38 it was assumed that all flux from the moderator was absorbed by the sleeve. At the end of the fuel-injection duct ($y = 0$), the flux seen by the fuel is half that at the cavity-moderator boundary because the fuel in this region sees only the flux coming from the cavity direction, while the fuel in the cavity sees flux from all directions. Also, the heat created in the fuel within the fuel-injection duct is assumed to be that due to only fission fragments for the reasons discussed previously. Since the heat generation rate due to the fuel within the cavity is considered as that from all causes, the resulting heat generation rate in the fuel located at the exact exit of the fuel-injection duct is approximately 44% of the total heat generation rate of the fuel within the cavity.

The total heat generated within the fuel in the fuel-injection duct may be obtained by integrating the curve shown on Fig. 38. If such an integration is performed, a result is obtained which indicates that the total heat generated within the fuel-injection duct due to uncollided flux from the cavity is equal to that which would occur in a duct having a length equal to 0.447 r_i if this length were subjected to the full neutron flux in the cavity. This length, 0.447 r_i, is denoted as an effective fuel exposure length, y_e.

Total Heat Deposited in Fuel Within Fuel-Injection Duct

A series of calculations have been carried out to determine the total fuel heating rate as a function of sleeve wall thickness for internal sleeve radii of 0.04, 0.08, 0.2, and 0.4 in. This heating rate was determined by adding that due to flux passing through the sleeve (such as that shown in Fig. 37) to that due to the uncollided flux from the cavity (Fig. 38). The results of this calculation are shown in Fig. 39. It can be seen from this figure that, for sleeve thicknesses greater than approximately 0.5 in., a majority of the heat generation in the fuel occurs as a result of uncollided flux originating in the cavity rather than from flux which has passed through the sleeve. Minimization of the flux from the cavity would require the use of the smallest possible value of the inside diameter of the fuel-injection duct. An effective reduction in the diameter of this fuel-injection duct could be obtained by filling the downstream end of the duct with "egg crate" partitions made from hafnium. As noted on Fig. 39, all calculations of the flux passing through the sleeve were made on the basis of the use of hafnium as the sleeve wall material.

The overall enthalpy rise in the fuel in passing through the fuel-injection duct may be determined from the following equation.

$$\Delta H_f = \bar{Q}\, t_{fs} = B\, Q_C \frac{l_m}{V_f} \tag{III-9}$$

A typical value of heat deposition rate for fuel in the cavity is 5×10^6 Btu/lb-sec. For a fuel-injection duct having an inside radius of 0.04 in. and a physical wall thickness of 0.5 in., the ratio of energy release of fuel in the fuel-injection duct to that in the cavity, B, is 0.003 according to Fig. 39. Therefore, for this example,

$$B\, Q_C = \bar{Q} = 0.003\,(5 \times 10^6) = 1.5 \times 10^4 \text{ BTU/LB-SEC} \tag{III-10}$$

From Fig. 1, $l_m = 2$ ft. The fuel must pass through the fuel-injection duct rapidly enough so that the temperatures created in the fuel are acceptable. If this maximum temperature is assumed to be that for melting of the fuel-injection duct (~ 3600 R) the corresponding enthalpy would be approximately 150 Btu/lb. A carrier gas, probably hydrogen, would also be employed and might occupy 50% of the volume within the duct. However, the contribution of the energy absorption of the hydrogen relative to that of the mixture would be negligible. Therefore,

$$\Delta H_f = 150 \text{ BTU/LB}$$

If values for ΔH_f, $\bar{Q}$, and ℓ_m are substituted in Eq. (III-9), it is concluded that the minimum permissible velocity of the fuel in passing through the moderator, $(V_f)_{MIN}$, is

$$(V_f)_{MIN} = \frac{B\, Q_C\, \ell m}{\Delta H_f} = \frac{0.003\,(5 \times 10^6)\,(2.0)}{150} = 200 \text{ FT/SEC}$$

If V_f is less than 200 ft/sec, the temperature of the fuel at the end of the fuel duct will be greater than the assumed value of 3600 R. Note that the required fuel velocity would have been 66,700 ft/sec if the hafnium liner had not been employed ($B = 1.0$).

Knowing $V_{f_{MIN}}$, r_i, and the fuel density, ρ_F, at 3600 R and 1000 atm, the minimum injection rate of fuel, W_F, can be calculated. It is assumed that the density of the carrier gas, H_2, is negligible relative to particulate or condensed U-233 present at 50% by volume and therefore, from Ref. 14, $\rho_F = 575$ lb/ft^3. If $r_i = 0.1$ cm

$$W_{f_{MIN}} = \rho_F\, (V_f)_{MIN}\, A = (575)(200)(3.38 \times 10^{-5}) = 3.8 \text{ LB/SEC}$$

This fuel flow rate could obviously be reduced by employing a smaller volume fraction of fuel in the duct or by employing a smaller duct diameter.

Effect of Neutron Absorption in Sleeve on Critical Mass

The presence of a neutron-absorbing sleeve surrounding the fuel-injection duct will cause an increase in the critical mass of nuclear fuel required in the cavity. The neutron-absorbing sleeve of thickness greater than 0.5 cm will effectively remove all neutrons passing through an area equal to the external surface area of the sleeve. Corporate-sponsored studies have indicated that a neutron-absorbing area uniformly distributed throughout the moderator and equal to 1% of the cavity surface area will result in an increase in critical mass of approximately 25%. This information has been used to construct Table V. It can be seen that care must be taken to minimize the diameter of the sleeve surrounding the fuel-injection duct in order to minimize the resulting effect on critical mass. For the example in the preceding sections, a fuel injection tube with $r_i = 0.04$ in. (0.1 cm) and with a sleeve thickness of 0.5 in. would result in an increase in critical mass of about 5.5%.

TABLE I

CONSTANTS EMPLOYED TO CALCULATE COMPRESSIBILITY OF HYDROGEN

See Text, Eqs. (4), (5), and (6)

Constant	Units	Values Employed in Ref. 3	Values Employed in Present Report
b_1	$(cc/g.mole) \cdot (^oK)^{1/4}$	.0055478	.005390
b_2	$(cc/g.mole) \cdot (^oK)^{3/4}$	-.036877	-.043045
b_3	$(cc/g.mole) \cdot (^oK)^{5/4}$	-.22004	-.10393
c_1	$(cc/g.mole) \cdot (^oK)^{3/2}$	.004788	.009686
c_2	$(cc/g.mole) \cdot (^oK)^{2}$	-.04053	-.16816

TABLE II

TABULATION OF DATA FROM NASA LEWIS COAXIAL-FLOW EXPERIMENT

See Appendix II — Data From Ref. 11

Run	Flow Rate, lb/sec: Air, W_A	Flow Rate, lb/sec: Bromine, W_B	Initial Velocities, ft/sec: Air, V_A	Initial Velocities, ft/sec: Bromine, V_B	Air Density, ρ_A lb/ft^3	Reynolds Numbers: Re_B	Reynolds Numbers: Re_A	Reynolds Numbers: Re_Z(1)	$L/r_6 = 4$: $\bar{C}^*$	$L/r_6 = 4$: $\bar{\rho}_B/\rho_A$(1)	$L/r_6 = 4$: τ_B(1)	$L/r_6 = 8$: $\bar{C}^*$	$L/r_6 = 8$: $\bar{\rho}_B/\rho_A$(1)	$L/r_6 = 8$: τ_B(1)	$L/r_6 = 16$: $\bar{C}^*$	$L/r_6 = 16$: $\bar{\rho}_B/\rho_A$(1)	$L/r_6 = 16$: τ_B(1)
1	.0074	.000288	1.81	2.18	.0236	1030	1350	85	.898	2.80	.0263	.822	2.57	.0482	.695	2.17	.0816
2	.0073	.000250	1.79	1.85	.0235	870	1330	84	.837	2.68	.0291	.724	2.32	.0503	.595	1.91	.0827
3	.00945	.000244	2.8	2.24	.0194	870	1720	108	.895	2.80	.0311	.782	2.45	.0543	.652	2.04	.0907
4	.0095	.000187	2.81	1.71	.0195	670	1730	109	.776	2.44	.0352	.650	2.04	.0589	.525	1.65	.0951
5	.0095	.0000716	2.54	.59	.0215	255	1730	109	.800	2.53	.0953	.677	2.14	.161	.549	1.74	.2615
6	.0313	.000336	7.97	2.83	.0226	1200	5680	358	.710	2.08	.0168	.543	1.59	.0257	.384	1.13	.0363
7	.0475	.00108	13.1	9.25	.0209	3850	8680	547	.891	2.78	.0070	.808	2.52	.0126	.698	2.18	.0218
8	.0475	.000892	13.1	7.62	.0209	3190	8680	547	.895	2.79	.0085	.801	2.50	.0152	.658	2.05	.0249
9	.0475	.000731	13.1	6.24	.0209	2610	8680	547	.829	2.61	.0096	.731	2.30	.017	.591	1.86	.0274
10	.0475	.000529	13.1	4.52	.0209	1920	8680	547	.805	2.51	.0129	.660	2.06	.0211	.502	1.57	.0321
11	.091	.000852	24.7	7.16	.0212	3060	16,600	1046	.705	2.21	.0072	.551	1.72	.0109	.391	1.22	.0155
12	.091	.000666	24.7	5.6	.0212	2370	16,600	1046	.628	1.97	.0080	.485	1.52	.0123	.345	1.08	.0175
13	.091	.000370	24.7	3.11	.0212	1310	16,600	1046	.565	1.77	.0129	.413	1.29	.0189	.281	.88	.0258
14	.091	.000245	24.7	2.06	.0212	870	16,600	1046	.448	1.40	.0155	.319	1.00	.0221	.205	.64	.0284
15	.15	.000824	40.8	6.94	.0212	2930	27,400	1726	.585	1.83	.0060	.40	1.25	.0082	.271	.85	.0111
16	.152	.000532	41.3	4.48	.0212	1900	27,700	1745	.442	1.38	.0071	.30	.94	.0096	.194	.61	.0123
17	.147	.000245	40.0	2.06	.0212	875	27,000	1701	.326	1.02	.0112	.209	.65	.0144	.131	.41	.0181
18	.247	.000882	72.7	8.04	.0196	3150	45,100	2841	.48	1.50	.0043	.29	.91	.0056	.225	.70	.0086
19	.267	.000726	75.6	6.36	.0204	2590	48,400	3049	.375	1.18	.0043	.252	.79	.0059	.171	.54	.008
20	.267	.000487	75.6	4.27	.0204	1730	48,400	3049	.345	1.08	.006	.211	.66	.0073	.13	.41	.009
21	.272	.000179	77.1	1.57	.0203	640	49,300	3106	.318	1.00	.0151	.18	.56	.0170	.096	.30	.0182

(1) for $r_6/r_1 = 0.75$

TABLE III

RELATIVE VALUES OF AVERAGE NEUTRON FLUX IN EACH ENERGY GROUP
AND IN DIFFERENT PORTIONS OF MODERATOR

See Appendix III

	Boundaries of Energy Group, ev		Relative Average Neutron Flux, Neutrons/cm^2-sec			
Energy Group Number	Lower End	Upper end	Cavity	Beryllium oxide portion of moderator	Graphite portion of moderator	Heavy Water portion of moderator
18	1.35×10^6	10^7	1.93	.84	.13	.004
17	1.17×10^4	1.35×10^6	4.58	2.21	.39	.020
16	583	1.17×10^4	2.16	1.45	.33	.020
15	29	583	1.81	1.36	.39	.027
14	8.32	29	.93	.60	.18	.013
13	3.06	8.32	3.04	.82	.17	.011
12	2.38	3.06	1.17	.27	.06	.003
11	1.86	2.38	1.26	.33	.10	.003
10	1.44	1.86	1.36	.48	.17	.005
9	1.125	1.44	1.38	.68	.46	.005
8	.683	1.125	3.03	2.73	2.12	.032
7	.414	.683	3.26	4.66	3.36	.068
6	.3	.414	1.70	3.10	2.15	.067
5	.2	.3	1.46	3.13	2.20	.159
4	.1	.2	1.11	2.30	2.29	.916
3	.05	.1	.29	1.05	1.07	1.900
2	.015	.05	.067	.38	.56	2.231
1	0	.015	.0035	.04	.08	.479

TABLE IV

NEUTRON ABSORPTION CROSS SECTIONS FOR HAFNIUM AND FISSION CROSS SECTIONS FOR URANIUM-233 FOR DIFFERENT NEUTRON ENERGY GROUPS

See Appendix III
Hafnium Atom Density = 4.0×10^{22} atom/cm^3
U-233 Atom Density = 4.65×10^{22} atom/cm^3

Energy Group Number	Boundaries of Energy Group, ev		Neutron Absorption Cross Section for Hafnium, Σ_a = cm^{-1}	Fission Cross Section for U-233, Σ_f, cm^{-1}
	Lower End	Upper end		
18	1.35×10^6	10^7	0.08	0.09
17	1.17×10^4	1.35×10^6	0.08	0.13
16	583	1.17×10^4	0.40	0.38
15	29	583	0.60	1.25
14	8.32	29	1.40	4.46
13	3.06	8.32	8.00	4.97
12	2.38	3.06	8.00	2.85
11	1.86	2.38	40.00	17.20
10	1.44	1.86	4.00	27.90
9	1.125	1.44	24.00	10.80
8	.683	1.125	8.00	6.19
7	.414	.683	2.20	6.21
6	.3	.414	1.80	7.17
5	.2	.3	1.80	8.25
4	.1	.2	2.00	5.40
3	.05	.1	2.60	14.70
2	.015	.05	4.00	22.40
1	0	.015	8.00	44.40

TABLE V

EFFECT OF THICKNESS OF SLEEVE SURROUNDING
FUEL-INJECTION DUCT ON CRITICAL MASS

See Appendix III
Cavity Diameter - 9 ft
Spherical Cavity Surface Area = 254.0 ft^2 = 2.36 x 10^5 cm^2
Moderator Thickness = 2 ft = 61.0 cm

Outside Radius of Sleeve Sur-rouding Fuel-Injection Duct, r_o-cm		Outside Surface Area of Sleeve Surrounding Fuel Injection Duct, cm^2	$\frac{\text{Outside Sleeve Surface Area}}{\text{Cavity Surface Area}}$	Fractional Increase in Critical Mass Due to Presence of Sleeve
in.	cm			
0.40	1.0	383	.00162	.04
0.80	2.0	766	.00324	.08
1.20	3.0	1150	.00487	.12
1.60	4.0	1532	.0065	.16

MOLLIER DIAGRAM FOR HYDROGEN AT HIGH PRESSURES

DATA CALCULATED USING PROCEDURES OF REF. 3

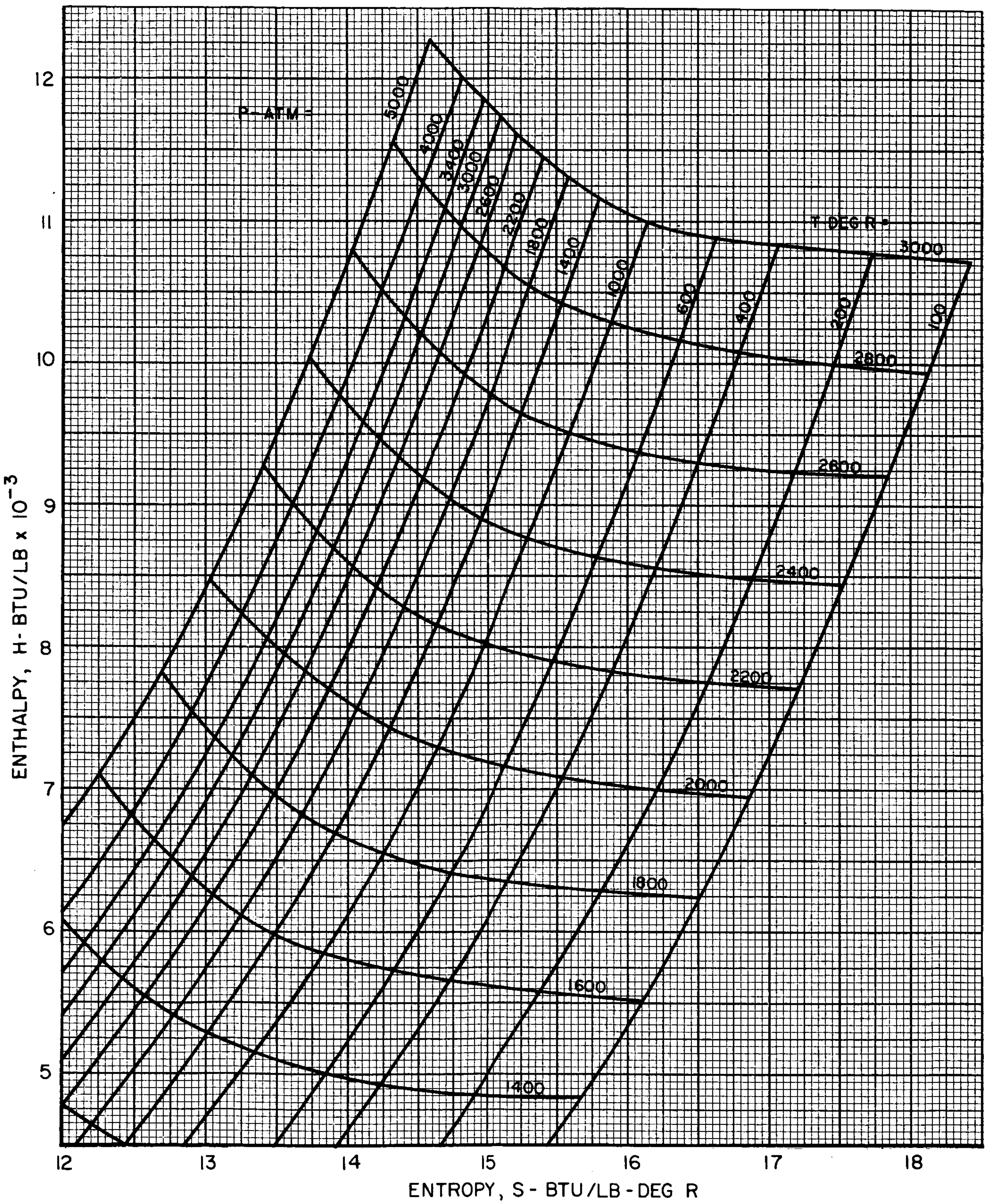

FIG. 2

HYDROGEN DENSITIES EMPLOYED IN ANALYSIS OF PUMP PERFORMANCE

CURVE A USED UNLESS OTHERWISE SPECIFIED

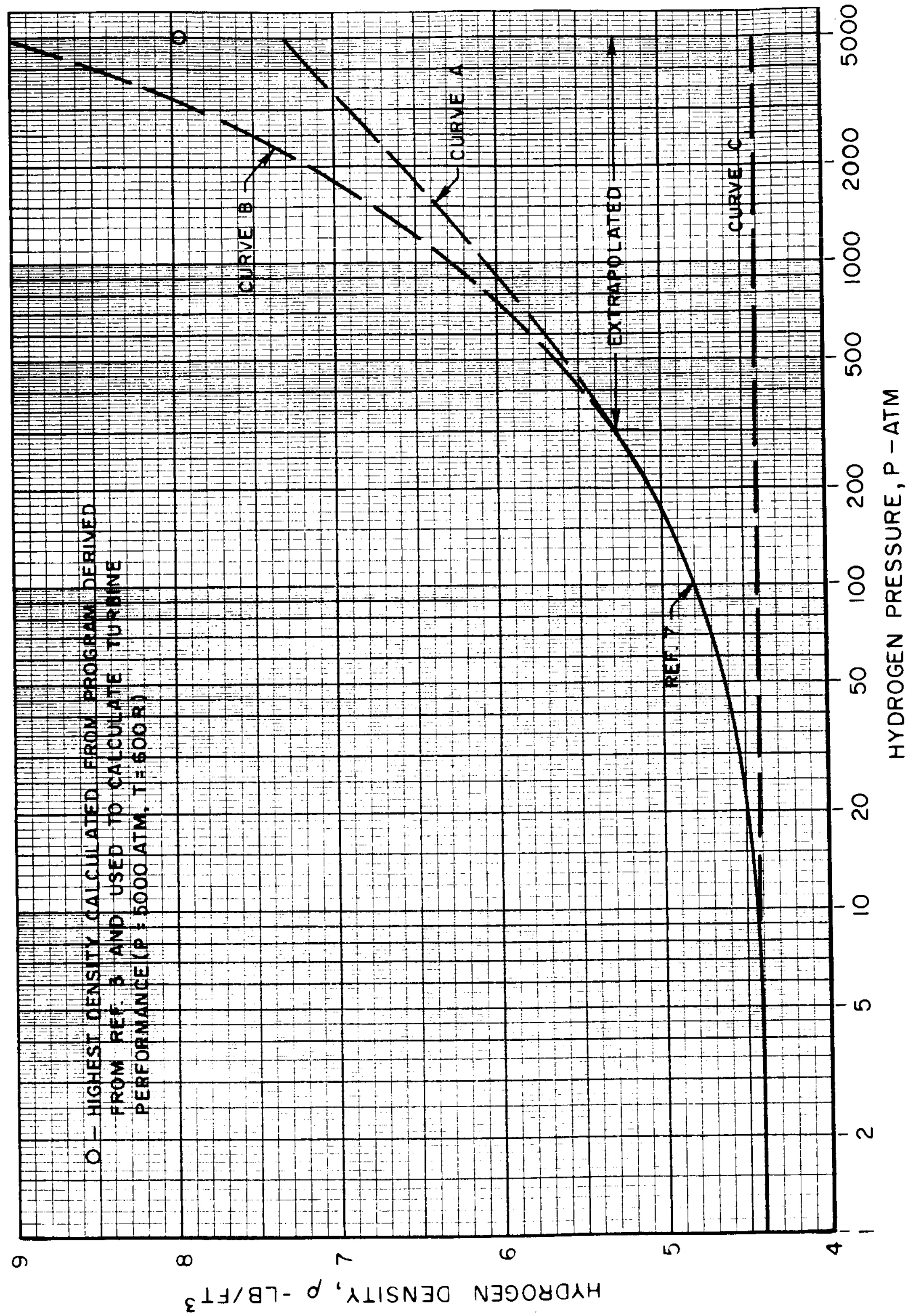

EFFECT OF PRESSURE ON ISENTROPIC ENTHALPY RISE IN HYDROGEN PUMP

PUMP INLET PRESSURE, P_1 = 1 ATM

PUMP INLET TEMPERATURE, T_1 = 36 R

CURVES CALCULATED USING DENSITIES FROM FIG. 2 AND FOLLOWING EQUATION:

$$(\Delta H_P)_i = \int v\,dP = \int dP/\rho$$

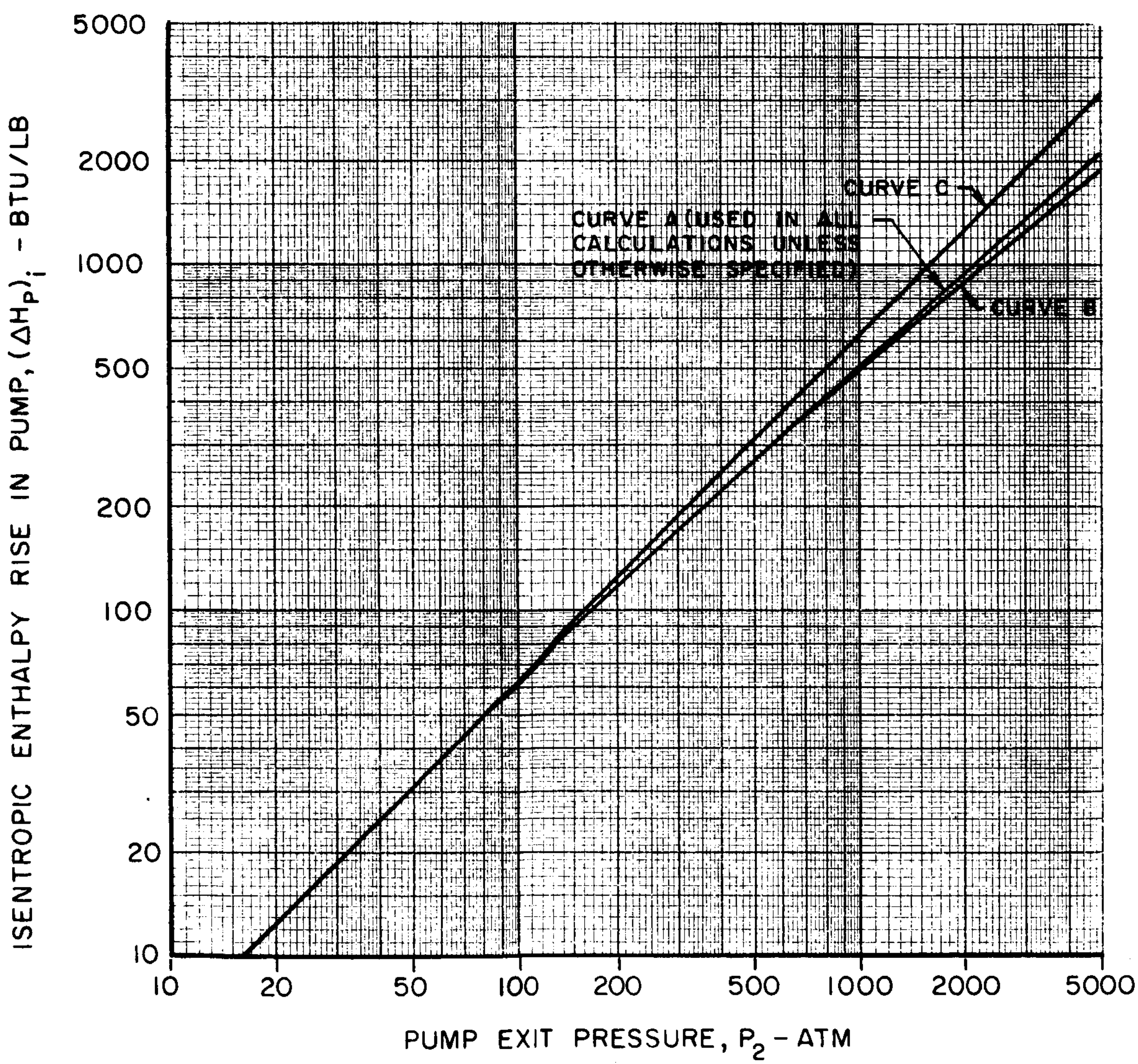

TURBOPUMP CYCLES EMPLOYED IN ANALYSIS

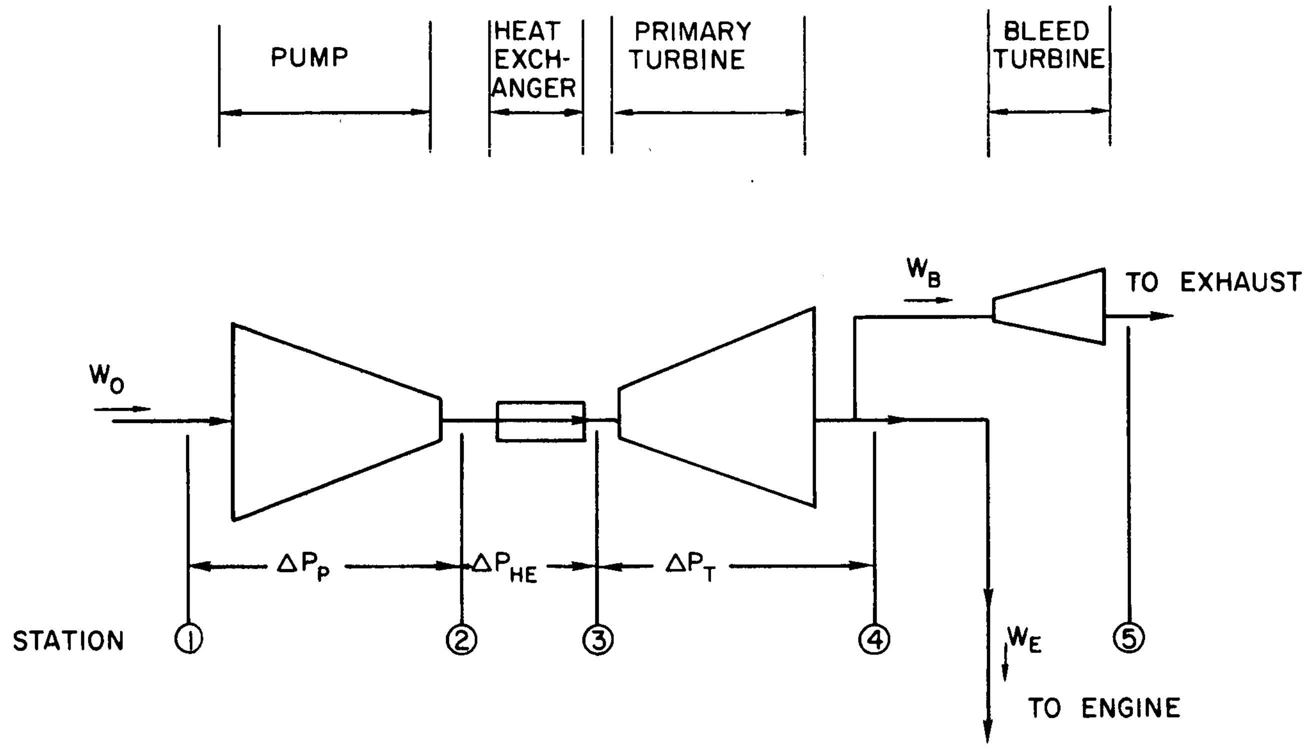

CYCLE	$F = \dfrac{(\text{WORK IN PRIMARY TURBINE})}{(\text{WORK IN PRIMARY PLUS BLEED TURBINE})}$	PRIMARY TURBINE PRESSURE DROP $\Delta P_T = P_3 - P_4$	(BLEED TURBINE FLOW)/(TOTAL FLOW), W_B/W_O	BLEED TURBINE EXPANSION PRESSURE RATIO, P_5/P_4
TOPPING	1.0	> 0	0	--
BLEED	0	0	> 0	0.01
MIXED	0.5	> 0	> 0	0.01

PRIMARY TURBINE PRESSURE DROP REQUIRED FOR TOPPING CYCLE AND TURBINE INLET TEMPERATURE OF 1400 R

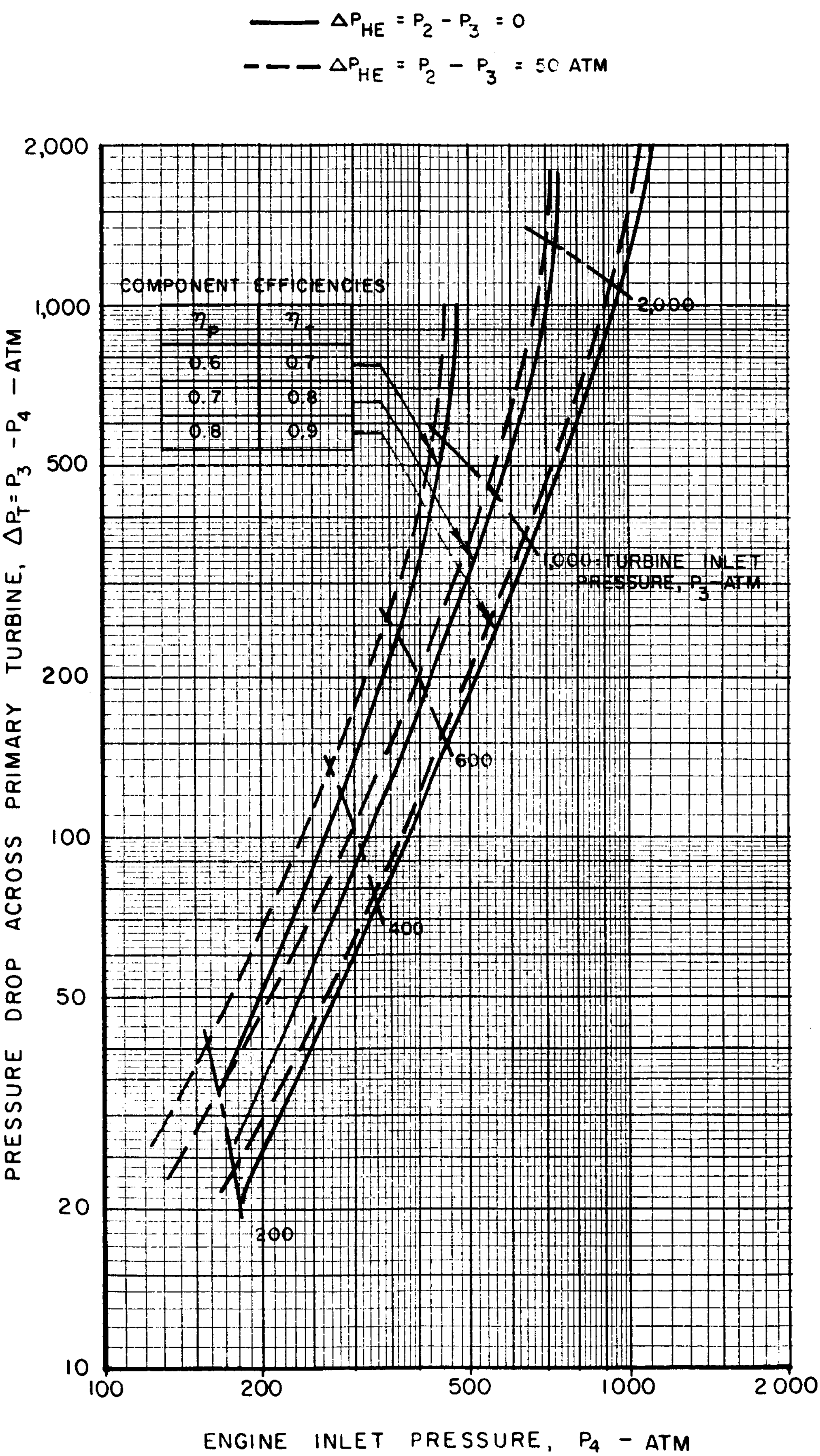

PRIMARY TURBINE PRESSURE DROP REQUIRED FOR TOPPING CYCLE AND TURBINE INLET TEMPERATURE OF 2200 R

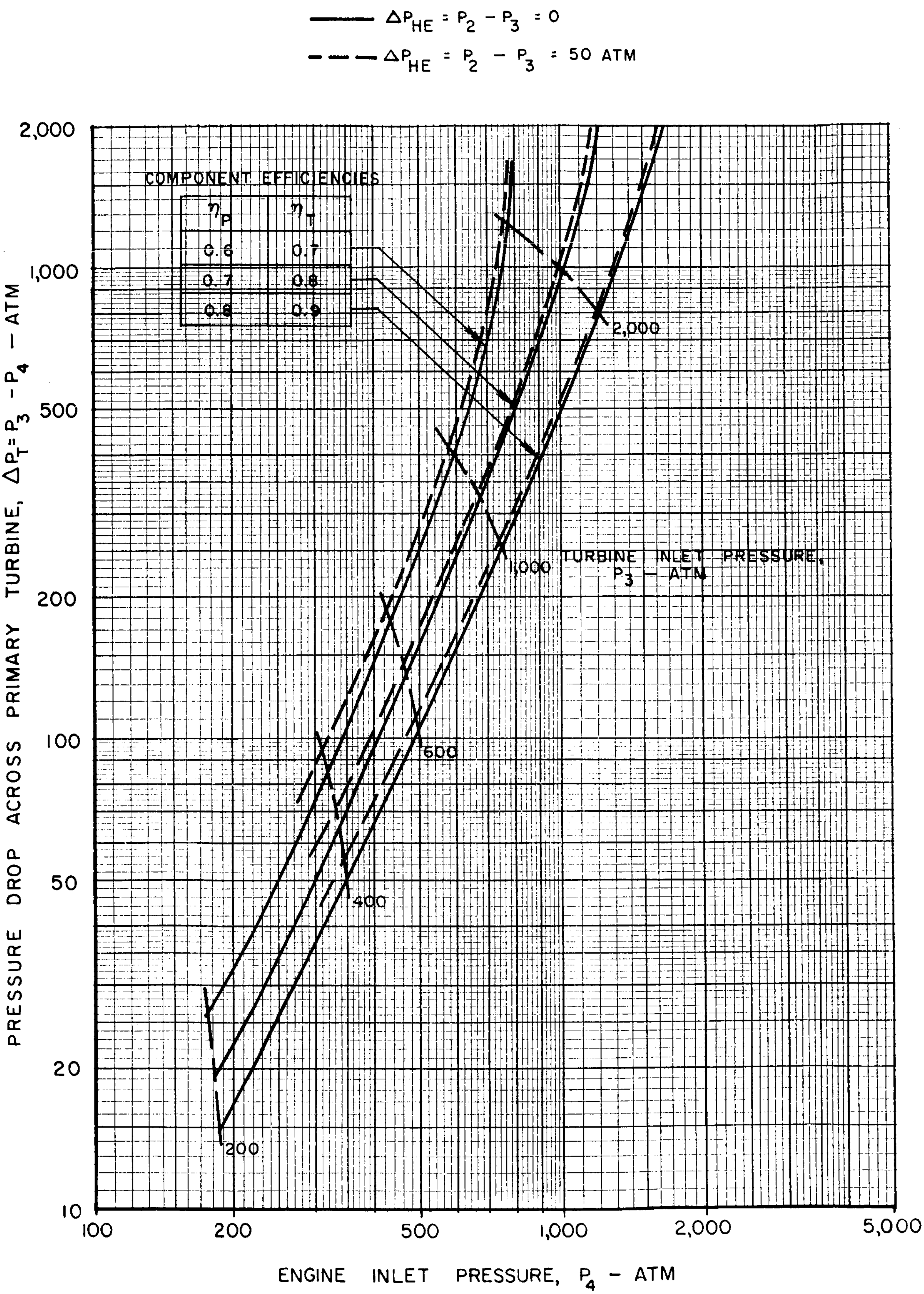

PRIMARY TURBINE PRESSURE DROP REQUIRED FOR TOPPING CYCLE AND TURBINE INLET TEMPERATURE OF 3000 R

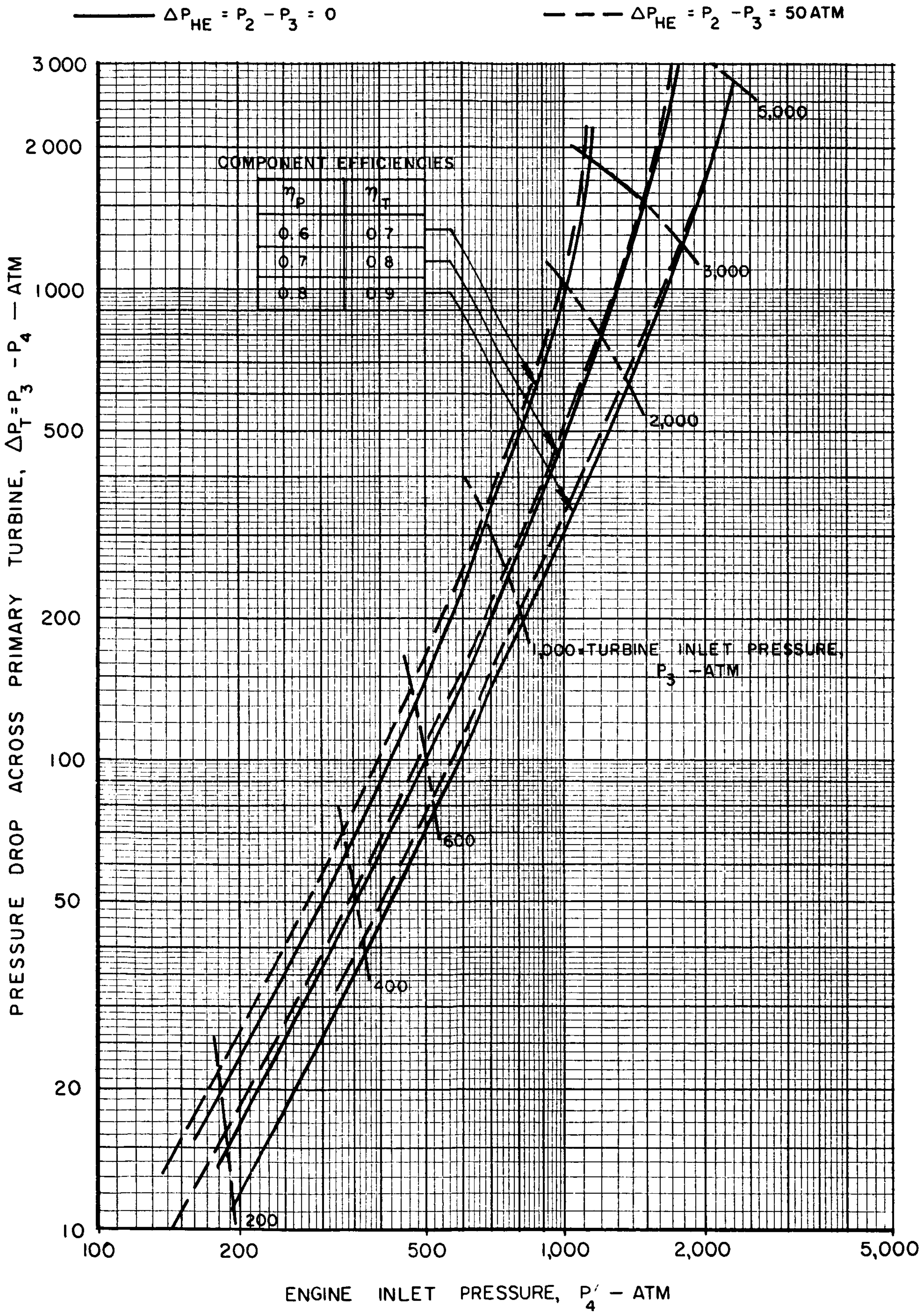

PRIMARY TURBINE PRESSURE DROP REQUIRED FOR TOPPING CYCLE AND TURBINE INLET TEMPERATURE OF 3800 R

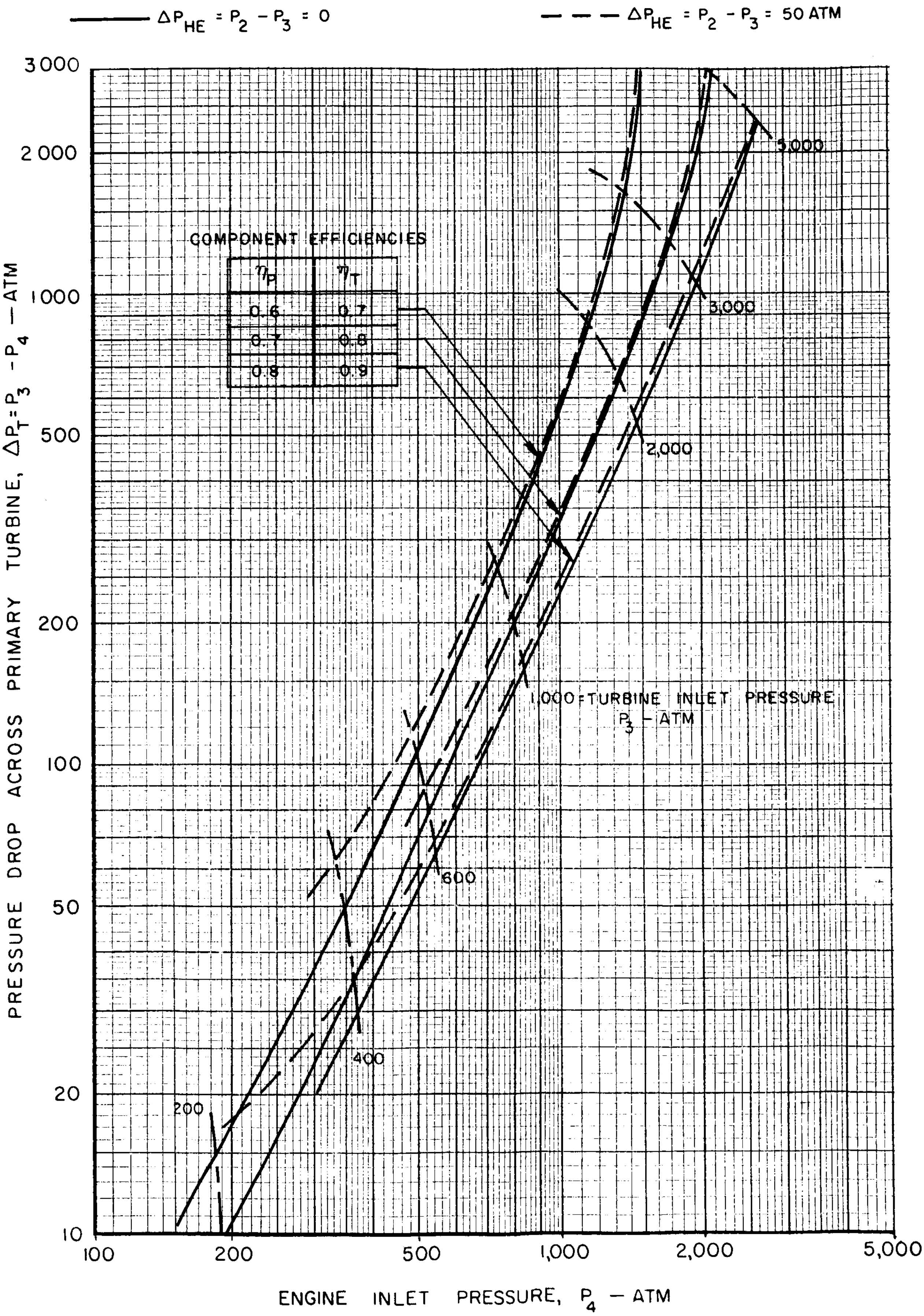

EFFECT OF TURBINE INLET TEMPERATURE ON MAXIMUM ENGINE INLET PRESSURES FOR TOPPING CYCLE

MAXIMUM VALUES OF ENGINE INLET PRESSURE DETERMINED FROM MAXIMUM ASSUMED VALUES OF PRIMARY TURBINE PRESSURE DROP NOTED ON EACH SET OF CURVES

——— $\Delta P_{HE} = P_2 - P_3 = 0$ — — — $\Delta P_{HE} = P_2 - P_3 = 50$ ATM

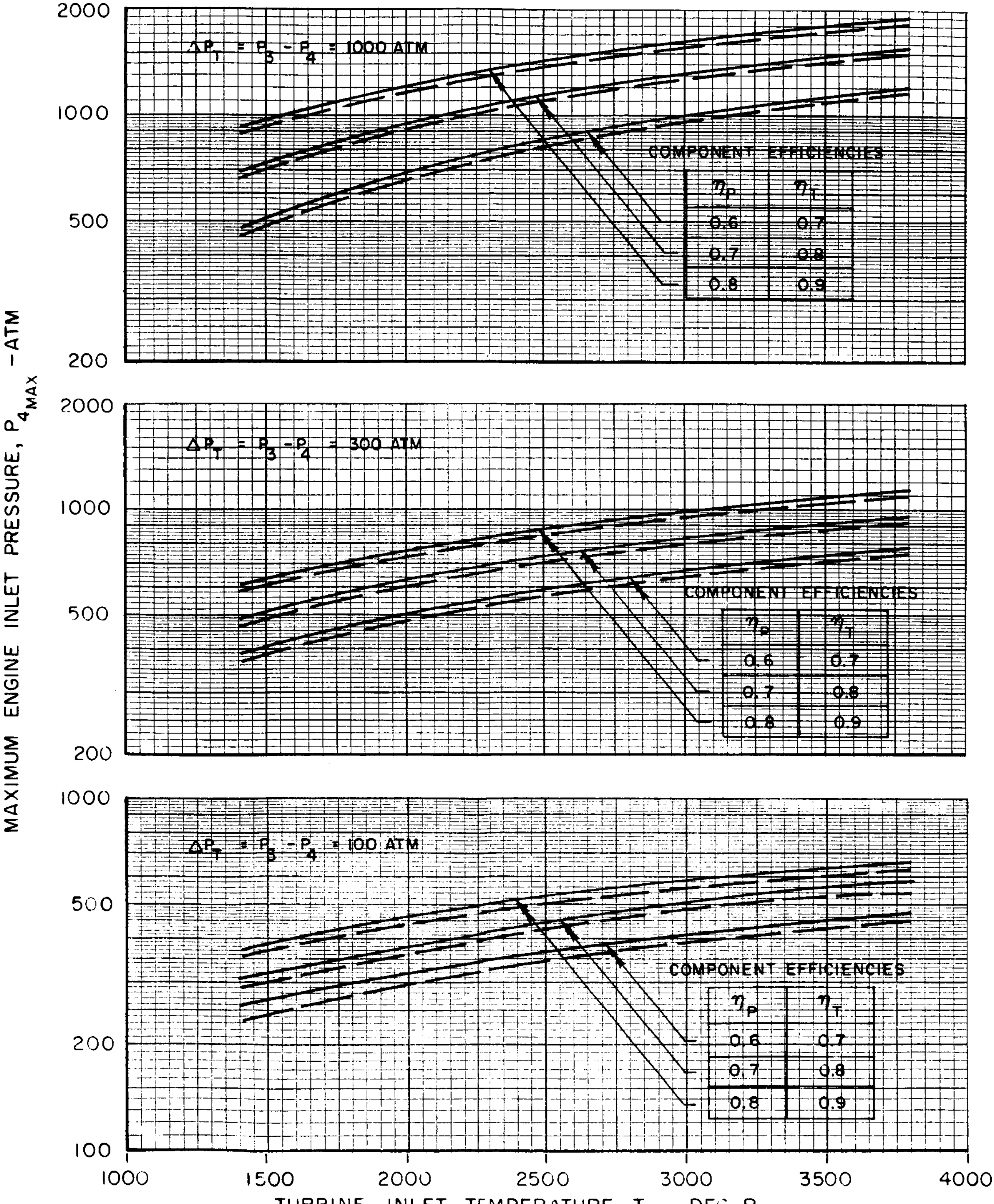

EFFECT OF HYDROGEN CHARACTERISTICS IN PUMP ON TURBINE PRESSURE DROP FOR TOPPING CYCLE

TURBINE INLET TEMPERATURE, T_3 = 2200 R
HEAT EXCHANGER PRESSURE DROP, $\Delta P_{HE} = P_2 - P_3 = 0$

LINE	PUMP ENTHALPY CURVE IN FIG. 3
solid line	A (USED TO CALCULATE FIGS. 5 TO 9)
long-dash line	B
dash-dot line	C

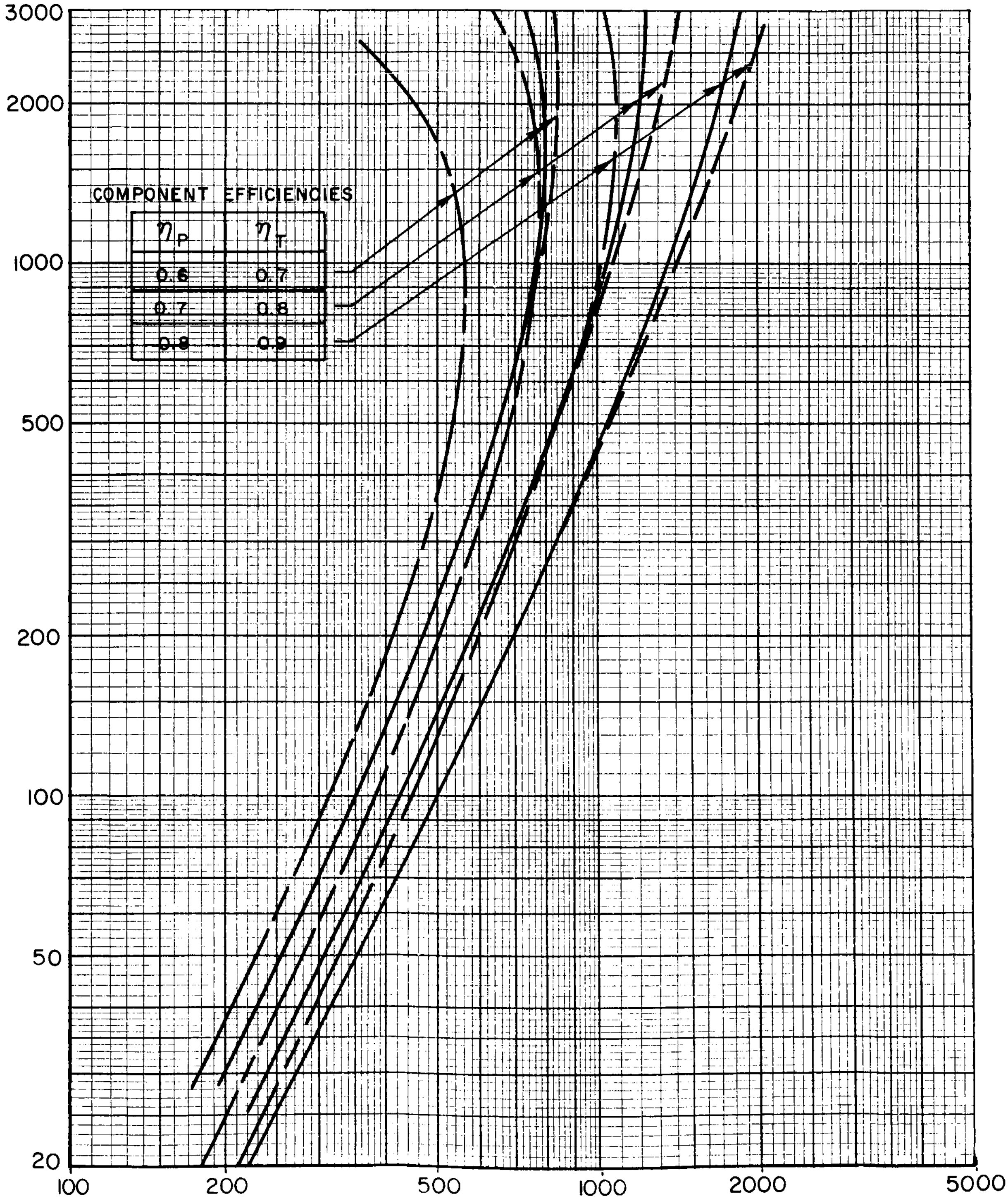

BLEED FLOW FRACTION REQUIRED FOR BLEED CYCLE AND TURBINE INLET TEMPERATURE OF 1400 R

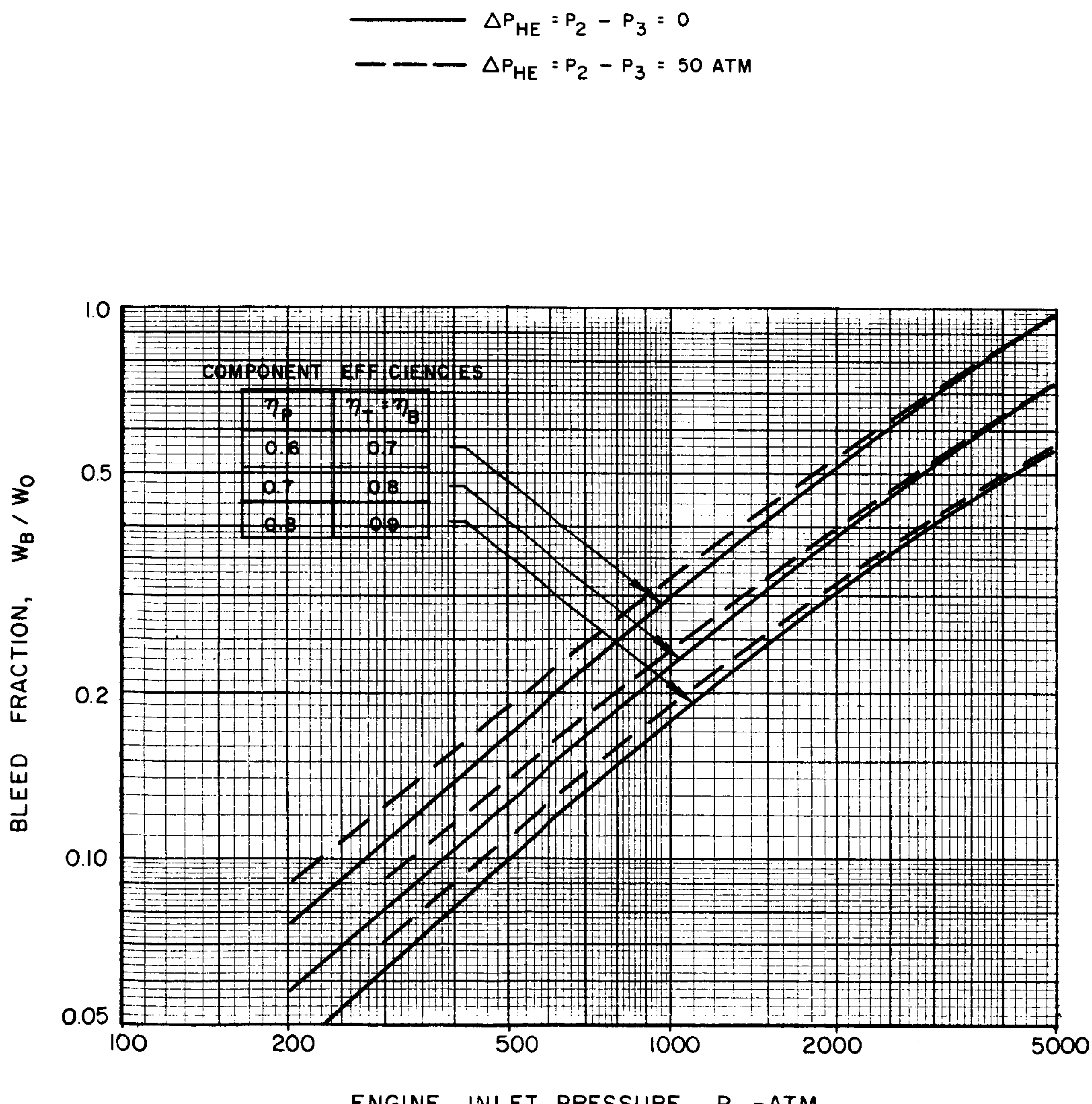

BLEED FLOW FRACTION REQUIRED FOR BLEED CYCLE AND TURBINE INLET TEMPERATURE OF 2200 R

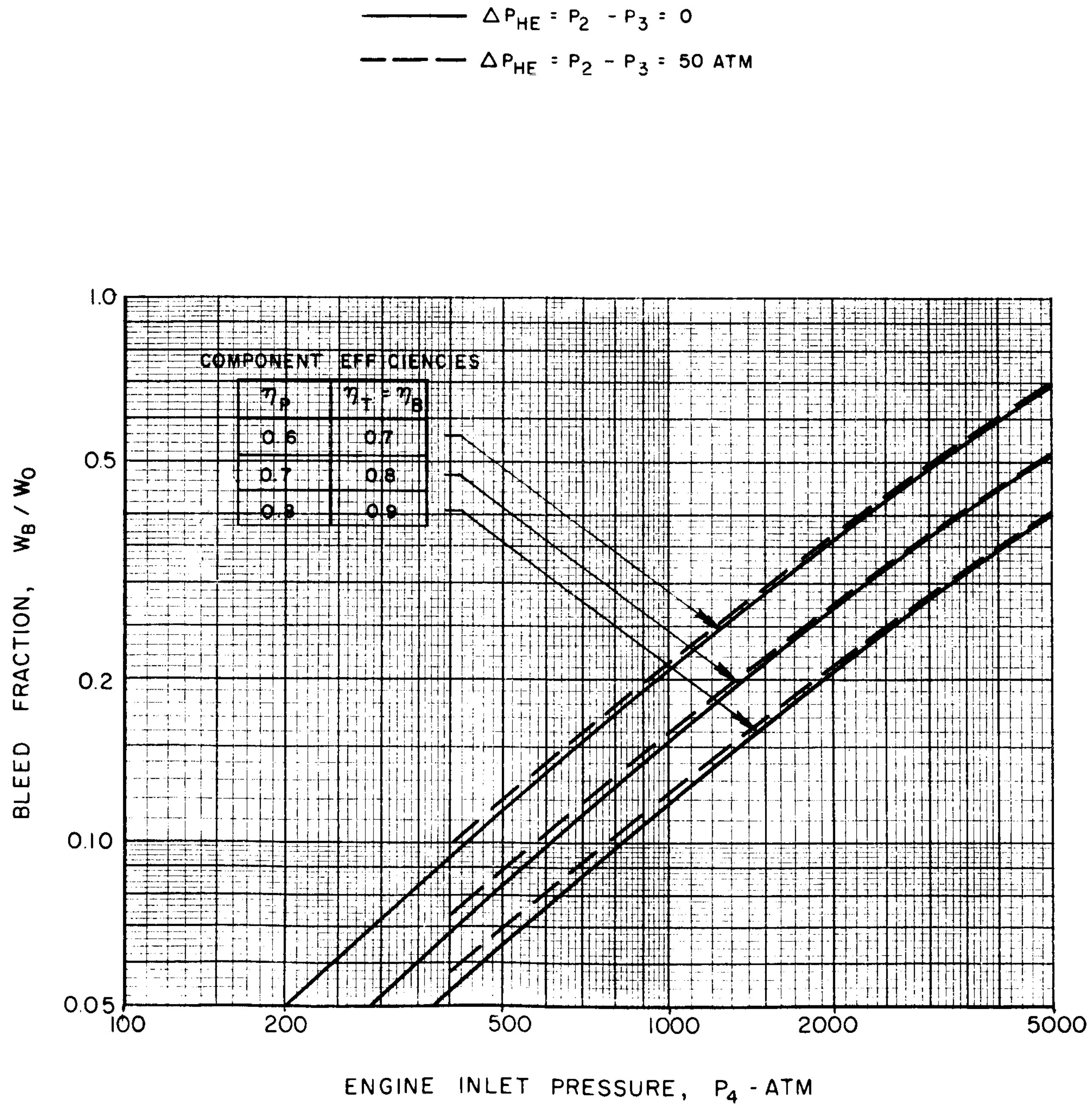

BLEED FLOW FRACTION REQUIRED FOR BLEED CYCLE AND TURBINE INLET TEMPERATURE OF 3000 R

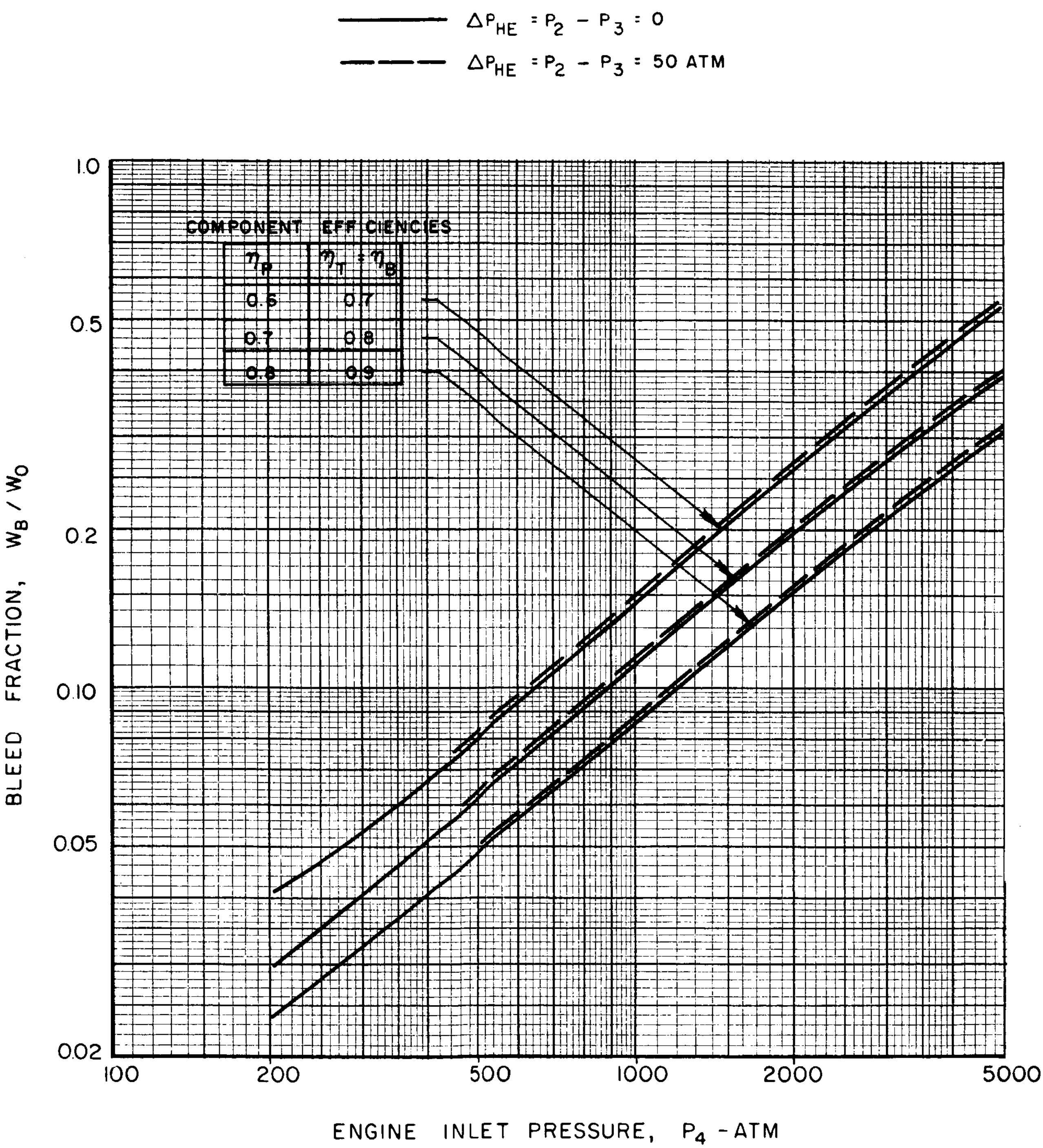

BLEED FLOW FRACTION REQUIRED FOR BLEED CYCLE AND TURBINE INLET TEMPERATURE OF 3800 R

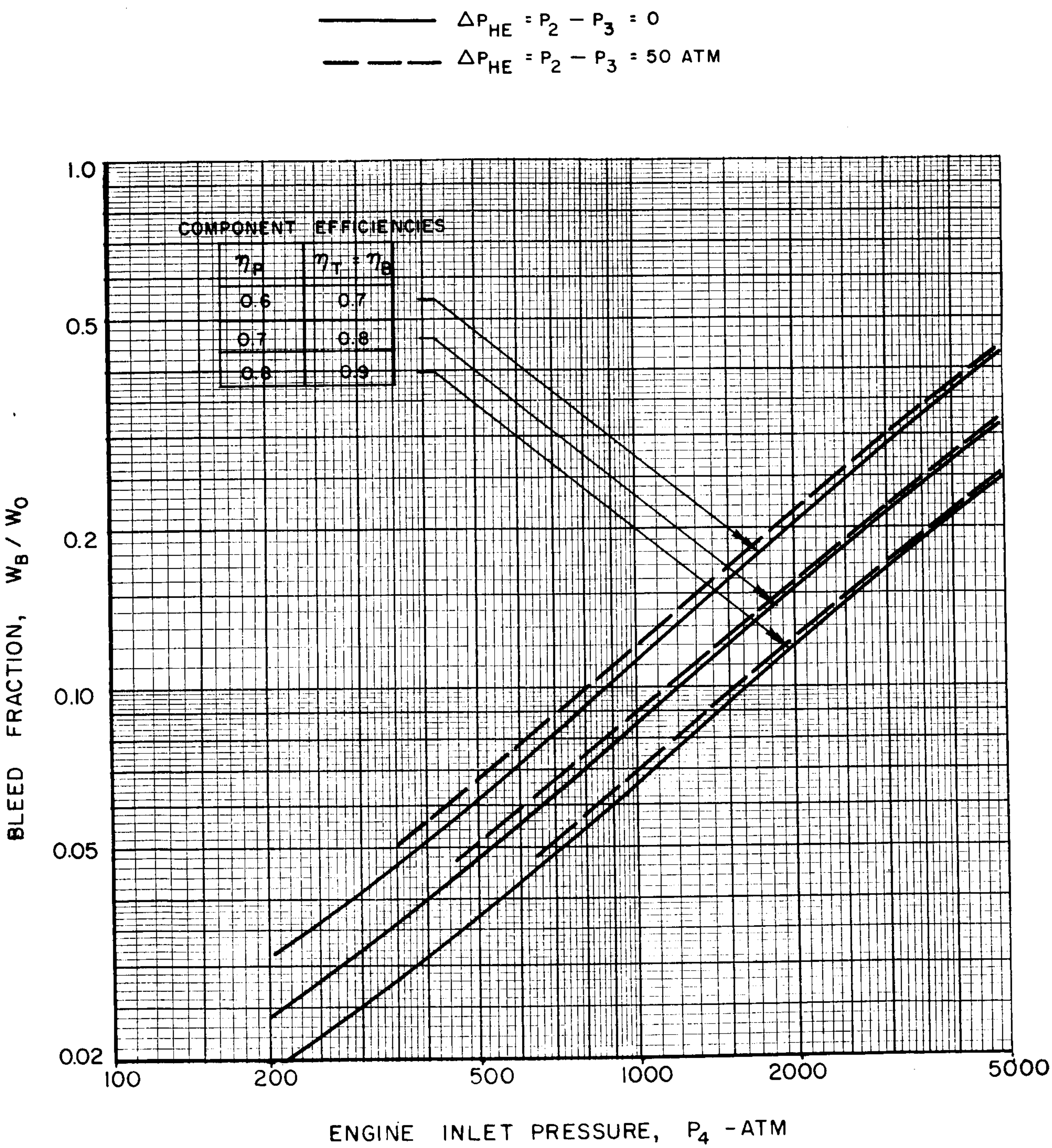

EFFECT OF TURBINE INLET TEMPERATURE ON MAXIMUM ENGINE INLET PRESSURES USING BLEED CYCLE

MAXIMUM ENGINE INLET PRESSURES DETERMINED FROM FIGS. 11 TO 14 FOR VALUES OF BLEED FRACTION NOTED ON EACH SET OF CURVES

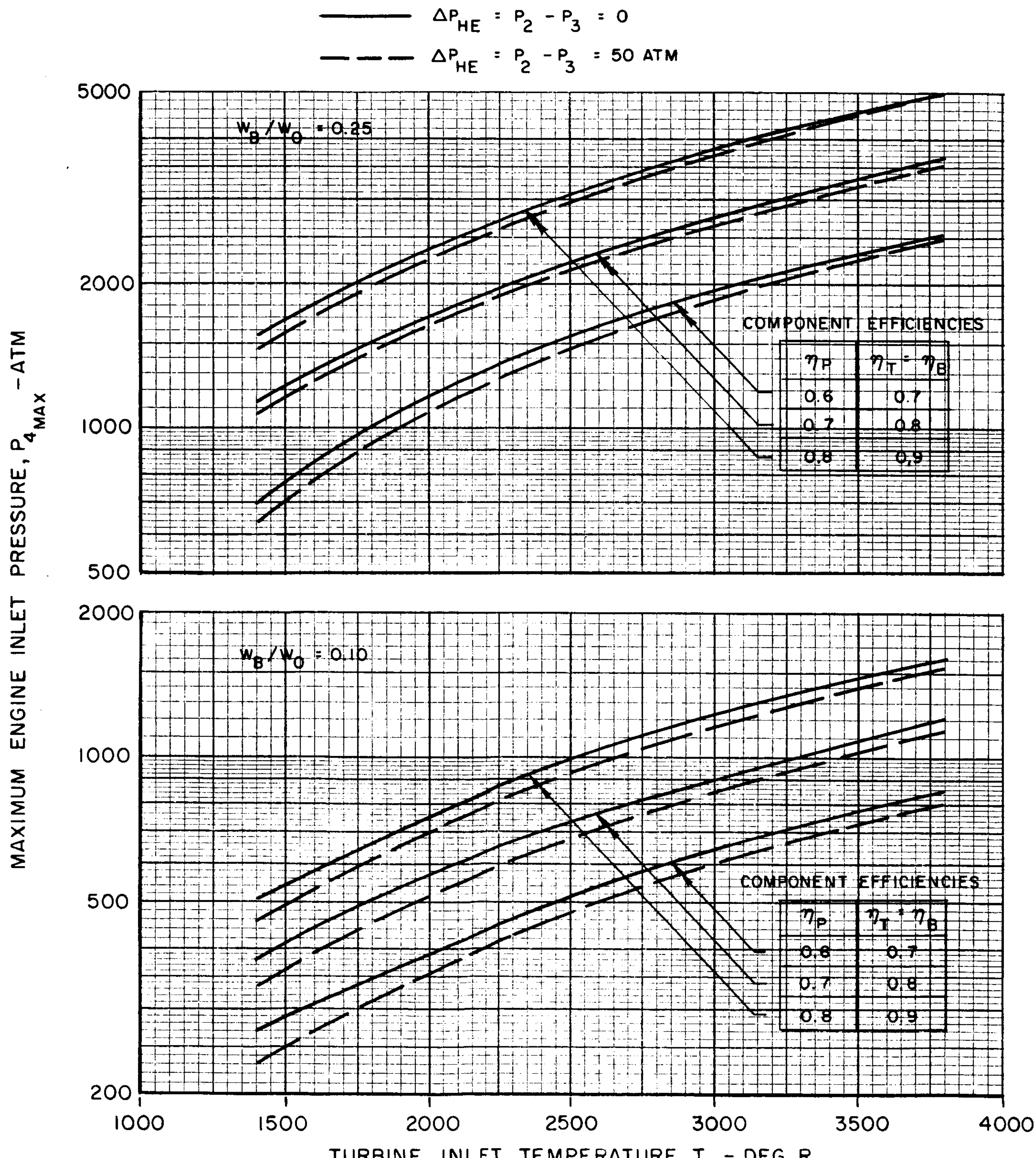

EFFECT OF HYDROGEN CHARACTERISTICS IN PUMP ON BLEED FLOW FRACTION FOR BLEED CYCLE

TURBINE INLET TEMPERATURE, T_3 = 2200 R
HEAT EXCHANGER PRESSURE DROP, $\Delta P_{HE} = P_2 - P_3 = 0$

LINE	PUMP ENTHALPY CURVE IN FIG. 3
———	A (USED TO CALCULATE FIGS 11 TO 15)
— — —	B
—·—	C

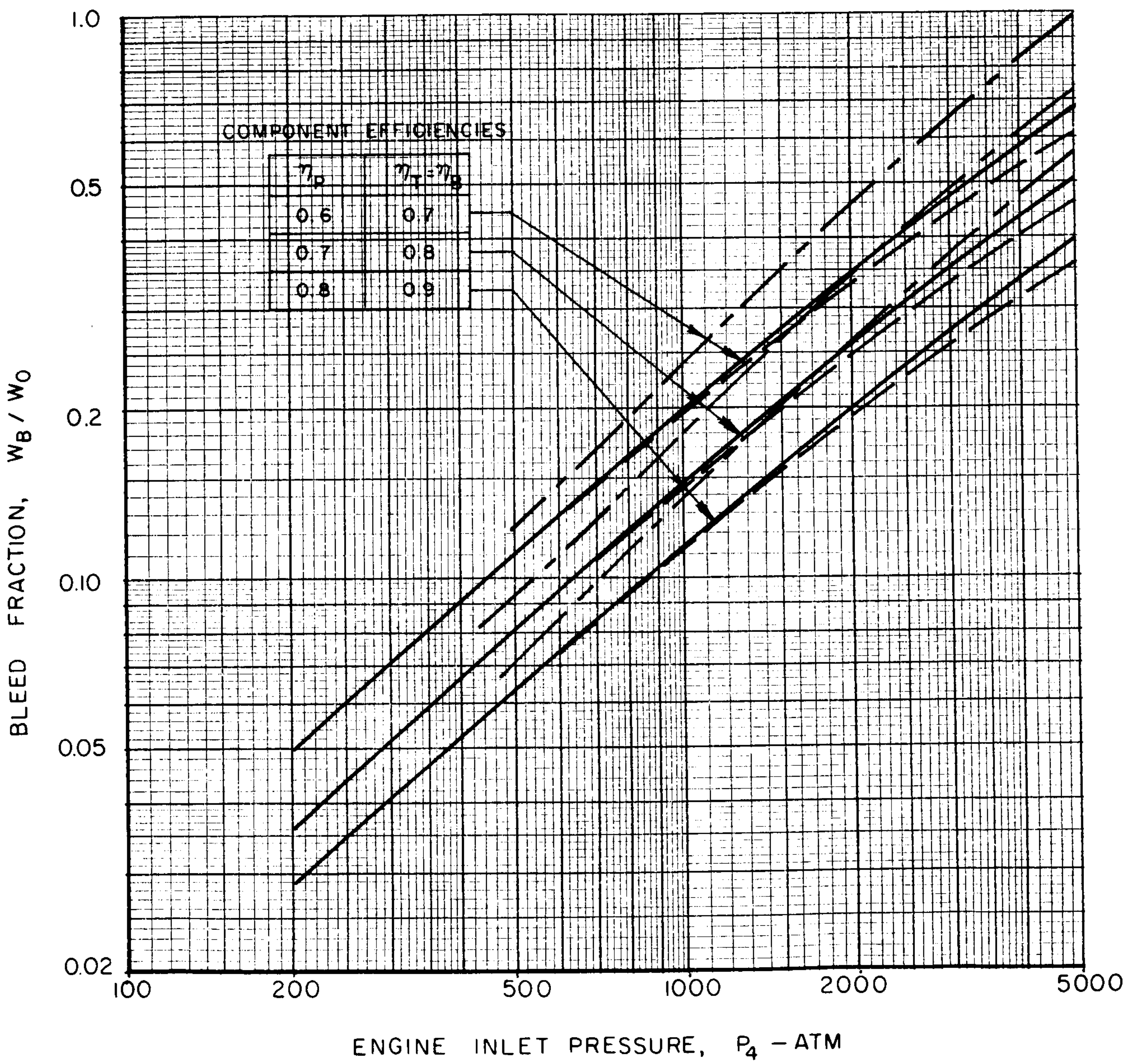

PRIMARY TURBINE PRESSURE DROP REQUIRED FOR MIXED CYCLE AND PRIMARY TURBINE INLET TEMPERATURE OF 1400 R

CORRESPONDING VALUE OF BLEED FLOW FRACTION GIVEN IN FIG. 18
FRACTION OF WORK IN PRIMARY TURBINE, F = 0.5

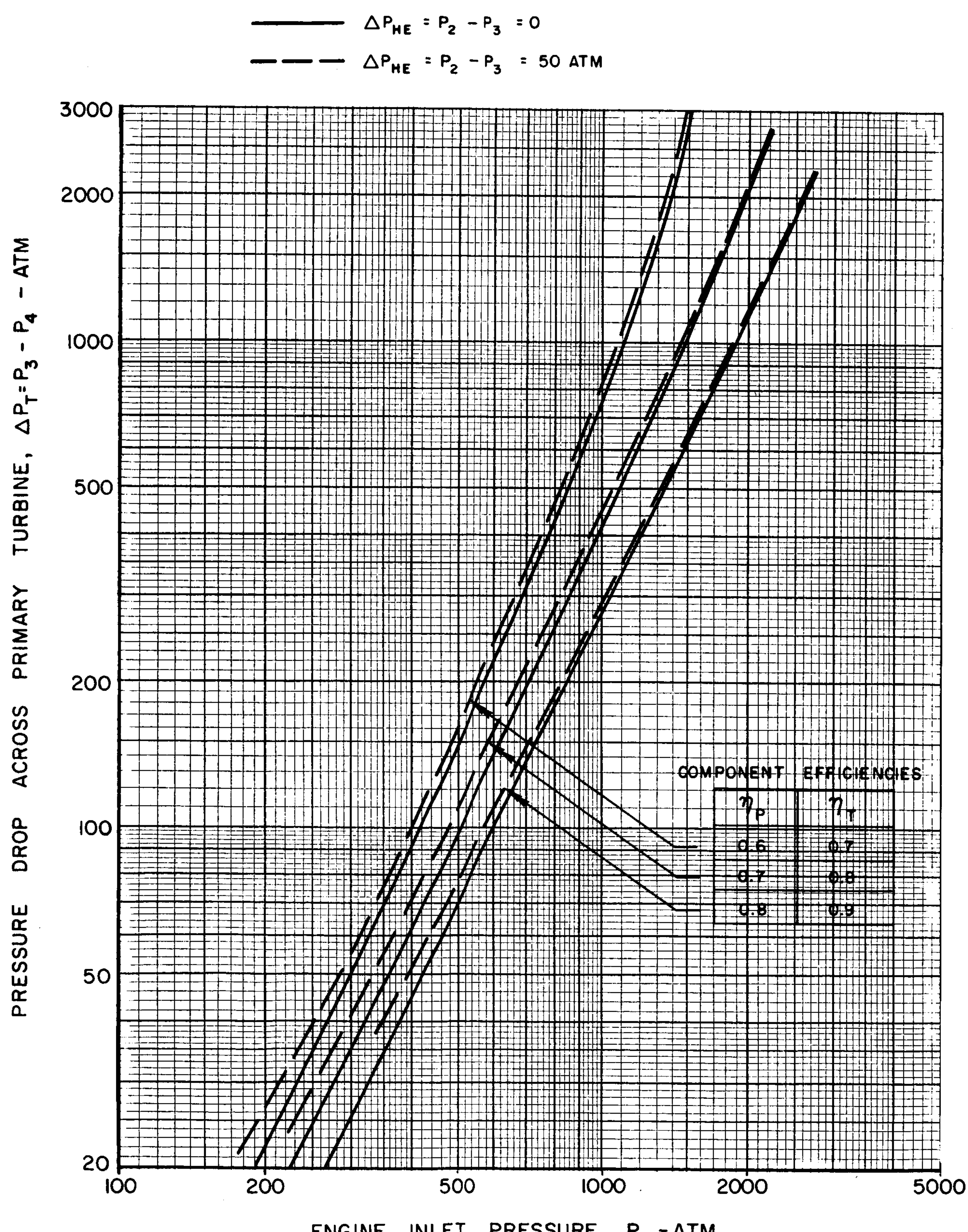

BLEED FLOW FRACTION REQUIRED FOR MIXED CYCLE AND PRIMARY TURBINE INLET TEMPERATURE OF 1400 R

CORRESPONDING VALUE OF PRIMARY TURBINE PRESSURE DROP GIVEN IN FIG. 17

FRACTION OF WORK IN PRIMARY TURBINE, F = 0.50

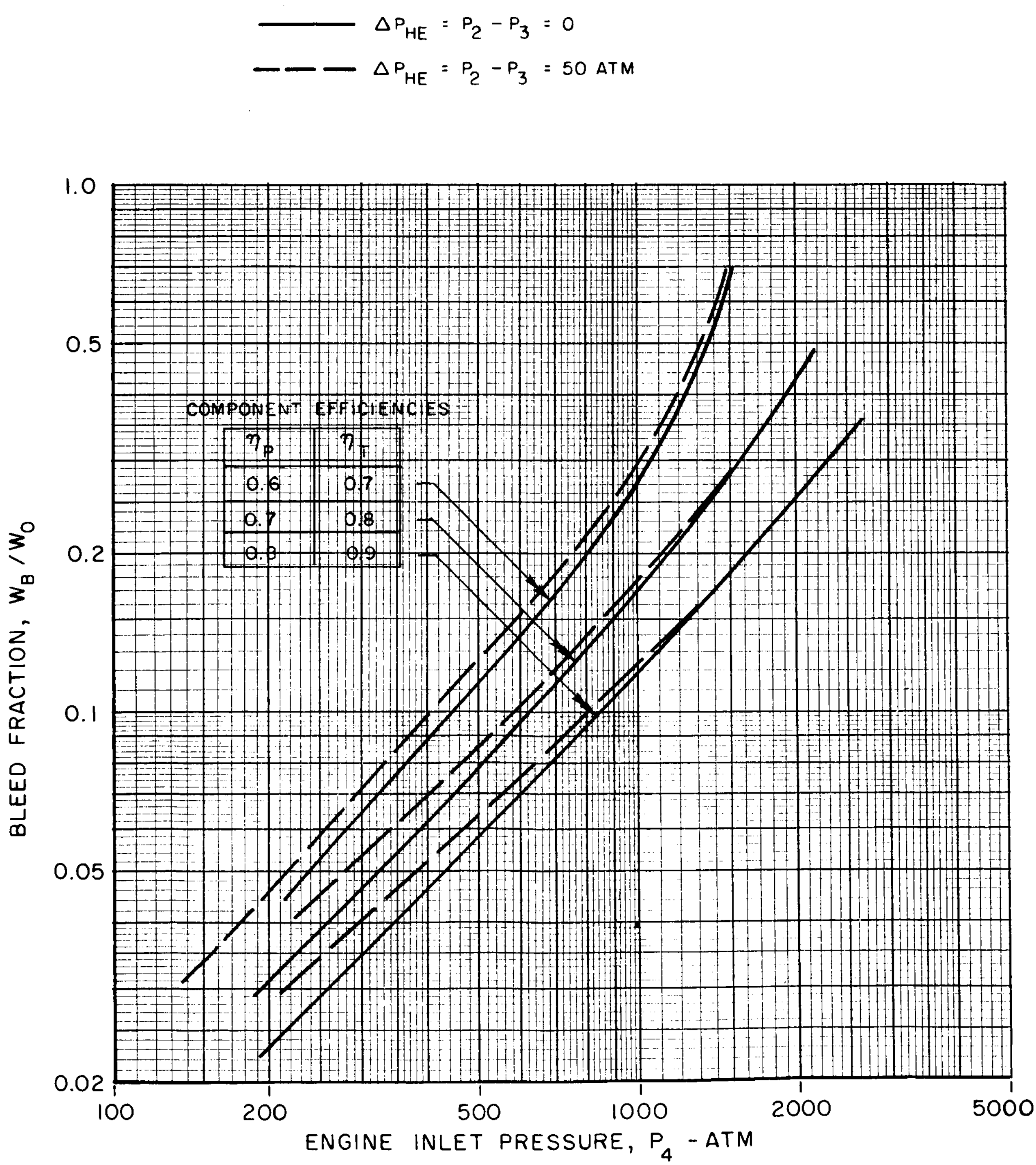

PRIMARY TURBINE PRESSURE DROP REQUIRED FOR MIXED CYCLE AND PRIMARY TURBINE INLET TEMPERATURE OF 2200 R

CORRESPONDING VALUE OF BLEED FLOW FRACTION GIVEN IN FIG. 20
FRACTION OF WORK IN PRIMARY TURBINE, F = 0.5

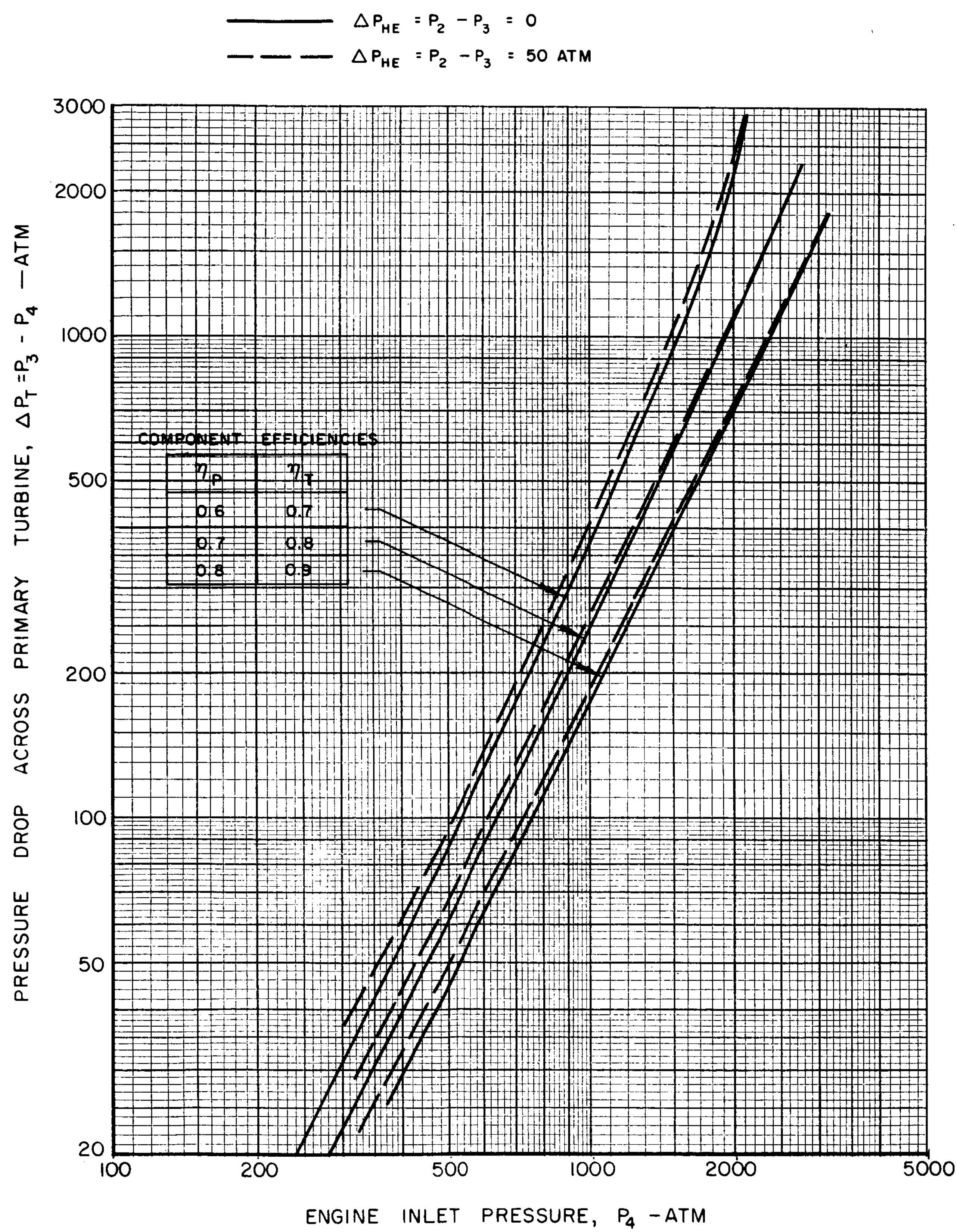

BLEED FLOW FRACTION REQUIRED FOR BLEED CYCLE AND PRIMARY TURBINE INLET TEMPERATURE OF 2200 R

CORRESPONDING VALUE OF PRIMARY TURBINE PRESSURE DROP GIVEN IN FIG. 19
FRACTION OF WORK IN PRIMARY TURBINE, F = 0.5

——————— $\Delta P_{HE} = P_2 - P_3 = 0$

— — — $\Delta P_{HE} = P_2 - P_3 = 50$ ATM

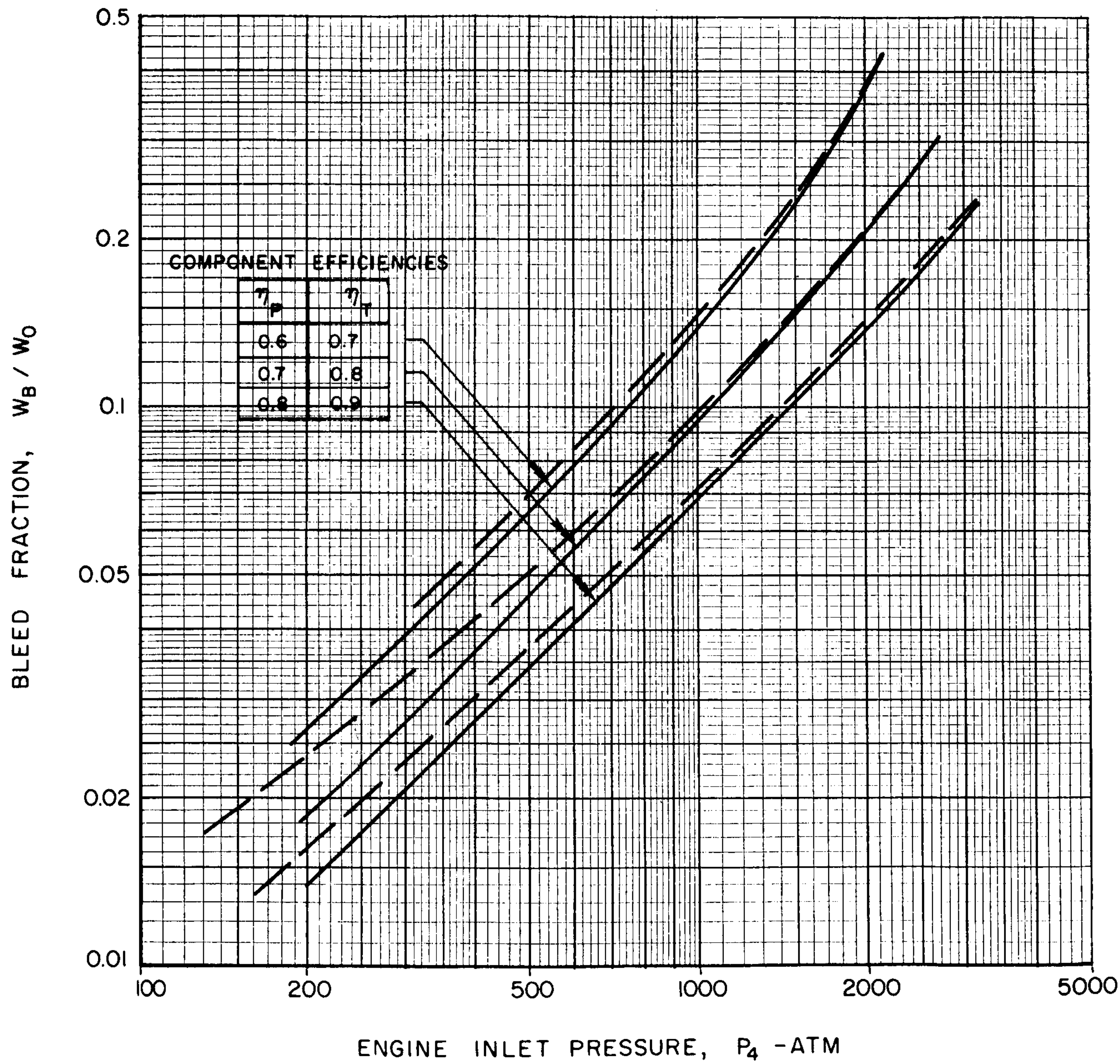

PRIMARY TURBINE PRESSURE DROP REQUIRED FOR MIXED CYCLE AND PRIMARY TURBINE INLET TEMPERATURE OF 3000 R

CORRESPONDING VALUE OF BLEED FLOW FRACTION GIVEN IN FIG. 22
FRACTION OF WORK IN PRIMARY TURBINE, F = 0.5

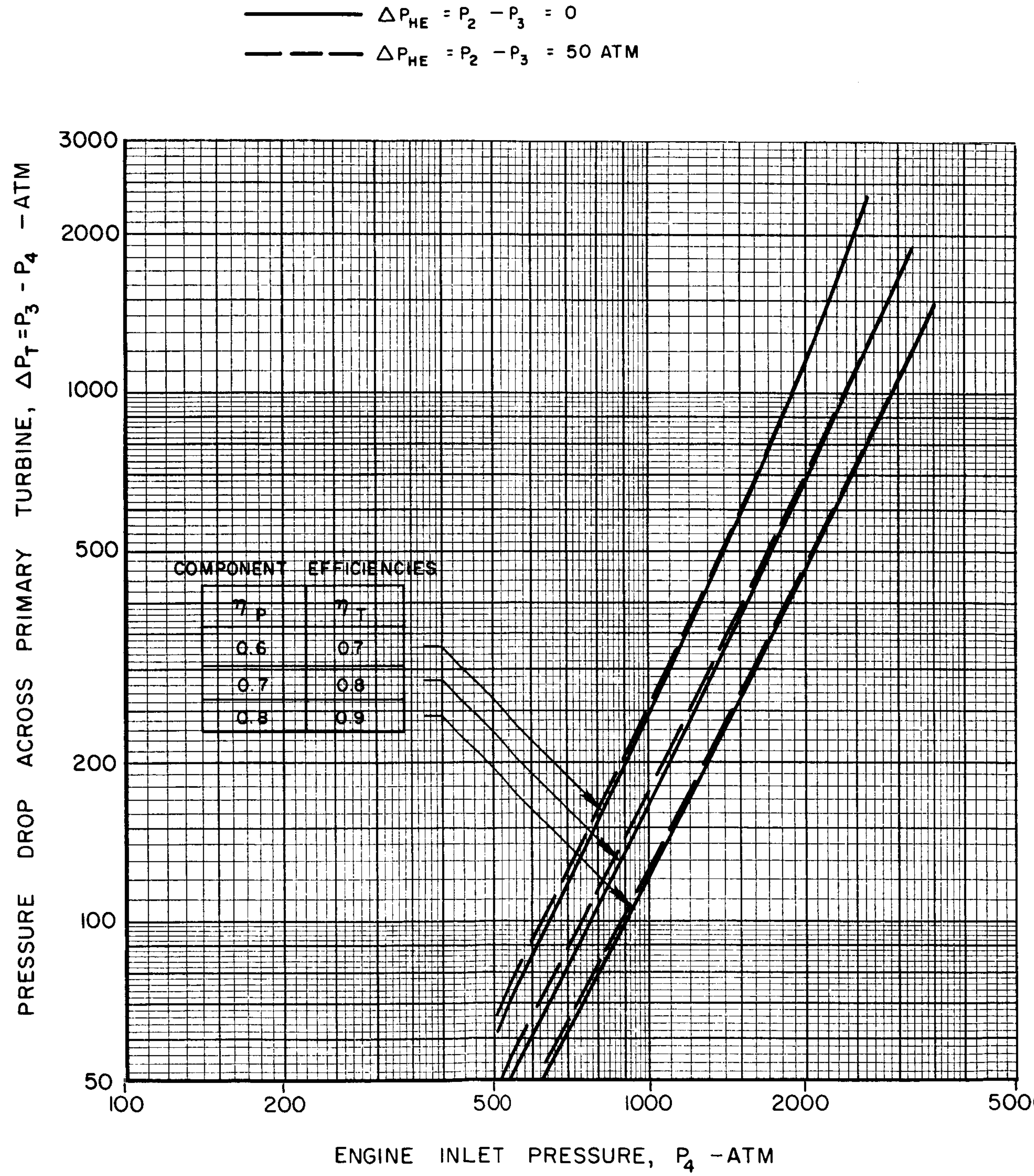

BLEED FLOW FRACTION REQUIRED FOR BLEED CYCLE AND PRIMARY TURBINE INLET TEMPERATURE OF 3000 R

CORRESPONDING VALUE OF PRIMARY TURBINE PRESSURE DROP GIVEN IN FIG. 21
FRACTION OF WORK IN PRIMARY TURBINE, F = 0.5

——————— $\Delta P_{HE} = P_2 - P_3 = 0$

— — — $\Delta P_{HE} = P_2 - P_3 = 50$ ATM

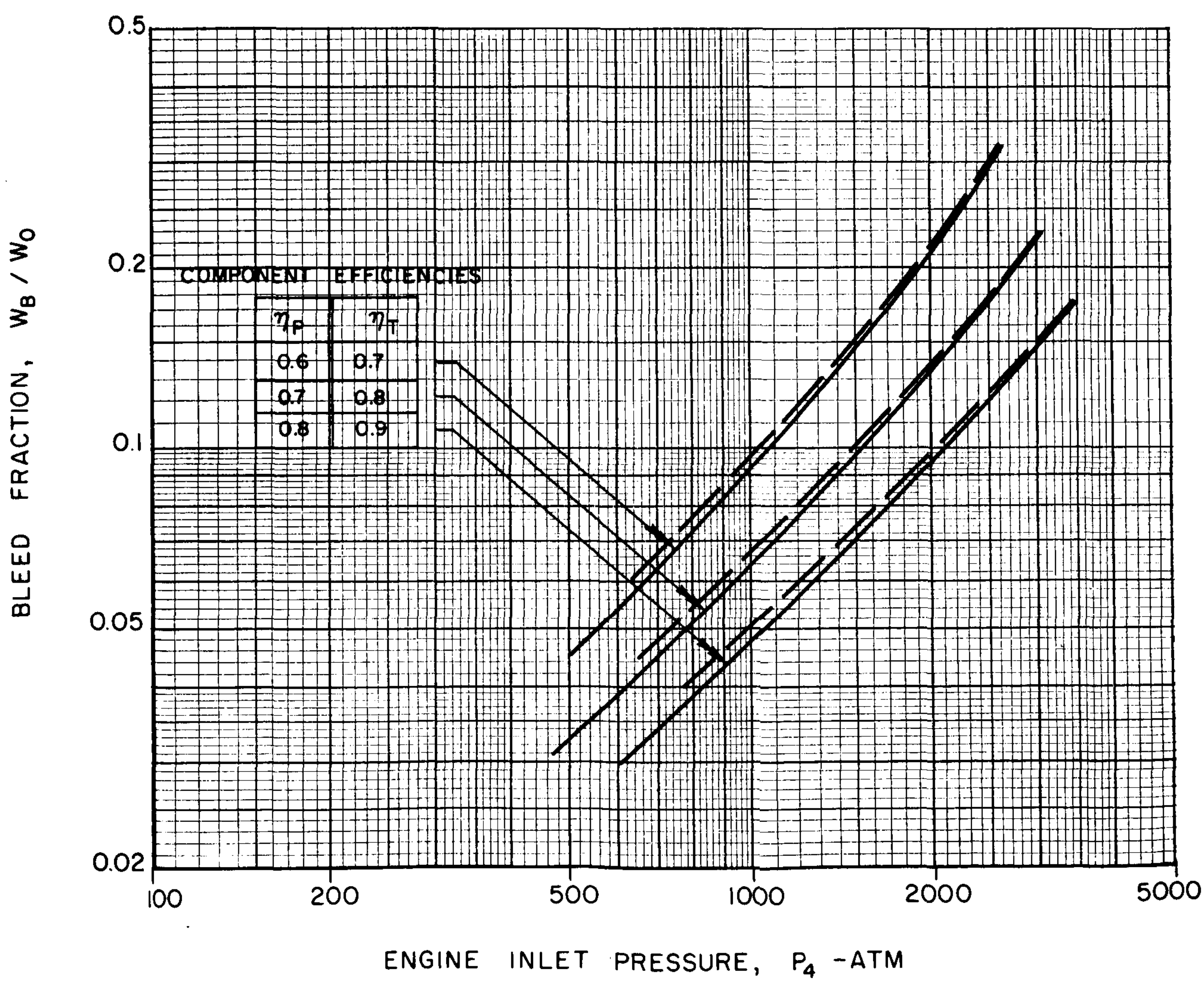

PRIMARY TURBINE PRESSURE DROP REQUIRED FOR MIXED CYCLE AND PRIMARY TURBINE INLET TEMPERATURE OF 3800 R

CORRESPONDING VALUE OF BLEED FLOW FRACTION GIVEN IN FIG. 24
FRACTION OF WORK IN PRIMARY TURBINE, F = 0.5

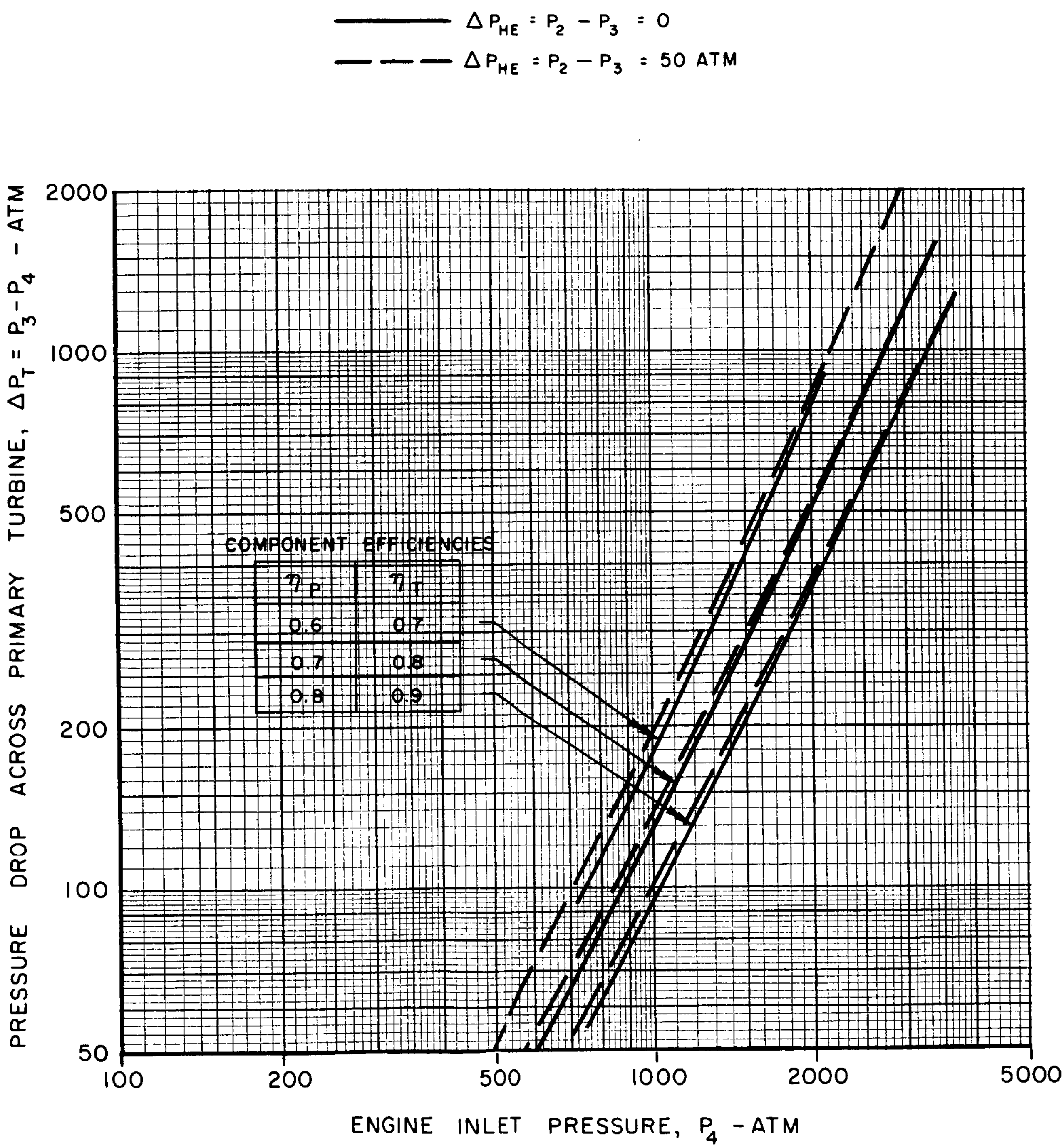

BLEED FLOW FRACTION REQUIRED FOR MIXED CYCLE AND PRIMARY TURBINE INLET TEMPERATURE OF 3800 R

CORRESPONDING VALUE OF PRIMARY TURBINE PRESSURE DROP IN FIG. 23
FRACTION OF WORK IN PRIMARY TURBINE, F=0.5

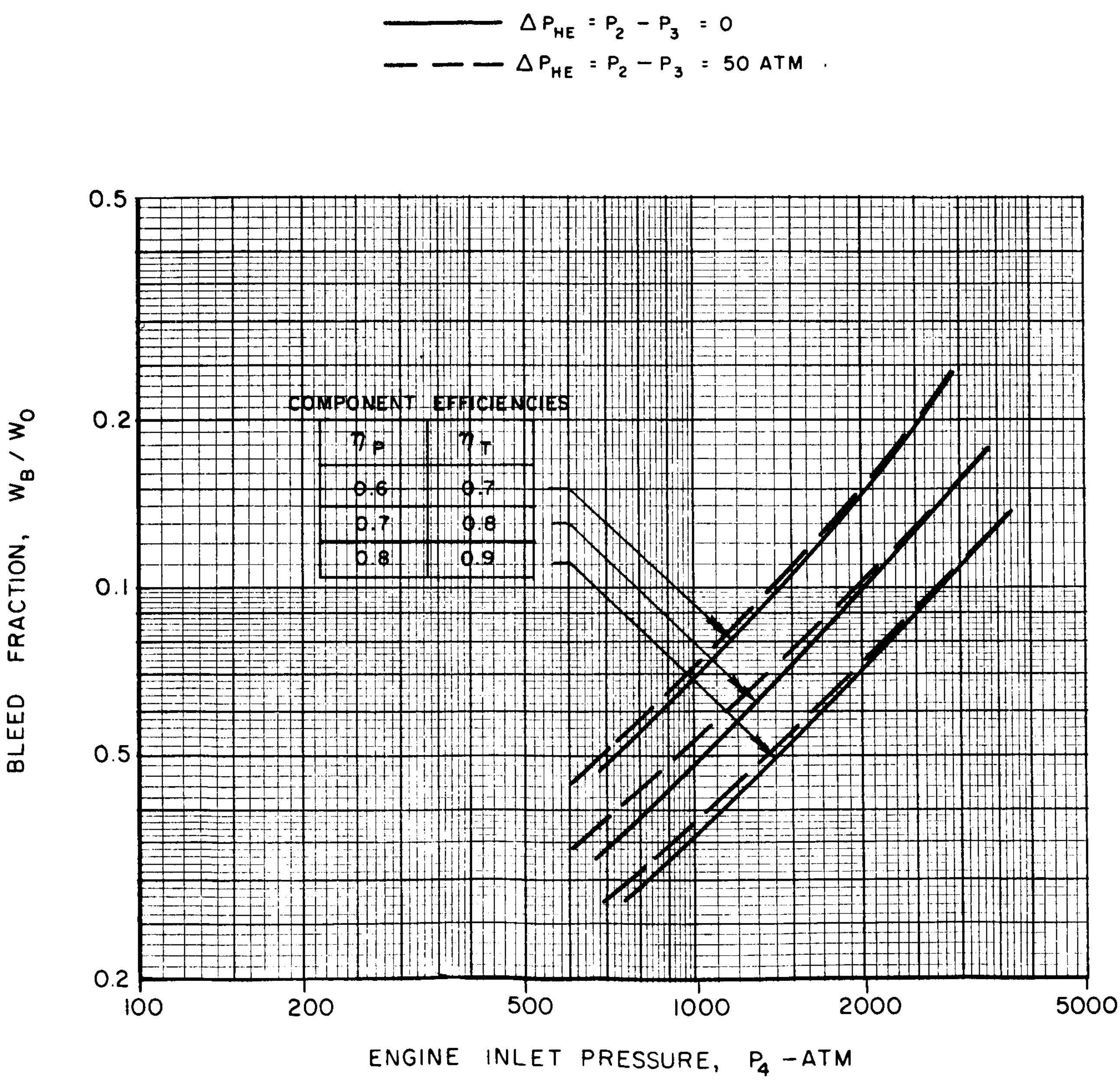

EFFECT OF PRIMARY TURBINE INLET TEMPERATURE ON MAXIMUM ENGINE INLET PRESSURES FOR MIXED CYCLE

MAXIMUM VALUES OF ENGINE INLET PRESSURE DETERMINED FROM MAXIMUM ASSUMED VALUES OF PRIMARY TURBINE PRESSURE DROP NOTED ON EACH SET OF CURVES

BLEED FRACTIONS CORRESPONDING TO EACH PRIMARY TURBINE PRESSURE DROP GIVEN IN FIG. 26

PERCENT WORK IN PRIMARY TURBINE, F = 0.5

——— $\Delta P_{HE} = P_2 - P_3 = 0$ — — — $\Delta P_{HE} = P_2 - P_3 = 50$ ATM

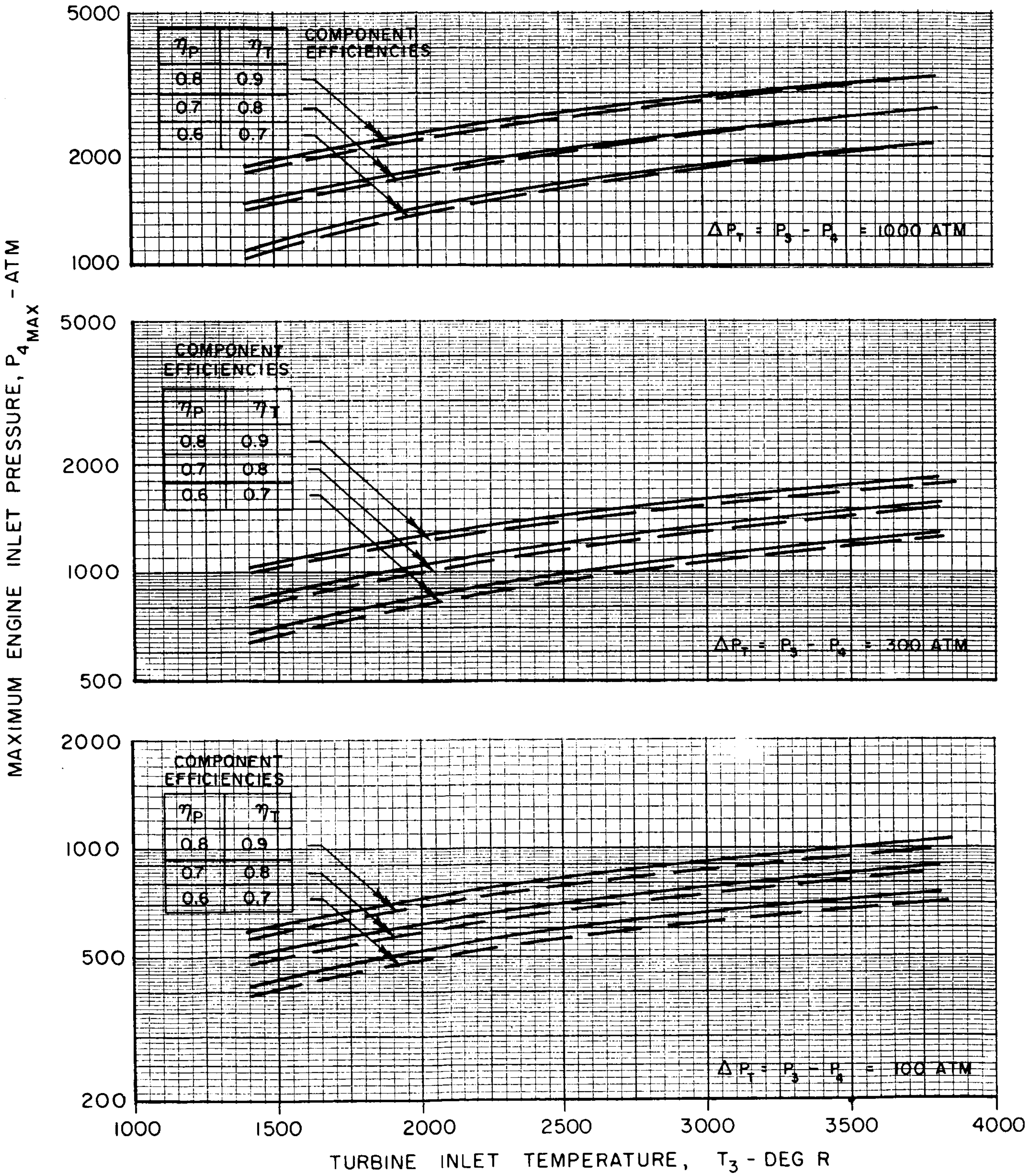

BLEED FLOW FRACTIONS REQUIRED IN MIXED CYCLE

BLEED FLOW FRACTIONS CORRESPOND TO PRIMARY TURBINE PRESSURE DROPS SHOWN IN FIG. 25

——— $\Delta P_{HE} = P_2 - P_3 = 0$

— — — $\Delta P_{HE} = P_2 - P_3 = 50$ ATM

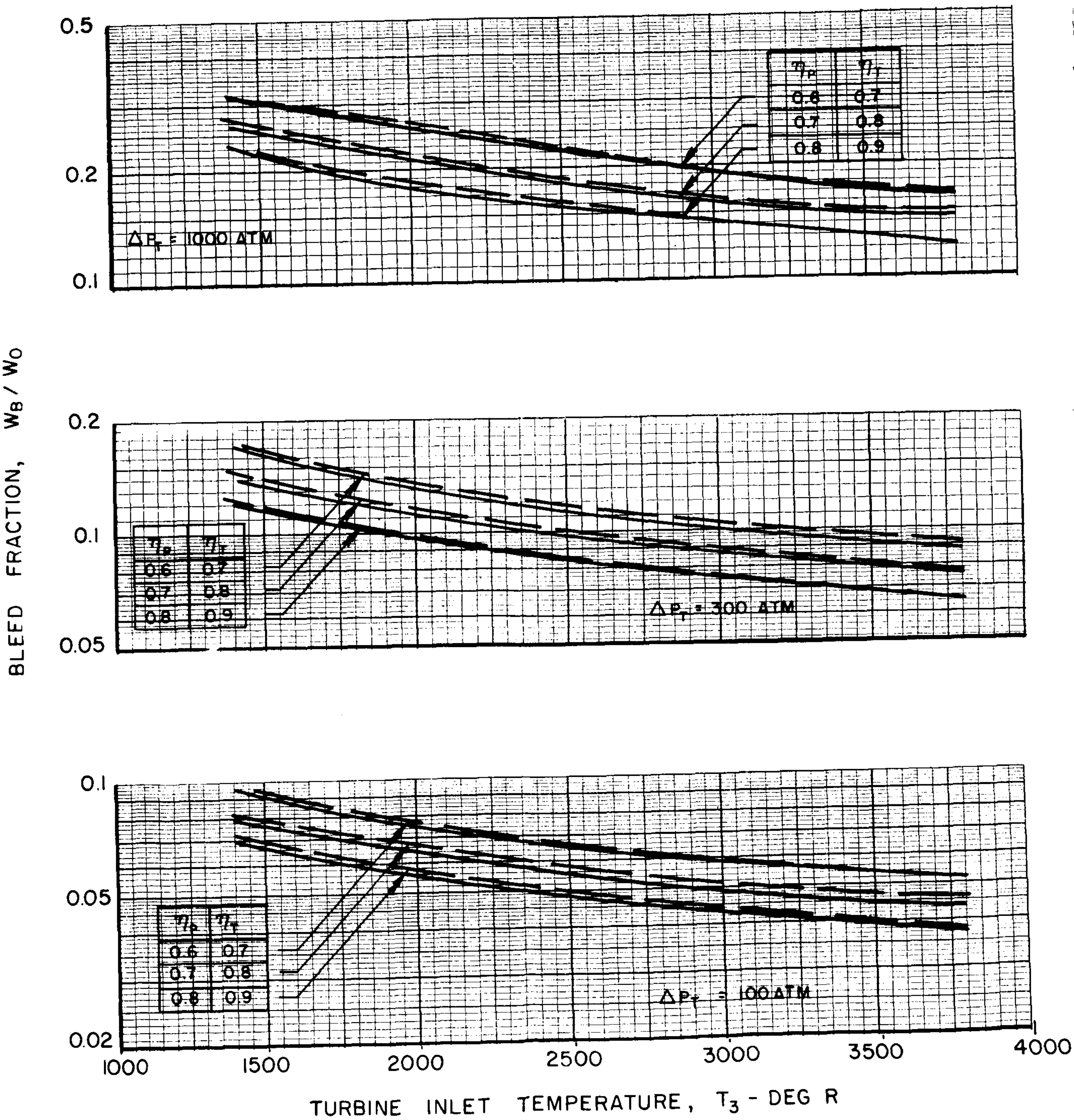

CALCULATED TEMPERATURE DISTRIBUTIONS IN FUEL-CONTAINMENT REGION

SEE APPENDIX I

$a_R R_e = 200$

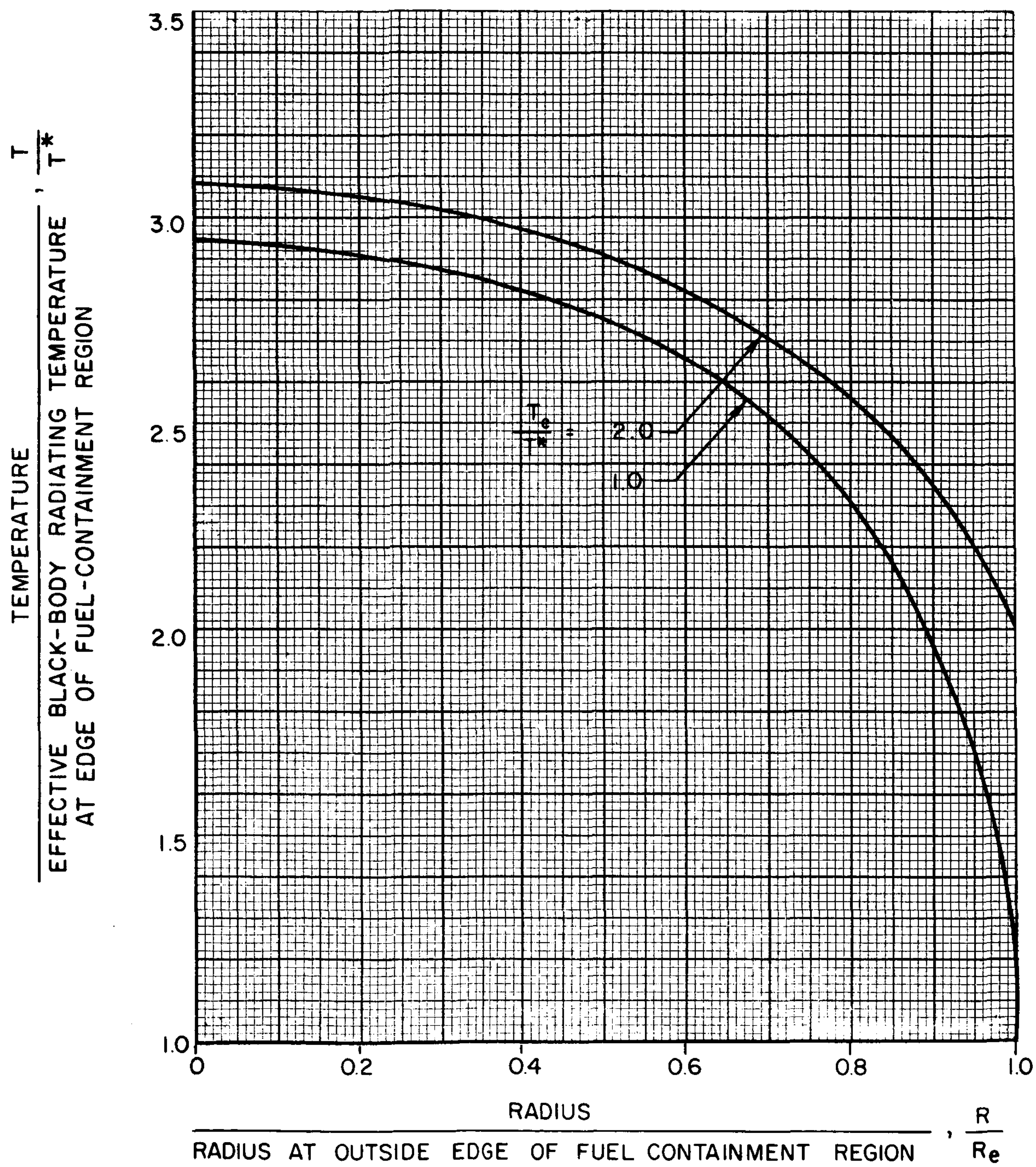

EFFECT OF DIMENSIONLESS FUEL OPACITY ON TEMPERATURE AT CENTERLINE OF FUEL-CONTAINMENT REGION

SEE APPENDIX I

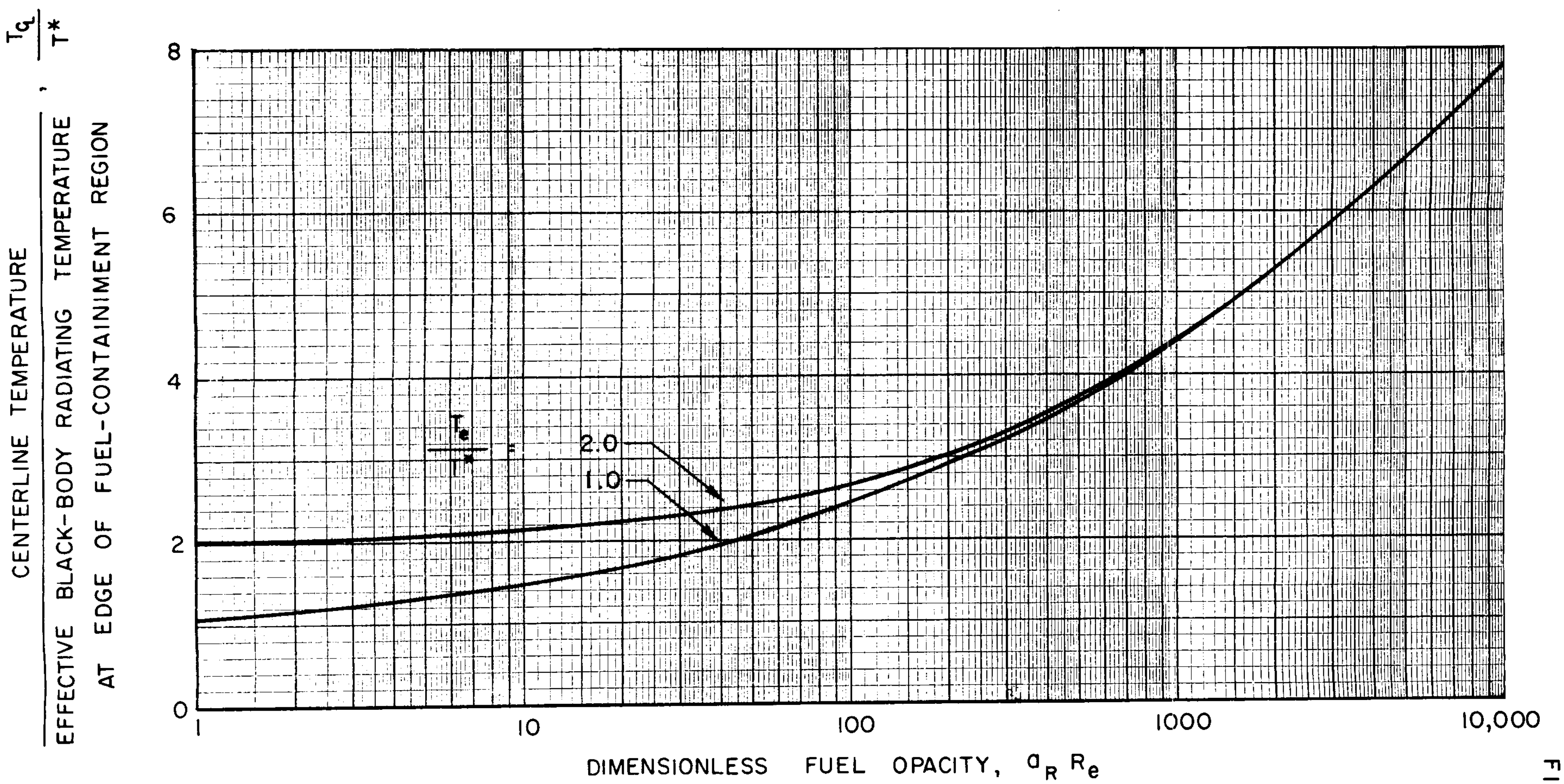

GEOMETRY OF NASA LEWIS COAXIAL-FLOW EXPERIMENT

SEE APPENDIX II AND REF. 11

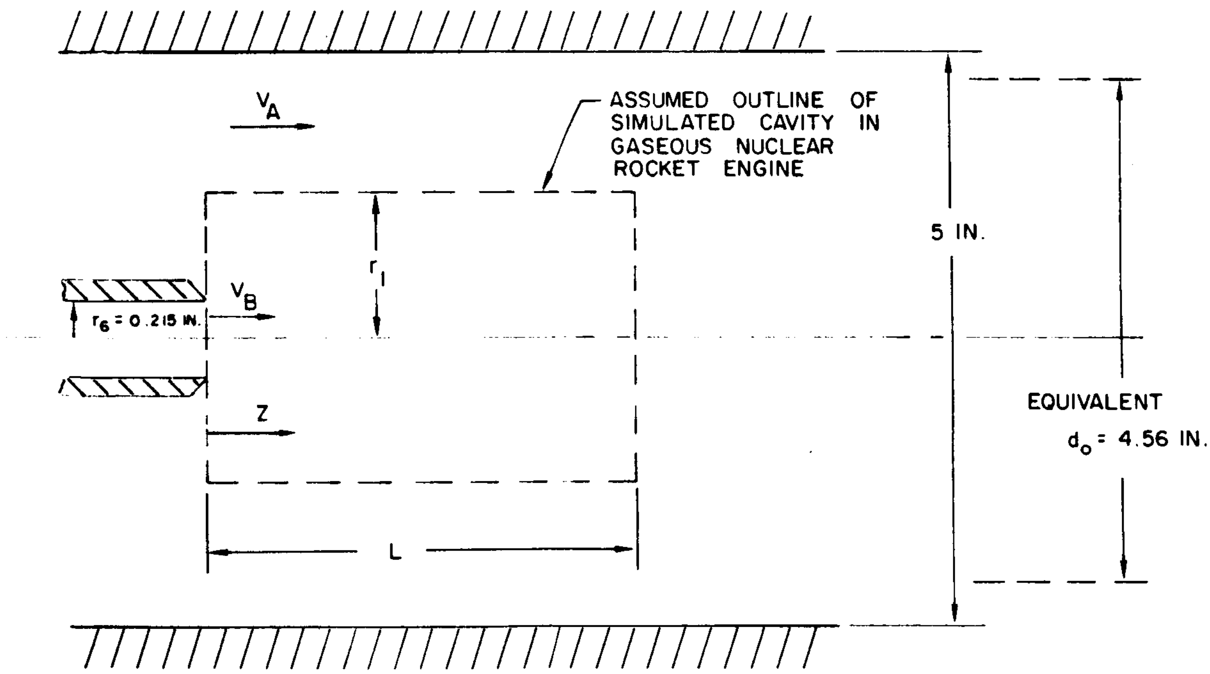

EFFECT OF REYNOLDS NUMBER ON DIMENSIONLESS BROMINE TIME CONSTANT

SEE APPENDIX II

$L/r_6 = 8$ $L/r_1 = 6$

$r_6/r_1 = 0.75$

NUMBERS NEXT TO SYMBOLS DESIGNATE RUN NOS. FROM REF. 11 (SEE TABLE II)

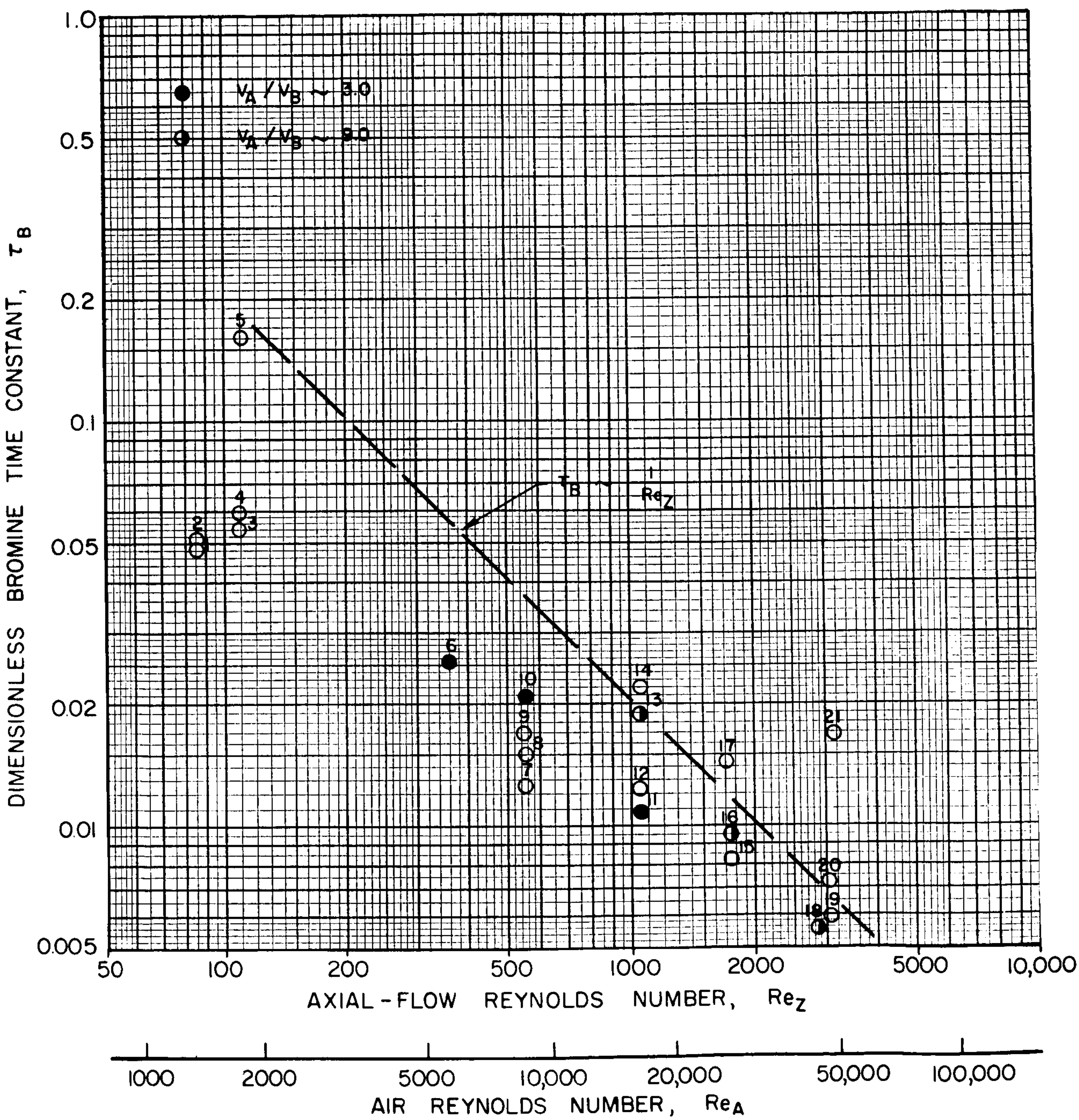

EFFECT OF REYNOLDS NUMBER ON BROMINE - AIR DENSITY RATIO

SEE APPENDIX II

$L/r_6 = 8$ $L/r_1 = 6$

$r_6/r_1 = 0.75$

NUMBERS NEXT TO SYMBOLS DESIGNATE RUN NUMBERS FROM REF. II (SEE TABLE II)

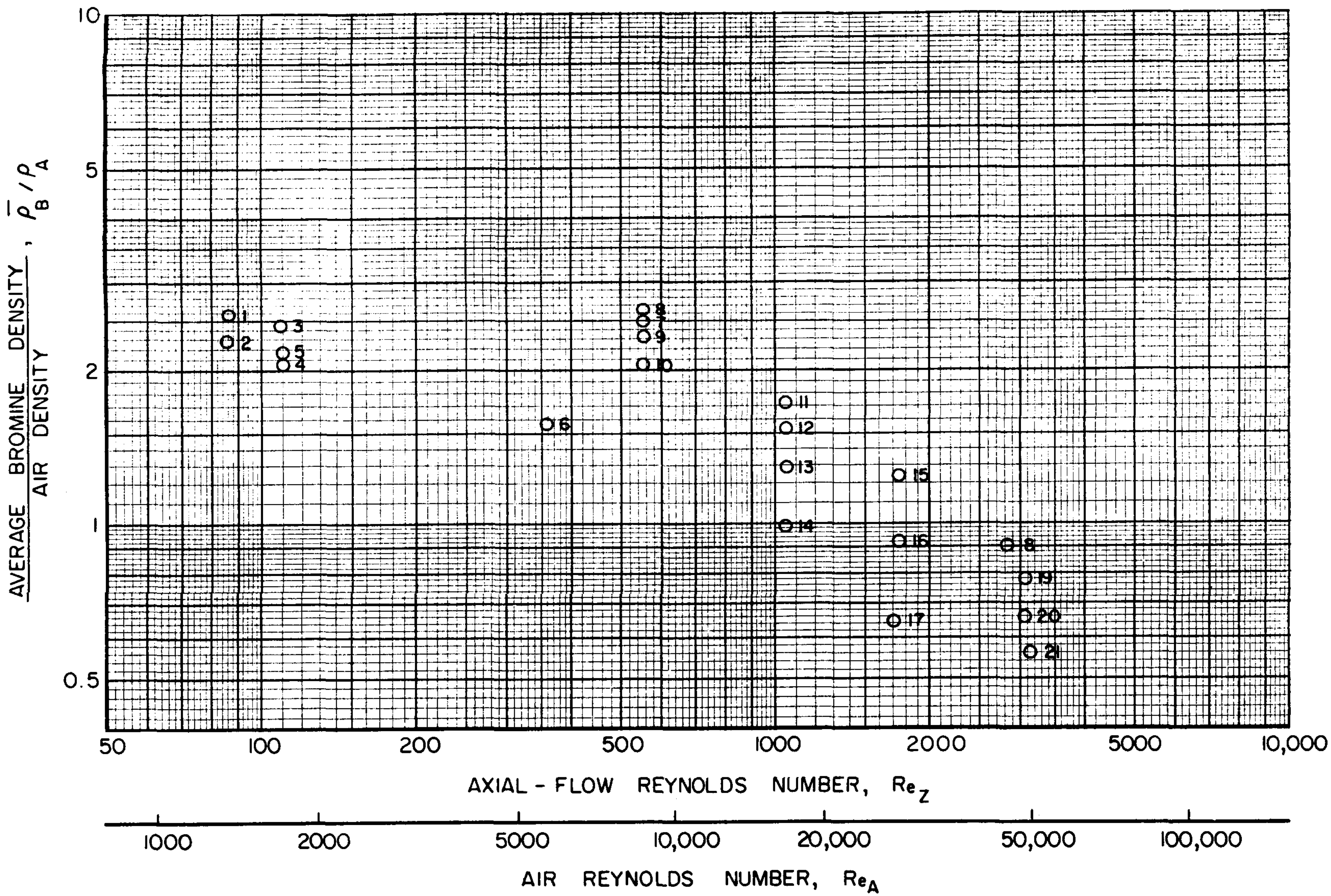

TYPICAL EFFECT OF CAVITY LENGTH-TO-DIAMETER RATIO ON DIMENSIONLESS BROMINE TIME CONSTANT

SEE APPENDIX II

$r_6 / r_1 = 0.75$

NUMBERS NEXT TO CURVES DESIGNATE RUN NUMBERS FROM REF. 11 (SEE TABLE II)

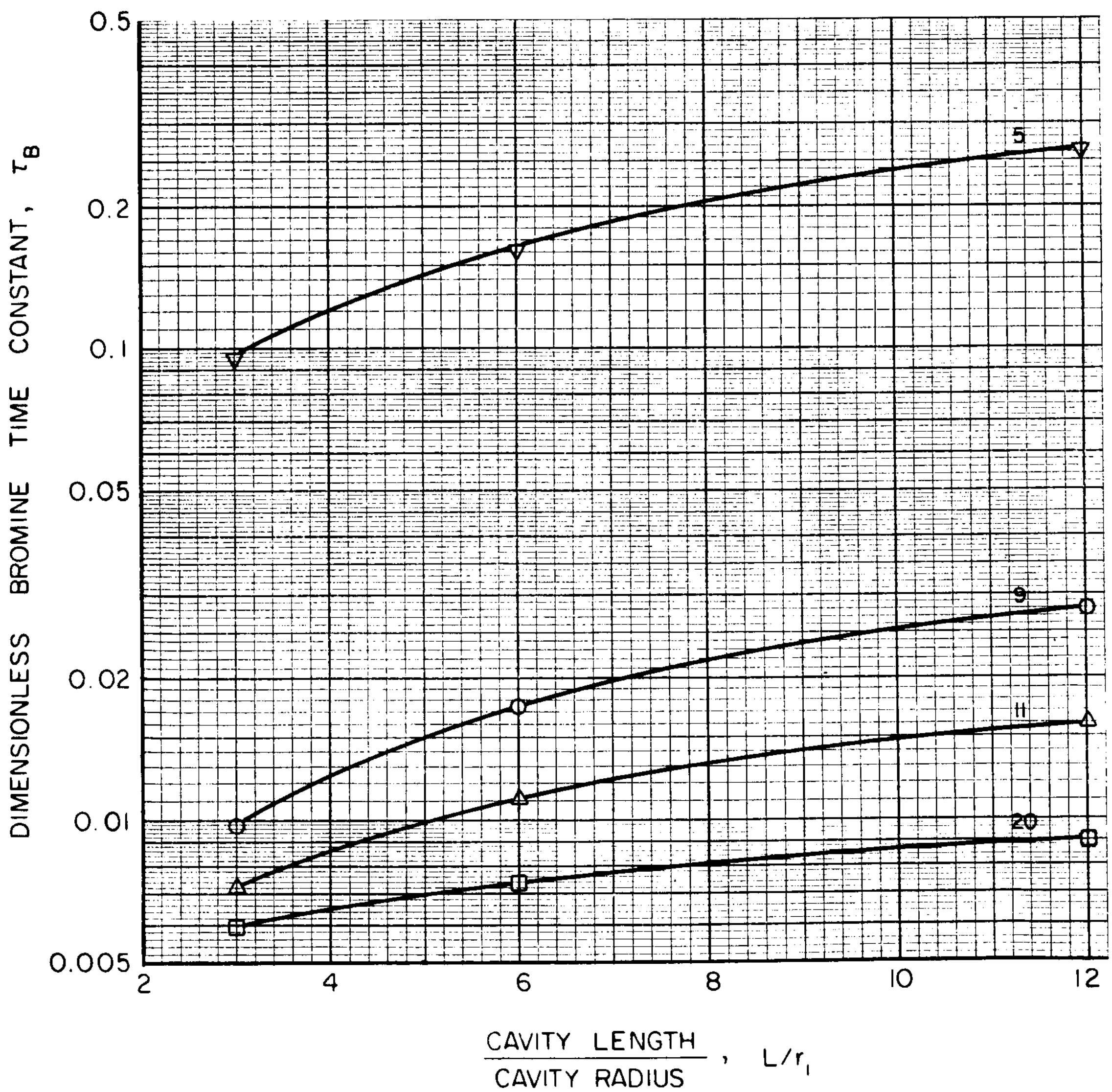

EFFECT OF CAVITY LENGTH-TO-DIAMETER RATIO ON BROMINE - AIR DENSITY RATIO

SEE APPENDIX II

$r_6 / r_1 = 0.75$

NUMBERS NEXT TO CURVES DESIGNATE RUN NUMBERS FROM REF. 11 (SEE TABLE II)

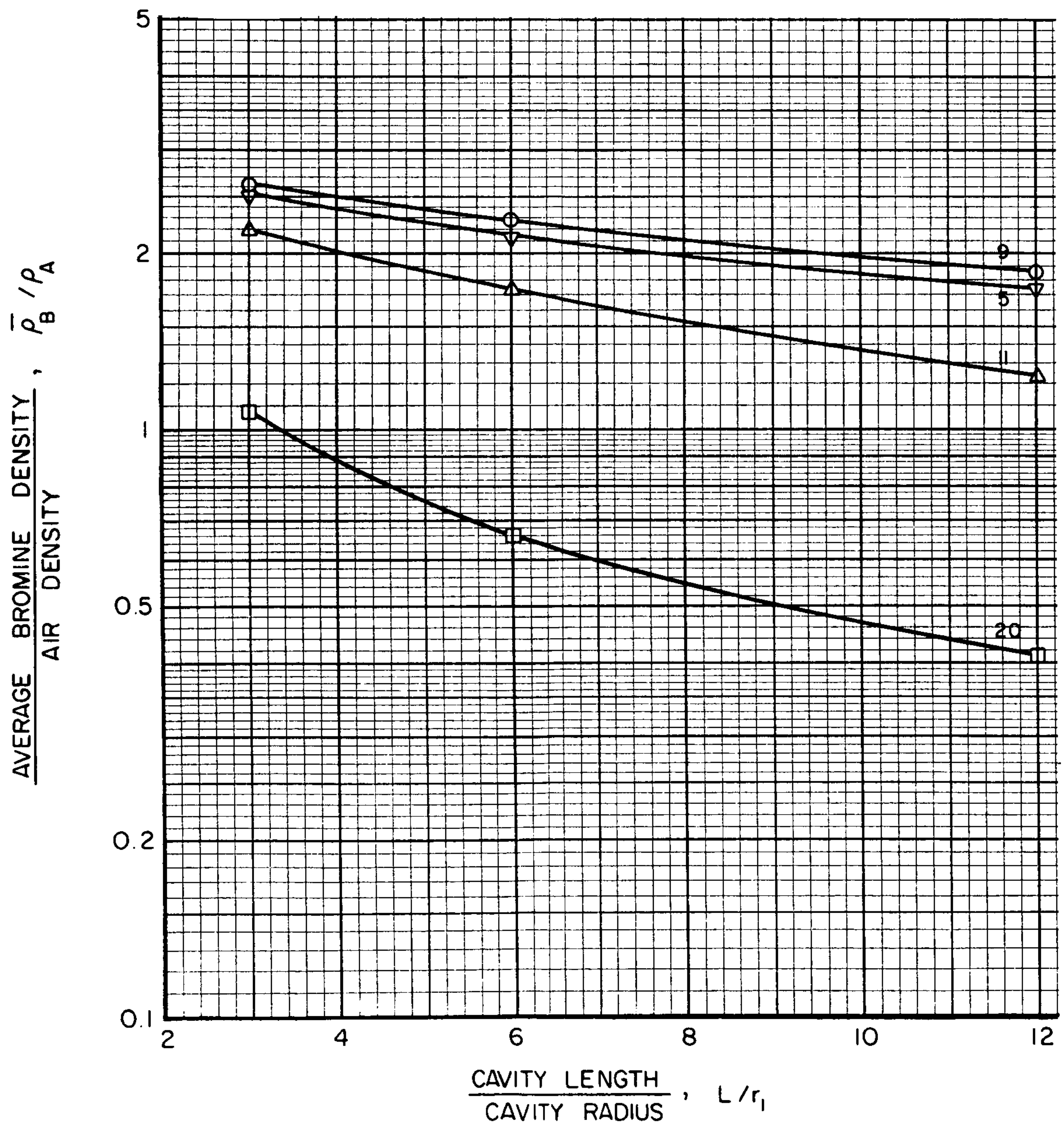

EFFECT OF BROMINE-TO-AIR DENSITY RATIO ON DIMENSIONLESS BROMINE TIME CONSTANT

SEE APPENDIX II

$L/r_6 = 8$ $L/r_1 = 6$

$r_6/r_1 = 0.75$

NUMBERS NEXT TO SYMBOLS DESIGNATE RUN NOS. FROM REF. 11 (SEE TABLE II)

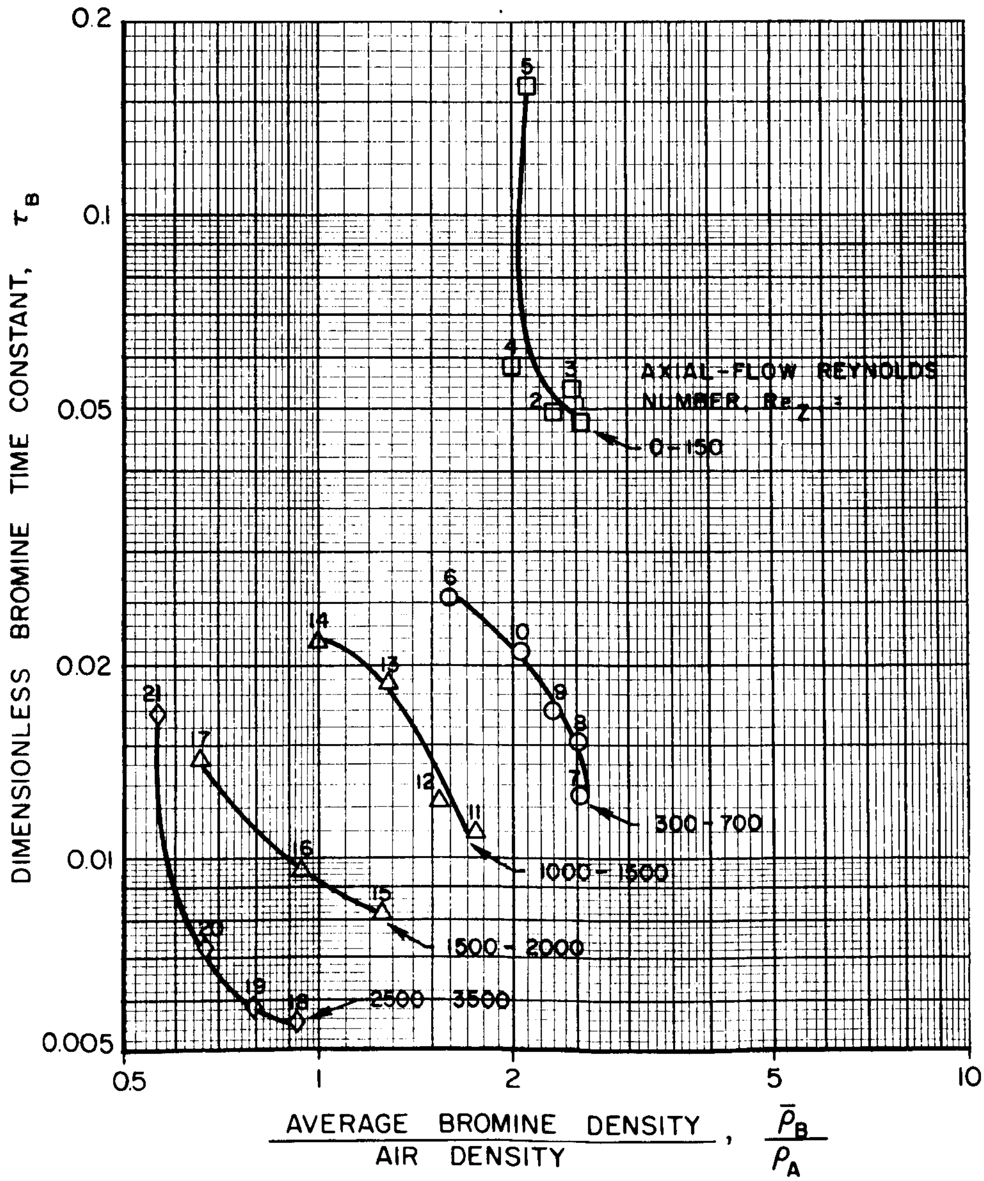

D-910093-19

FIG. 35

GEOMETRY EMPLOYED IN ANALYSIS OF FUEL-INJECTION DUCT FOR GASEOUS NUCLEAR ROCKETS

SEE APPENDIX III

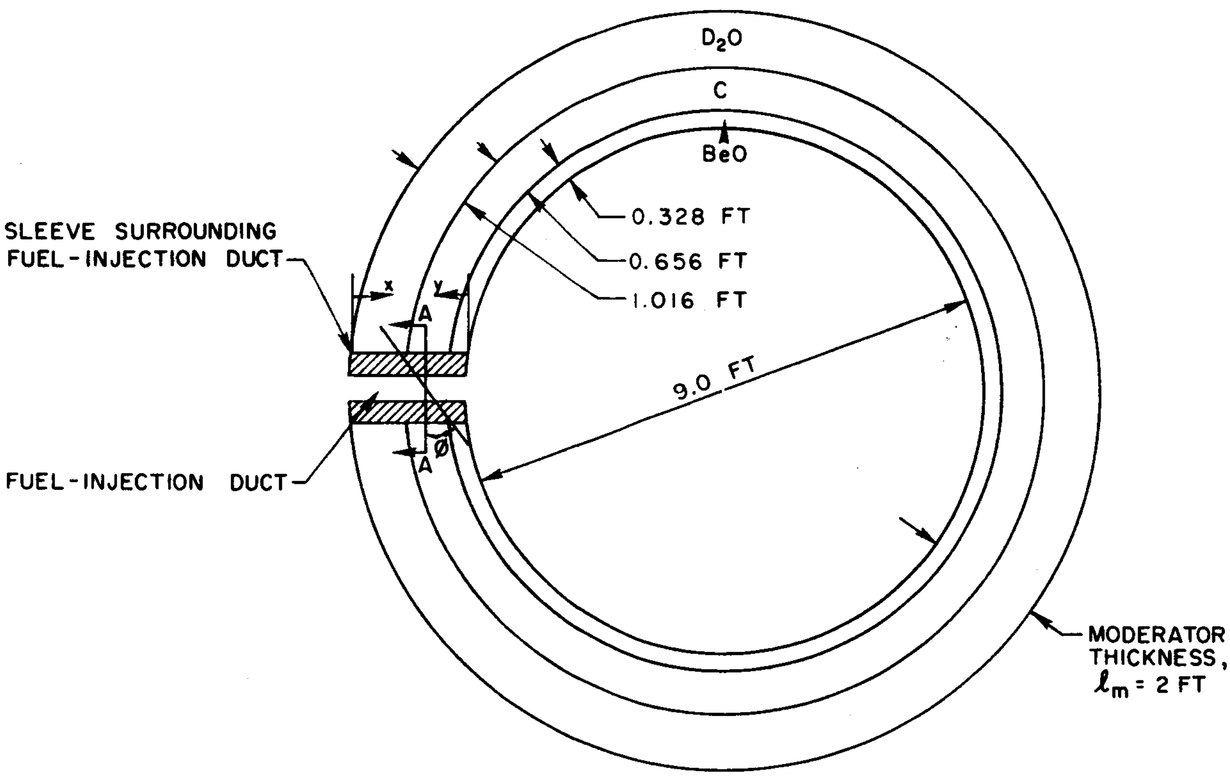

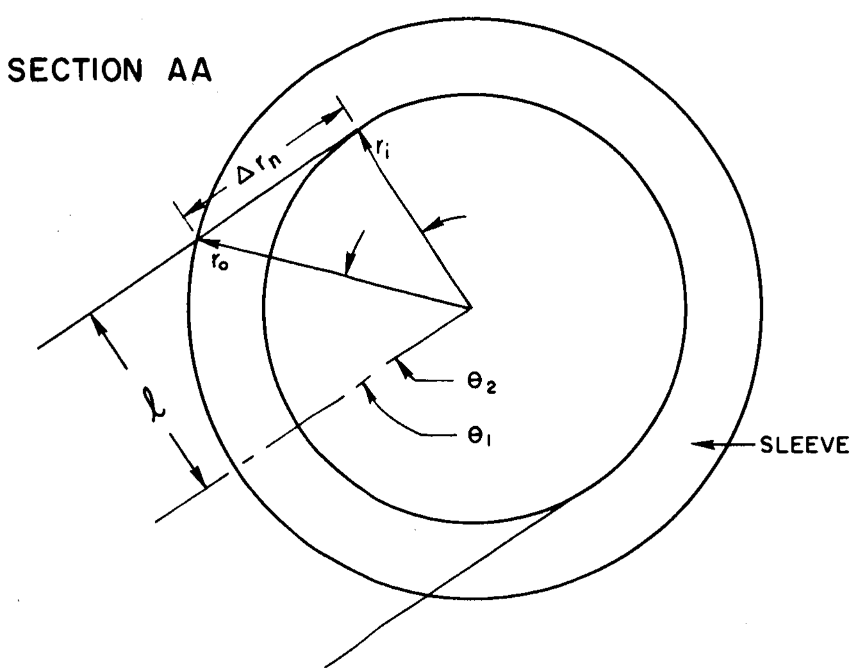

INFLUENCE OF EFFECTIVE THICKNESS OF SLEEVE SURROUNDING FUEL-INJECTION DUCT ON NEUTRON FLUX WITHIN FUEL-INJECTION DUCT

SEE APPENDIX III

$(r_o - r_i)$ = THICKNESS OF SLEEVE (SEE FIG. 35)

Σ_a = MACROSCOPIC NEUTRON ABSORPTION CROSS SECTION OF SLEEVE WALL MATERIAL

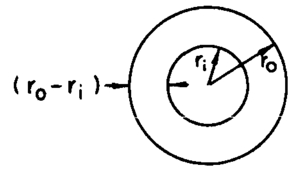

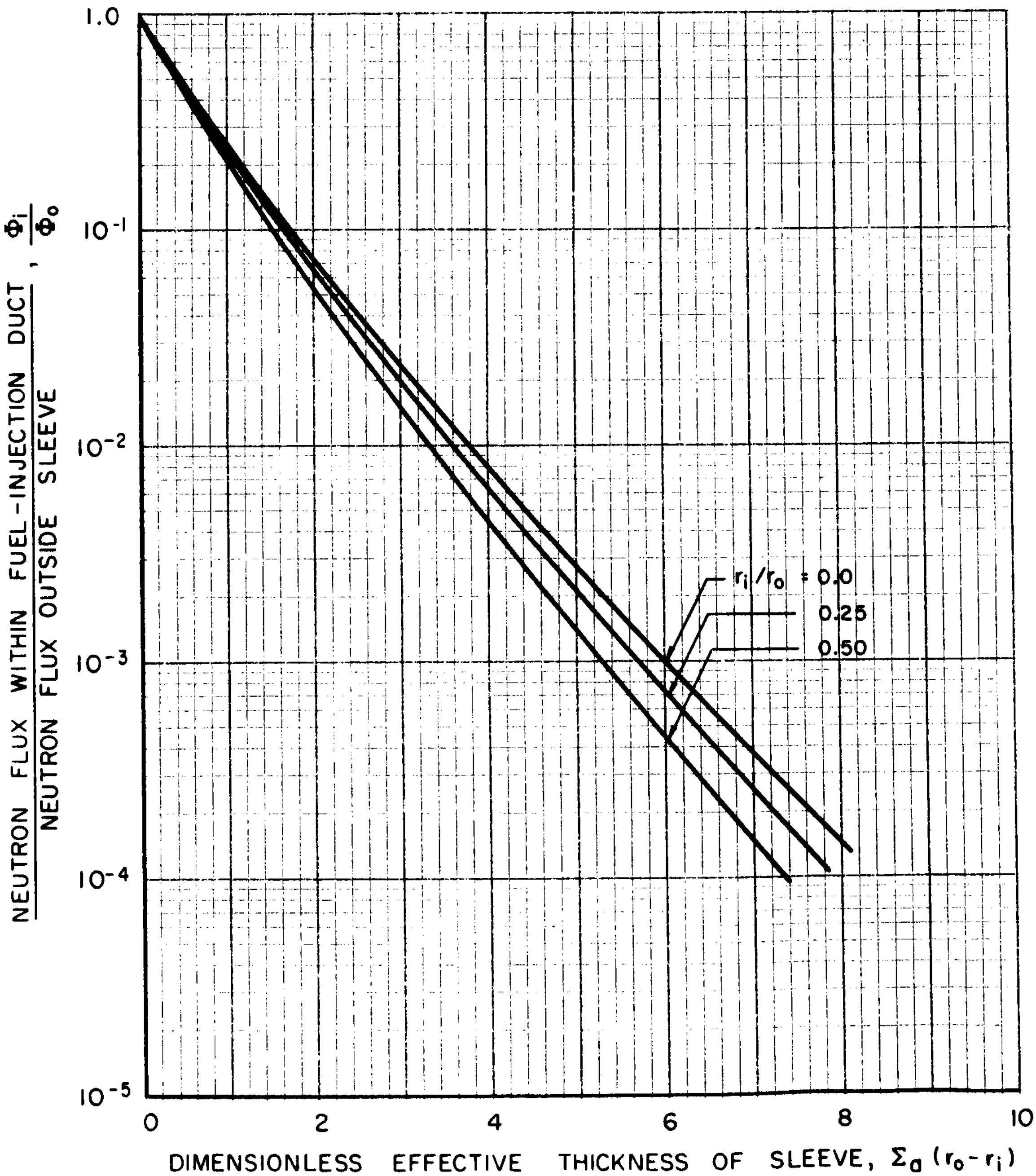

HEAT GENERATION IN FUEL WITHIN FUEL-INJECTION DUCT DUE TO THE NEUTRON FLUX PASSING THROUGH SLEEVE WALL

SEE APPENDIX III
HAFNIUM EMPLOYED AS SLEEVE WALL MATERIAL
INSIDE RADIUS OF SLEEVE = 0.04 IN. = 0.1 CM
END EFFECT NEGLECTED (SEE FIG. 38)

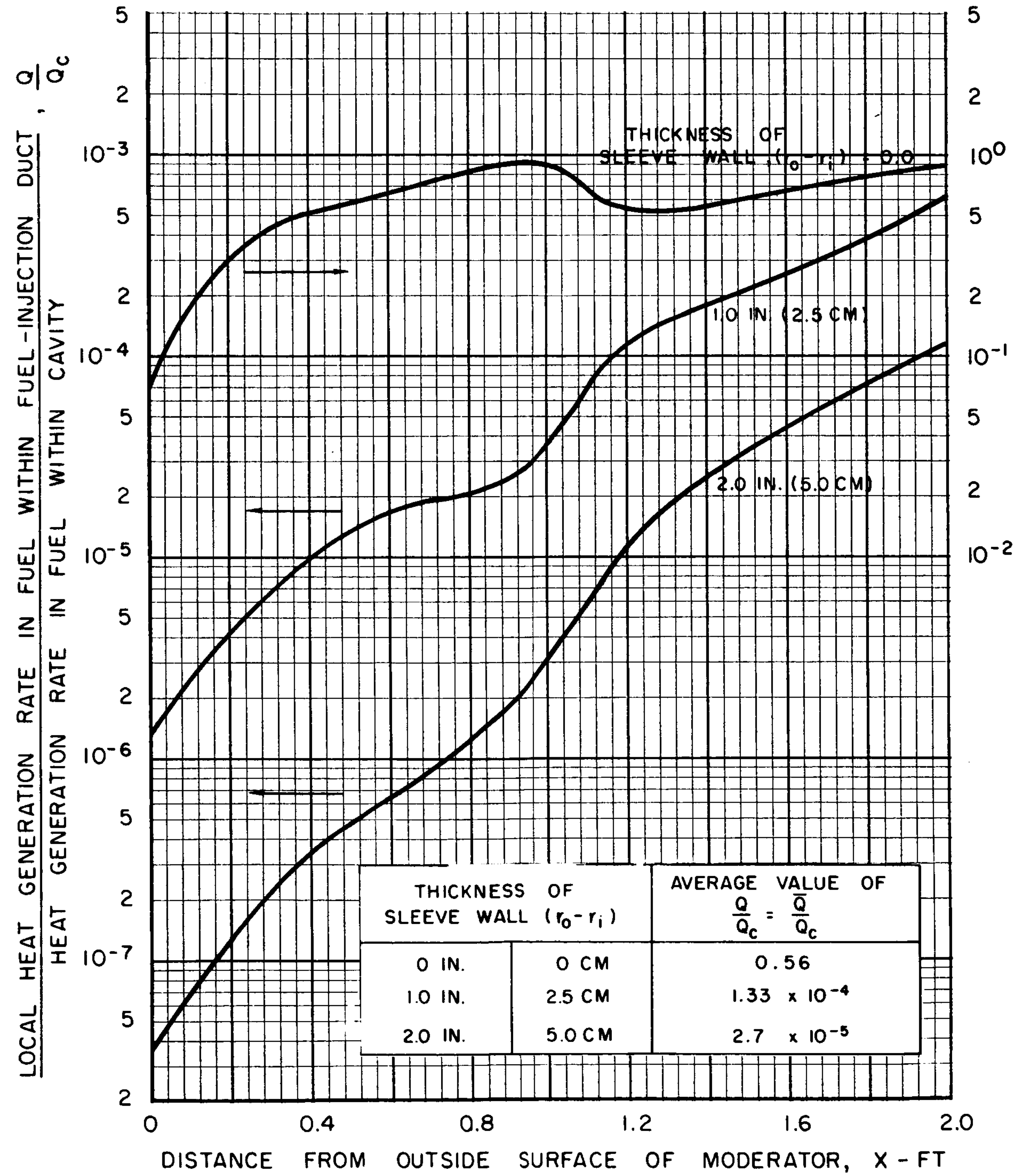

THICKNESS OF SLEEVE WALL $(r_o - r_i)$		AVERAGE VALUE OF $\frac{Q}{Q_c} = \frac{\overline{Q}}{Q_c}$
0 IN.	0 CM	0.56
1.0 IN.	2.5 CM	1.33×10^{-4}
2.0 IN.	5.0 CM	2.7×10^{-5}

HEAT GENERATION RATE IN FUEL WITHIN FUEL-INJECTION DUCT DUE TO UNCOLLIDED NEUTRON FLUX FROM CAVITY

SEE APPENDIX III

FLUX PASSING THROUGH WALL OF SLEEVE NEGLECTED (SEE FIG. 37)

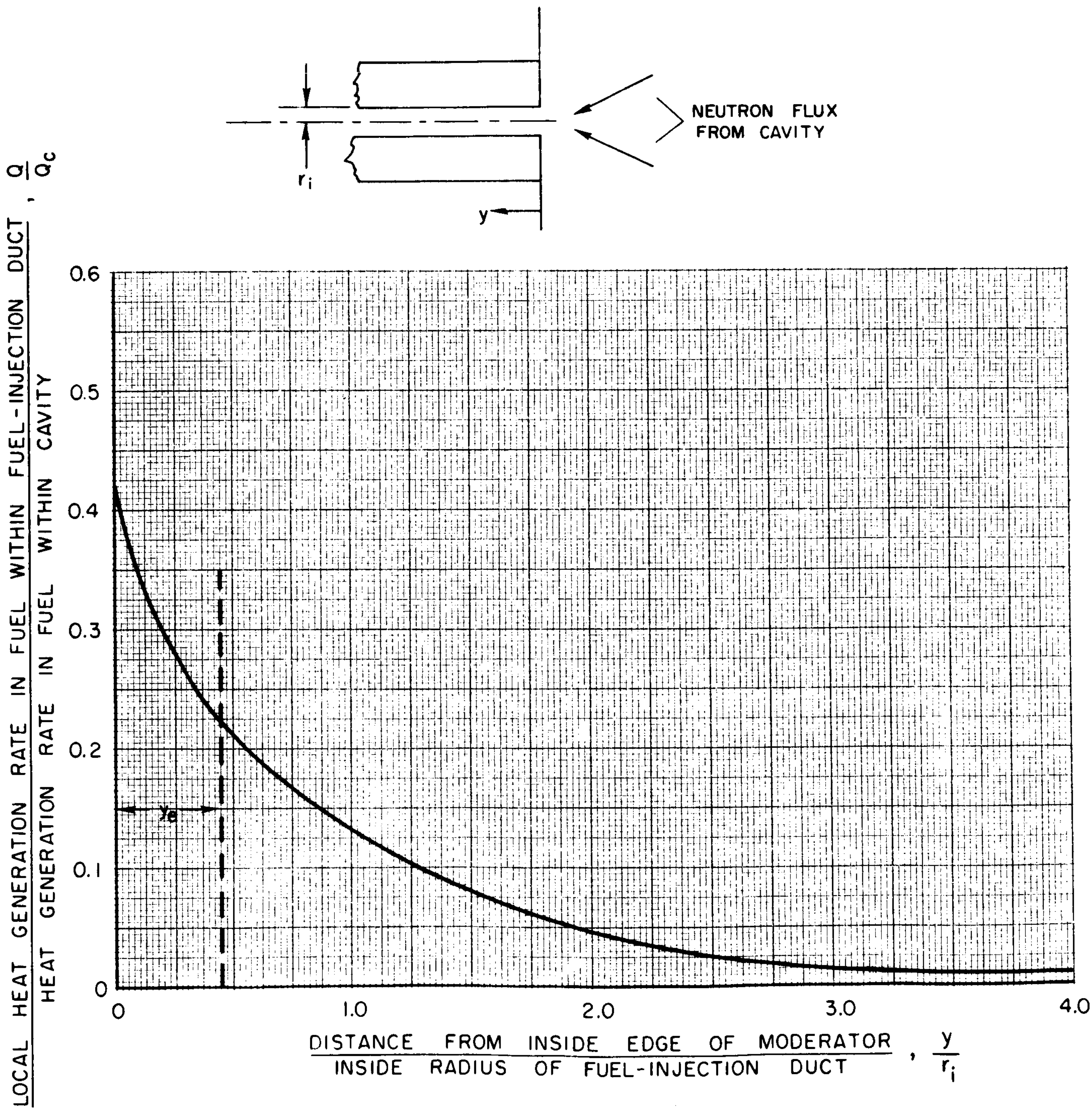

OVERALL AVERAGE HEAT GENERATION RATE OF FUEL WITHIN FUEL – INJECTION DUCT

SEE APPENDIX III
HAFNIUM EMPLOYED AS SLEEVE WALL MATERIAL
CURVES OBTAINED FROM FIGS. 37 AND 38

TO USE CURVE, $\Delta H_f = B\,Q_c\,t_{fs} = B\,Q_c\,\frac{\ell m}{V_t}$

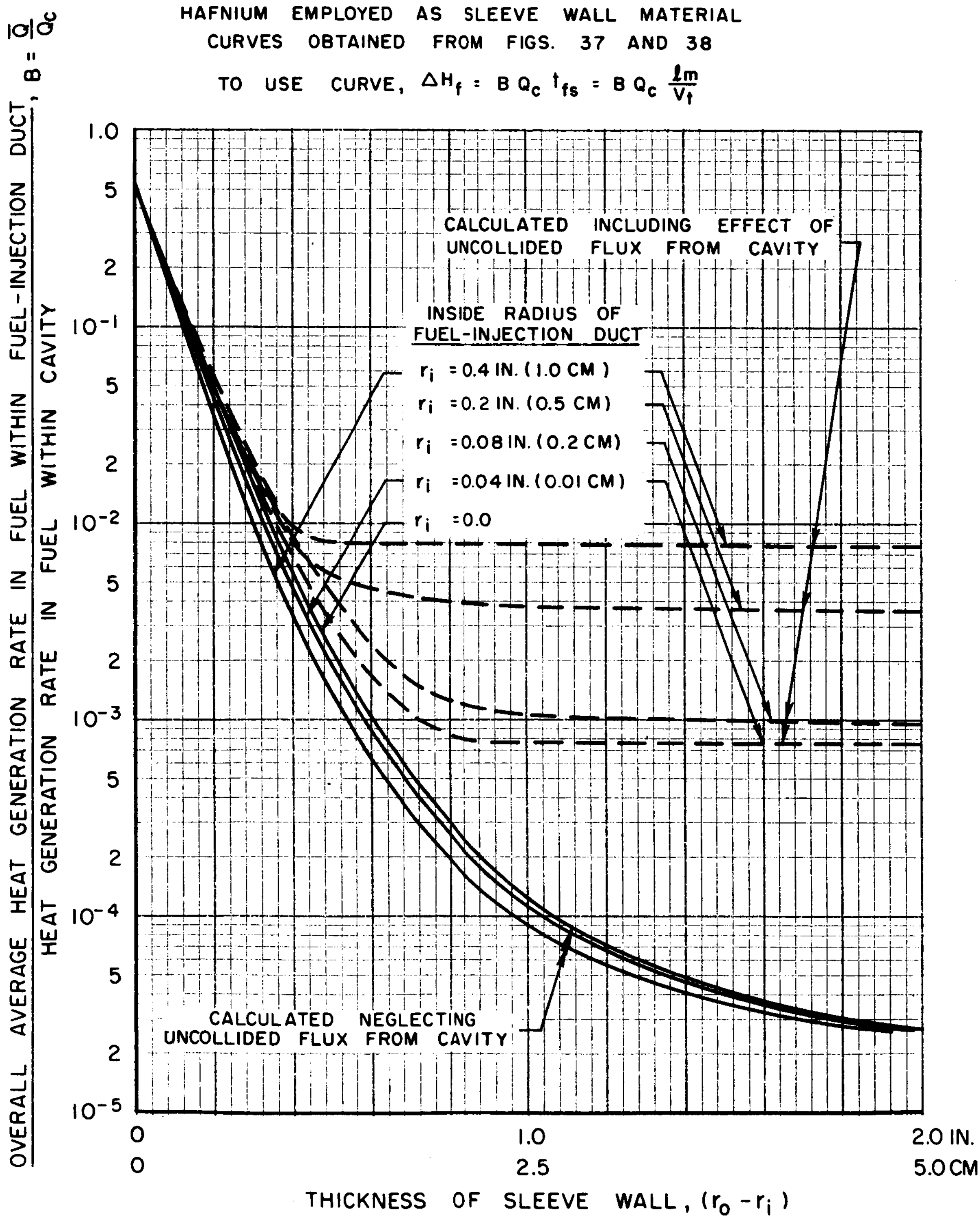

DISTRIBUTION LIST

	Copy No.
Space Nuclear Propulsion Office U. S. Atomic Energy Commission Washington, D. C. 20545 Attention: Mr. H. B. Finger	1
Space Nuclear Propulsion Office U. S. Atomic Energy Commission Washington, D. C. 20545 Attention: Captain W. A. Yingling	2
Argonne National Laboratory 9700 South Cass Avenue Argonne, Illinois Attention: John Marchaterre	3
Los Alamos Scientific Laboratory P. O. Box 1663 Los Alamos, New Mexico 87544 Attention: N Division	4
Los Alamos Scientific Laboratory P. O. Box 1663 Los Alamos, New Mexico 87544 Attention: Ralph Cooper	5
Los Alamos Scientific Laboratory P. O. Box 1663 Los Alamos, New Mexico 87544 Attention: John Orndoff	6
U. S. Atomic Energy Commission Brookhaven Area Office Upton, New York Attention: E. L. Van Horn	7
U. S. Atomic Energy Commission Headquarters Library, Reports Section Mail Station G-017 Washington, D. C. 20545	8

DISTRIBUTION LIST (cont'd)

	Copy No.
AEC, Division of Technical Information Extension P. O. Box 62 Oak Ridge, Tennessee	9
Oak Ridge National Laboratory Oak Ridge, Tennessee Attention: Dr. John Keyes	10
Office of Advance Research and Technology NASA Headquarters 1520 H Street, NW Washington, D. C. Attention: Dr. James B. Edson	11
NASA, Lewis Research Center 21000 Brookpark Road Cleveland, Ohio 44135 Attention: Frank Rom	12
NASA, Lewis Research Center 21000 Brookpark Road Cleveland, Ohio 44135 Attention: Robert Ragsdale	13
National Aeronautics and Space Administration George C. Marshall Space Flight Center Huntsville, Alabama Attention: Library	14
National Aeronautics and Space Administration George C. Marshall Space Flight Center Huntsville, Alabama Attention: Will Jordan	15
NASA, Goddard Space Flight Center Glenn Dale Road Greenbelt, Maryland Attention: Librarian	16
National Aeronautics and Space Administration Office of Scientific and Technical Information Washington, D. C. 20546 Attention: AFSS-LL	17

DISTRIBUTION LIST (cont'd)

	Copy No.
Headquarters NASA Washington, D. C. 20546 Attention: OART	18
Jet Propulsion Laboratory 4800 Oak Grove Drive Pasadena 3, California Attention: H. Denslow	19
Space Technology Laboratory, Inc. P. O. Box 95001 Los Angeles 45, California Attention: M. N. Sloane (Librarian)	20
National Aeronautics and Space Administration Manned Spacecraft Center P. O. Box 1537 Houston 1, Texas Attention: Library	21
National Aeronautics and Space Administration Langley Research Center Langley Air Force Base Virginia Attention: Library	22
National Aeronautics and Space Administration Washington, D. C. 20546 Attention: Office of Technical Information and Educational Programs, Code ETL	23
National Aeronautics and Space Administration Washington, D. C. 20546 Attention: R. W. Ziem (RPS)	24
Jet Propulsion Laboratory 4800 Oak Grove Drive Pasadena 3, California Attention: L. E. Newlan Chief, Reports Group	25

DISTRIBUTION LIST (cont'd)

	Copy No.
Air Force Rocket Propulsion Laboratory Edwards Air Force Base California 93523 Attention: Mr. J. B. Mullen (RPRRA)	26
RTD (RTNP) Bolling Air Force Base Washington 25, D. C. Attention: Major T. P. Mott-Smith	27
HQ USAF (AFRNE) Washington 25, D. C. Attention: Col. J. Burke	28
SSD (SSTRP) UF Unit Post Office Los Angeles 45, California Attention: Major F. E. Baker	29
ASD (ASAPRD-NS) Wright-Patterson Air Force Base, Ohio	30
AFSWL Kirtland Air Force Base, New Mexico Attention: Captain William A. Anders	31
SAC (OAWS) Offutt Air Force Base, Nebraska	32
DDR&E (OAP) Washington 25, D. C. Attention: J. E. Jackson	33
DDR&E (WSEG) Washington 25, D. C. Attention: OSD	34
AFSC (SCTD) Andrews Air Force Base Washington 25, D. C.	35

DISTRIBUTION LIST (cont'd)

	Copy No.
AUL (AUL3T-7143) Maxwell Air Force Base, Alabama Attention: E. C. Perkins	36
Aerospace Corporation P. O. Box 95085 Los Angeles 45, California Attention: Dr. C. J. Wang	37
Aerospace Corporation P. O. Box 95085 Los Angeles 45, California Attention: Library-Documents	38
USAFA (Astronautics Department) USAF Academy, Colorado Attention: Col. Joseph Hale	39
AFIT (AFIT-SE-Phys) c/o Security Officer AFIT Wright-Patterson AFB, Ohio Attention: Charles J. Bridgman	40
Commander AFSC Foreign Technology Division Wright-Patterson Air Force Base, Ohio Attention: RTD (TD-E3b)	41
Superintendent U. S. Naval Postgraduate School Naval Academy Monterey, California	42
Air Force Office of Scientific Research Washington 25, D. C. Attention: SREP, Dr. J. F. Masi	43
Aeronautical Research Laboratory Wright-Patterson Air Force Base, Ohio Attention: Major Keller	44

DISTRIBUTION LIST (cont'd)

	Copy No.
General Dynamics/Astronautics Technical Library San Diego 12, California Attention: Louis Canter	45
Douglas Aircraft Co., Inc. Santa Monica, California Attention: J. L. Waisman	46
Bellcomm, Incorporated 1100 Seventeenth Street, NW Washington, D. C. 20036 Attention: Maxwell W. Hunter, Director Flight Systems Division	47
Aerojet-General Corporation P. O. Box 573 Azusa, California Attention: Mrs. E. Henry	48
Aerojet-General Nucleonics P. O. Box 78 San Ramon, California Attention: B. Probert	49
Boeing Company Aero Space Division P. O. Box 3707 Seattle 24, Washington Attention: R. R. Barber	50
Martin Nuclear, A Division of Martin-Marietta Corp. P. O. Box 5042 Middle River 3, Maryland Attention: Library	51
Marquardt Corporation 16555 Saticoy Street Van Nuys, California Attention: J. J. Norton	52

DISTRIBUTION LIST (cont'd)

	Copy No.
Pratt & Whitney Aircraft 400 Main Street East Hartford, Connecticut Attention: W. H. Podolny	53
General Electric Co., NMPO P. O. Box 15132 Cincinnati 15, Ohio Attention: J. W. Stephenson	54
Rocketdyne P. O. Box 552 Canoga Park, California Attention: C. C. Bennett	55
Bell Aerosystems Box 1 Buffalo 5, New York Attention: T. Reinhardt	56
Westinghouse Electric Corporation Astronuclear Laboratory P. O. Box 10864 Pittsburgh 36, Pennsylvania Attention: F. McKenna	57
Allison Division - GMC P. O. Box 24013 Indianapolis 24, Indiana Attention: R. R. Blackwell	58
Chrysler Corporation Defense Operations Div. Box 757 Detroit 31, Michigan	59
North American Aviation, Inc. Space and Information Systems Division 12214 Lakewood Boulevard Downey, California Attention: Tech. Information Center (L. M. Foster)	60

DISTRIBUTION LIST (cont'd)

	Copy No.
Grumman Aircraft Engineering Corporation Bethpage, Long Island, New York Attention: M. O. Friedlander Engineering Library, Plant 5	61
General Electric Company MSVD Library Documents Group, Rm 3446 3198 Chestnut Street Philadelphia 1, Pennsylvania	62
Lockheed Missiles and Space Company Division of Lockheed Aircraft Corporation Sunnyvale, California Attention: H. F. Plank, Bldg. 153, DCS-G	63
Aerojet-General Corporation 11711 South Woodruff Avenue Downey, California Attention: Florence Walsh, Librarian	64
Aerojet-General Corporation P. O. Box 1947 Sacramento, California Attention: Technical Information Office	65
General Electric Company Cincinnati 15, Ohio Attention: Technical Information Center	66
Allison Division General Motors Corporation Indianapolis 6, Indiana Attention: Plant 8, Technical Library Mr. L. R. Smith	67
Institute for Defense Analysis Research and Engineering Support Division Attention: Technical Information Office 1825 Connecticut Avenue Washington 9, D. C.	68

DISTRIBUTION LIST (cont'd)

	Copy No.
Lockheed Propulsion Company P. O. Box 111 Redlands, California Attention: Miss Belle Berlad, Librarian	69
North American Aviation, Inc. Space & Information Systems Division 12214 Lakewood Boulevard Downey, California Attention: W. H. Morita	70
Purdue University Lafayette, Indiana Attention: M. J. Zucrow	71
Rocketdyne 6633 Canoga Avenue Canoga Park, California Attention: Library, Dept. 596-306	72
Space Technology Laboratory, Inc. 1 Space Park Redondo Beach, California Attention: STL Tech. Library Doc. Acquisitions	73
Thiokol Chemical Corporation Reaction Motors Division Denville, New Jersey Attention: Librarian	74
Thompson Ramo Wooldridge 23555 Euclid Avenue Cleveland 17, Ohio Attention: Librarian	75
The Rand Corporation 1700 Main Street Santa Monica, California Attention: Librarian	76
General Atomics Division General Dynamics Corporation P. O. Box 1111, San Diego, California 92110 Attention: Chief, Tech. Information Services	77

DISTRIBUTION LIST (cont'd)

	Copy No.
Massachusetts Institute of Technology Department of Aeronautical Engineering Cambridge 39, Massachusetts Attention: Dr. J. L. Kerrebrock	78
Institute for Defense Analyses, Rm. 615 1666 Connecticut Avenue, NW Washington, D. C. Attention: Dr. Robert Fox	79
NASA Headquarters Office of Advanced Research & Technology Washington, D. C. Attention: Mr. A. E. Gessow	80
Aerospace Corporation Los Angeles 45, California Attention: Dr. M. L. Rosenzweig	81
Plasma Laboratory, S. W. Mudd Building Columbia University New York, New York Attention: Professor R. A. Gross	82
Office of Advance Research and Technology NASA Headquarters 1520 H Street, NW Washington, D. C. Attention: Dr. A. J. Eggers, Jr.	83
Bureau of Naval Weapons Representative East Hartford, Connecticut Attention: Engineering Division	84
Los Alamos Scientific Laboratory Los Alamos, New Mexico Attention: Dr. George Grover	85
National Aeronautics and Space Council Executive Office of the President Washington, D. C. Attention: Mr. R. V. Mrozinski, Staff Member	86

DISTRIBUTION LIST (cont'd)

	Copy No.
Space Nuclear Propulsion Office c/o Nevada Operations Office U. S. Atomic Energy Commission Las Vegas, Nevada Attention: Mr. R. F. Dickson Director of Technical Division	87
NASA Ames Research Center Mission Analysis Division Moffett Field, California Attention: Mr. H. Hornby	88
Office of Research Analysis (RRRS) Holloman Air Force Base New Mexico Attention: Captain E. N. Kemler	89
Princeton University c/o Document Control Center Attention: Dr. Jerry Grey P. O. Box 710 Princeton, New Jersey 08540	90